

UC San Diego

UC San Diego Electronic Theses and Dissertations

Title

Exploring Bone Nanostructure: Isolation of Phases and Bioinspiration

Permalink

<https://escholarship.org/uc/item/3w81797n>

Author

Su, Frances Yenan

Publication Date

2018

Peer reviewed|Thesis/dissertation

UNIVERSITY OF CALIFORNIA SAN DIEGO

Exploring Bone Nanostructure: Isolation of Phases and Bioinspiration

A dissertation submitted in partial satisfaction of the
requirements for the degree Doctor of Philosophy

in

Materials Science and Engineering

by

Frances Yenan Su

Committee in charge:

Professor Joanna M. McKittrick, Chair
Professor Javier E. Garay
Professor Vlado Lubarda
Professor Marc A. Meyers
Professor Michael T. Tolley

2018

Copyright

Frances Yen-an Su, 2018

All rights reserved.

Dissertation of Frances Yenan Su is approved, and it is acceptable in quality and form for publication on microfilm and electronically:

Chair

University of California San Diego

2018

TABLE OF CONTENTS

SIGNATURE PAGE	iii
TABLE OF CONTENTS.....	iv
LIST OF FIGURES	viii
LIST OF TABLES.....	xii
ACKNOWLEDGEMENTS.....	xiii
VITA.....	xv
ABSTRACT OF THE DISSERTATION.....	xvii
1 Bioinspiration for the Development of New Materials	1
1.1 Engineering Motivations for Bioinspiration	1
1.2 Bioinspiration to Create Tough Materials.....	5
1.3 Models of Bone Nanostructure and Bone as an Interpenetrating Composite.....	9
2 Deproteinization of Cortical Bone: Effects of Different Treatments	13
2.1 Materials and Methods.....	14
2.1.1 Sample Preparation	14
2.1.2 Phosphate Ion Test.....	15
2.1.3 Thermogravimetric Analysis	16
2.1.4 X-ray Diffraction	16
2.1.5 Scanning Electron Microscopy	17
2.1.6 Raman Spectroscopy.....	17
2.1.7 Delipidation.....	18
2.2 Results and Discussion	18
2.2.1 Scanning Electron Microscopy.....	19
2.2.2 Thermogravimetric Analysis	23
2.2.3 X-ray Diffraction	25
2.2.4 Raman Spectroscopy.....	28
2.3 Conclusions.....	33

3	Demineralization of Cortical Bone using Several Protocols and Synthesis of a Collagen Scaffold.....	35
3.1	Materials and Methods.....	39
3.1.1	Sample Preparation.....	39
3.1.2	Raman Spectroscopy.....	40
3.1.3	Fourier-Transform Infrared Spectroscopy.....	41
3.1.4	Scanning Electron Microscopy.....	41
3.1.5	Thermogravimetric Analysis.....	42
3.1.6	Collagen Extraction and Freeze Casting.....	42
3.2	Results and Discussion.....	42
3.2.1	Raman spectroscopy.....	43
3.2.2	Fourier-Transform Infrared Spectroscopy.....	47
3.2.3	Thermogravimetric Analysis.....	50
3.2.4	Scanning Electron Microscopy.....	51
3.2.5	Biomaterial Scaffold Made from Demineralized Bone.....	54
3.3	Conclusions.....	54
4	Size and Scale Effects on Mechanical Properties of Additively Manufactured Two-phase Composites with Continuous or Discontinuous Phases.....	57
4.1	Introduction and Background.....	57
4.2	Materials and Methods.....	59
4.2.1	Additive Manufacturing.....	59
4.2.2	Mechanical Testing and Analysis.....	61
4.2.3	Finite Element Modeling.....	62
4.3	Results and Discussion.....	63
4.3.1	Increasing Number of Unit Cells.....	64
4.3.2	Decreasing Size of Unit Cell.....	74
4.4	Conclusions.....	78
5	Radial-Concentric Freeze Casting Inspired by Porcupine Fish Spines.....	80
5.1	Microstructural control in freeze casting for bioinspired materials.....	82
5.2	Bioinspiration from the porcupine fish spine.....	84
5.3	Materials and Methods.....	86

5.3.1	Freeze casting.....	86
5.3.2	Microstructural characterization	89
5.3.3	Mechanical testing	89
5.4	Results and Discussion	90
5.4.1	Radial and radial-concentric freeze casts: axial cross sections.....	91
5.4.2	Radial freeze cast: longitudinal cross section	93
5.4.3	Radial concentric freeze casts: outer interface.....	96
5.4.4	Radial concentric freeze casts: inner interface.....	98
5.4.5	Mechanical test results.....	98
5.5	Conclusions.....	103
6	Freeze Cast Composite of Hydroxyapatite and Demineralized Bone	105
6.1	Introduction.....	105
6.2	Materials and Methods.....	106
6.2.1	Magnetic Freeze Casting of Hydroxyapatite	107
6.2.2	Collagen Extraction	108
6.2.3	Combined Collagen and Hydroxyapatite Freeze Casting.....	108
6.2.4	Material Characterization.....	109
6.2.5	Mechanical Testing.....	110
6.3	Results and Discussion	110
6.3.1	Scaffold Characterization.....	110
6.3.2	Mechanical Testing in Dry and Hydrated Conditions	114
6.4	Conclusions.....	116
7	Recommendations for Future Work	117
7.1	Age study for mineral content of young porcine bone	117
7.2	Measurement of nanoscale deformation using <i>in situ</i> small angle x-ray scattering and wide angle x-ray diffraction.....	117
7.3	Cell growth study using scaffolds synthesized with the combine collagen and hydroxyapatite freeze casting	118
7.4	Effects of bioinspired hierarchy and anisotropy in additively manufactured composites	119
8	Conclusion.....	121

APPENDIX.....	125
REFERENCES	134

LIST OF FIGURES

Figure 1.1	Toughness vs. stiffness of natural materials composed of collagen and hydroxyapatite compared with a synthetic composite trend predicted by rule of mixtures. Adapted from [1].....	2
Figure 1.2	Biological structural design elements as described in Naleway, et al. [2].....	3
Figure 1.3	(a) Mantis shrimp with dactyl club circled in yellow. (b) Close-up image of dactyl club. (c) Computed tomography image of dactyl club sagittal plane. (d) Differential interference contrast image of boxed region in (c) showing the herringbone pattern of the impact region.....	4
Figure 1.4	Extrinsic and intrinsic toughening mechanisms of bone at different length scales. Taken from Launey, et al. [4].	4
Figure 1.5	Bioinspired materials synthesized with freeze casting compared to their natural analogs. (a,b) Natural bone and their (c,d) bone-inspired counterparts are shown as well as (e,f) natural nacre and (g,h) nacre-like structures formed with freeze casting. Taken from Porter, et al. [14].	6
Figure 1.6	(a) Stress-strain curve and corresponding deformation at points A, B, C, D, and E on the curve of laser etched borosilicate glass infiltrated with polyurethane inspired by nacre. (b) Nominal stress vs normalized displacement of crossply glass inspired by fish scales. Figure adapted from [15] and [16].	8
Figure 1.7	Steps to use additive manufacturing to explore biological materials and bioinspired designs.....	8
Figure 1.8	The bioinspiration cycle—a relationship between biology and engineering. Each field informs the other for better overall understanding. Example shown is the gecko and a gecko-inspired robot. Taken from Porter [21].	9
Figure 1.9	Cortical bone structure of mammalian long bone from nanoscale to mesoscale. Figure adapted from [23, 29].	10
Figure 1.10	Nanoscale models of mineralized collagen in bone. The staggered crystal model [9], extrafibrillar mineral model [15], and composite with interpenetrating phases [17].	11
Figure 2.1	Photograph of untreated (UT) porcine femur sample and specimens after six days of treatments using KOH, NaOH, NaOCl, and H ₂ O ₂	19
Figure 2.2	Scanning electron microscopy (SEM) images of untreated (a,f) and chemically treated samples using: (b,g) H ₂ O ₂ , (c,h) NaOCl, (d,i) NaOH, and (e,j) KOH. (f), (g), (h), (i) and (j) are high resolution SEM images of each sample. The bone growth direction is in the plane of the page.	20
Figure 2.3	Phosphate ion test of different deproteinization treatment solutions after one day of deproteinization: (a) NaOH, (b) KOH, (c) H ₂ O ₂ , and (d) NaOCl.....	22
Figure 2.4	Thermogravimetric analysis taken over six days for samples treated with H ₂ O ₂ , NaOH, and KOH and for 14 days with NaOCl. Yellow represents weight percentage of organic materials, while blue and green represent weight percentages of water and mineral, respectively.	24
Figure 2.5	(a) X-ray diffraction patterns of untreated and chemically treated samples. Blue dotted lines indicate peaks that match those of the PDF for hexagonal hydroxyapatite. Red dotted lines indicate peaks that do not match or are shifted. (b) X-ray diffraction of intact, untreated bone.....	27

Figure 2.6	Raman spectra of untreated bone and samples treated with NaOCl (4, 8, 10, 12, and 14 days). Red dotted lines indicate bands associated with collagen.	30
Figure 2.7	The mineral-to matrix ratio ($\nu_1\text{PO}_4^{3-}$ / amide III), carbonate-to-mineral ratio ($\nu_1\text{CO}_3^{2-}$ / $\nu_1\text{PO}_4^{3-}$), and crystallinity ($1/\text{FWHM}$ of $\nu_1\text{PO}_4^{3-}$) calculated from Raman imaging for untreated bone and samples treated with NaOCl for 4, 8, 12, and 14 days given as average \pm S.D. (standard deviation).	31
Figure 2.8	Raman spectroscopy of untreated bone and three different sequences of treatments: DP-DF (deproteinization, then defatting); DF-DP (defatting, then deproteinization); and DP-DF-DP (defatting, deproteinization, and then defatting again). Red dotted lines indicate bands associated with collagen.	32
Figure 3.1	Hydrochloric acid/ ethylene-diamine tetraacetic acid (HCl/EDTA) mixture treated sample that is over demineralized and shrunken compared to HCl treated samples.	43
Figure 3.2	(a) Representative Raman spectra indicate mineral and collagen bands for the control bone (Untreated), and for ethylene-diamine tetraacetic acid (EDTA), formic acid (CH_2O_2), hydrochloric acid (HCl) and the HCl/EDTA mixture. (b) Outlined area in (a) with a solid border is shown with the.	45
Figure 3.3	Raman spectroscopy analytical study of mineral and collagen content for control bone, and for ethylene-diamine tetraacetic acid (EDTA), formic acid (CH_2O_2), hydrochloric acid (HCl) and the HCl/EDTA mixture treated bone. (a) The inset is an enlarged plot of the mineral-to-matrix ratio.	46
Figure 3.4	(a) Fourier-transform infrared spectra for control bone (Untreated), and for ethylene-diamine tetraacetic acid (EDTA), formic acid (CH_2O_2), hydrochloric acid (HCl) and the HCl/EDTA mixture treated bone. (b) Magnified spectra from boxed region in (a) showing the shift in the amide II band.	48
Figure 3.5	Thermogravimetric analysis results after heating to 800°C : weight percentage of mineral and protein once water is removed after each demineralization treatment.	50
Figure 3.6	Scanning electron microscopy images of (a) untreated bone and demineralized bone using (b) ethylene-diamine tetraacetic acid (EDTA), (c) hydrochloric acid (HCl), (d) HCl/EDTA mixture, and (e,f) formic acid (CH_2O_2). Visible fibrils are outlined in yellow, dotted lines and d -spacing is indicated by arrows.	52
Figure 3.7	Toughness vs. stiffness of natural materials composed of collagen and hydroxyapatite compared with a synthetic composite trend predicted by rule of mixtures. Adapted from [1].	54
Figure 4.1	Types of unit cells and samples with varying numbers of unit cells.	60
Figure 4.2	Stress-strain curves of 3D printed samples for (a) discontinuous phase composites, (b) matrix-inclusion composite with soft frame, (c) matrix-inclusion composite with stiff frame, (d) interpenetrating composite with soft frame.	65
Figure 4.3	(a) Yield stress, (b) yield strain, (c) elastic moduli of composites with increasing number of cells, where gray bars show modeling results and colored bars show experimental results.	69
Figure 4.4	Strain maps for ϵ_{xy} and ϵ_{yy} for each composite geometry.	71
Figure 4.5	Deformation of different composite types with different numbers of unit cells. All samples measure 12.7 mm in side length.	72

Figure 4.6	Average stress-strain curves for samples with different sizes. Component materials (a) soft phase material (TangoBlackPlus) and (b) stiff phase material (VeroClear) and composite geometries (c) discontinuous composite, (d) matrix-inclusion composite with stiff shell	75
Figure 4.7	(a) Yield strain, (b) yield strength, and (c) elastic moduli of composites with decreasing unit cell size from experiments.....	77
Figure 5.1	Packing of ceramic particles in between ice crystals during freeze casting. (A) Slurry of ceramic particles (green) suspended within water, in contact with freezing surface before cooling is applied. (B) Cooling of the freezing surface begins, and ice crystals begin to form at the freezing surface.	80
Figure 5.2	(A) Porcupine fish fully inflated, with defensive spines oriented outwards [214]. (B) Schematic of ultrastructure and microstructure of the porcupine fish spine, adapted from [210].	85
Figure 5.3	Overview of freeze casting methods (bottom freezing surface underneath molds not shown). (A) Conventional freeze casting, (B) radial freeze casting and (C) radial-concentric freeze casting. A copper pin is placed in the center of the copper mold. Then, the direction of freezing.....	88
Figure 5.4	Freeze cast samples composed of 30 vol.% alumina. Full composite images of axial cross sections of each sample were created by stitching together multiple images, with each individual image taken at approximately 38× magnification. Samples freeze cast through (A) conventional, (B) radial, and	91
Figure 5.5	Scanning electron microscopy images of freeze cast samples composed of 30 vol.% alumina. Radial freeze cast (A) outermost region and (B) innermost region. Concentric freeze cast (C) outer layer, outer region; (D) outer layer, inner region; (E) core layer, outer region; (F) core layer, inner region.	92
Figure 5.6	Longitudinal cross section of radial freeze cast sample. (A) Schematic diagram of longitudinally sectioned freeze cast sample. (B) Composite scanning electron microscopy image of longitudinal section in blue boxed area in (A) with yellow dotted line delineating the meeting of lamellae growing longitudinally	94
Figure 5.7	(A) Scanning electron microscopy images of inner and outer rings in a representative radial-concentric freeze cast sample. (B) Zoomed-in image of boxed region in (A) of inner ring, with yellow dashed line highlighting the interface. (C) Zoomed-in image of boxed region in (A) of outer ring	96
Figure 5.8	Schematic of packing of ceramic particles at the outer interface. (A) The setup of the radial-concentric freeze casting method in the first step of the process (showing a 3-dimensional view per the axes in the bottom left corner), with a schematic representation of the boxed region shown in a top-down view in	97
Figure 5.9	Results from mechanical testing, where brackets labeled “n.s.” indicate results found to have no significant difference under Tukey pairwise comparisons for both structure and infiltration. Axial compressive strength in (A) uninfiltated and (B) infiltated samples from axial compression tests.....	99
Figure 5.10	Crack patterns in representative samples after Brazilian testing. (A) Uninfiltated conventional. (B) Uninfiltated radial. (C) Uninfiltated radial-concentric. (D) Infiltrated conventional. (E) Infiltrated radial. (F) Infiltrated radial-concentric..	102

Figure 6.1	Process for making a combined hydroxyapatite (HA) and collagen freeze cast scaffold. The process is divided into two parts. Part I consists of HA preparation, freeze casting, and sintering. Part II involves preparing the collagen solution, combined freeze casting with HA and collagen, and crosslinking 107	107
Figure 6.2	Scanning electron micrographs of the transverse cross-section of (a) magnetized HA and (b) combined collagen and magnetized HA scaffolds. Directions shown in (a) are applicable for both panels..... 111	111
Figure 6.3	Fourier transform infrared spectra of (a) bone demineralized with HCl, untreated bone, and magnetized HA samples as well as (b) combined collagen and magnetized hydroxyapatite scaffolds in different regions of the scaffold transverse cross-section. Bands associated with hydroxyapatite are shown as dotted lines, and collagen-associated peaks are dashed..... 112	112
Figure 6.4	(a) Compression strength of scaffolds under dry or hydrated conditions and (b) Young's modulus of scaffolds in dry and hydrated conditions. Error bars show standard deviation 115	115
Figure B.1	Freeze casting experimental setup adapted from Wegst, et al. [9]. 128	128
Figure C.1	Average stress-strain curves of composite unit cells. 130	130

LIST OF TABLES

Table 2.1	Deproteinization treatments.....	15
Table 2.2	The average weight of bone constituents by thermogravimetric analysis during four chemical treatments (n=2).....	25
Table 2.3	Statistical significance between each treatment duration presented by <i>p</i> -value.	30
Table 3.1	Sample preparation by demineralization agents: EDTA (ethylene-diamine tetraacetic acid), formic acid (CH ₂ O ₂), hydrogen chloride (HCl), and HCl/EDTA mixture.....	40
Table 3.2	Effectiveness summary for EDTA (ethylene-diamine tetraacetic acid), formic acid (CH ₂ O ₂), hydrochloric acid (HCl), and HCl/EDTA mixture as determined from Raman spectroscopy.....	47
Table 3.3	Fourier-transform infrared spectroscopy absorption bands for bone and their functional groups	48
Table 3.4	Elemental analysis from energy dispersive X-ray spectroscopy for untreated specimens and samples after treatments. Both atomic percentage and weight percentage are provided. The relative standard deviations are given as 2 σ . ..	53
Table 4.1	Mechanical properties of the stiff and soft polymer materials used for additive manufacturing. TangoBlack+ has no elastic modulus value since it is a nonlinear material. Poisson's ratio was given by the manufacturer. Values are given as average (s.d.).....	60
Table 4.2	Effective modulus equations and calculated values based on properties of VeroClear and TangoBlackPlus with a volume fraction (ϕ) of 0.5 for each phase. Values are calculated with mechanical properties of the stiff and soft polymers given in Table 1.....	70
Table 4.3	Surface area of the interface between the two phases to volume ratio of the overall sample with dimensions 12.7×12.7×12.7 mm ³ . Units are in mm ⁻¹ . ..	74
Table 5.1	Wall thicknesses of lamellae, where N is the number of measurements taken and SD is the standard deviation. Measurements were taken using ImageJ software.....	92
Table A.1	Lattice parameters <i>a</i> and <i>c</i> calculated through Rietveld refinement as well as <i>c/a</i> ratio. Goodness of fit for each refinement is as also shown. Estimated standard deviations are shown in parentheses for the last two significant figures.	125
Table A.2	Lattice parameters <i>a</i> and <i>c</i> calculated through Rietveld refinement as well as <i>c/a</i> ratio. Goodness of fit for each refinement is as also shown. Estimated standard deviations are shown in parentheses for the last two significant figures.	126
Table C.1	Yield strain, yield stress, and elastic modulus values from FEM and experiments. Values for experiments are given as average (s.d) and n=6 for each sample type.	129
Table D.1	Summary of mechanical test results, where N is the number of samples and SD is the standard deviation.	131
Table D.2	Analysis of variance, p-values (where p<0.05 indicates that the mechanical property is influenced by the source).....	132

ACKNOWLEDGEMENTS

I would like to thank and acknowledge Professor Joanna McKittrick for her support as the chair of my committee, for guidance as my PhD advisor, and always being supportive of my research and career. I would also like to thank my committee members Marc Meyers, Vlado Lubarda, Olivia Graeve, and Michael Tolley for their support and feedback on my dissertation. I am grateful for my undergraduate mentees that have helped me immensely with work. These individuals include Joyce Mok, Rachel Hsiong, Amesha Green, Justin Salim, Katherine Tang, and Gowri Viswanathan.

I would also like to acknowledge my collaborators and groups who have helped in immeasurable ways: Professor Iwona Jasiuk, Siyuan Pang, and Fereshteh Sabet. In addition, I would like to acknowledge the support from the San Diego Nanotechnology Infrastructure (SDNI) at UCSD, a member of the National Nanotechnology Coordinated Infrastructure, which is supported by the National Science Foundation (Grant number ECCS-1542148) and Sabine Faulhaber from the UCSD Nanoengineering Materials Research Center for help with the FTIR and TGA instruments.

Finally, I would like to thank my current and past lab colleagues for their help, insights, and for great discussions. In particular, I would like to thank Mike Frank, Steven Naleway, Jerry Jung, Jungmin Ha, Keisuke Matsushita, Sean Garner, and Isaac Cabrera.

Chapter 1 and 2, in part, is a reprint of the material as it appears in “Deproteinization of cortical bone: Effects of different treatments” *Calcified Tissue International*, vol. 103, pp 554-556, 2018. The dissertation author was one of the primary investigators and authors on this paper. This paper was co-authored by Siyuan Pang, Yik Tung Tracy Ling, Peter Shyu, Ekaterina

Novitskaya, Kyungah Seo, Sofia Lambert, Kimberlin Zarate, Olivia A. Graeve, Iwona Jasiuk, and Joanna McKittrick.

Chapter 3, in part, is a reprint of the material as it appears in “Demineralization of Cortical Bone using Several Protocols and Synthesis of a Collagen Scaffold,” which has been submitted for publication. The dissertation author was one of the primary investigators and authors on this paper. This paper was co-authored by Siyuan Pang, Amesha Green, Justin Salim, Joanna McKittrick, and Iwona Jasiuk.

Chapter 4, in part, is in preparation for submission for publication as “Size and Scale Effects on Mechanical Properties of Additively Manufactured Two-phase Composites with Continuous or Discontinuous Phases,” 2018. The dissertation author is the primary investigator and author on this paper. The work is co-authored by Fereshteh A. Sabet, Katherine Tang, Rachel Hsiong, Michael Tolley, Iwona Jasiuk, and Joanna McKittrick.

Chapter 5, in part, is in preparation for submission for publication as “Radial-Concentric Freeze Casting Inspired by Porcupine Fish Spines,” 2018. The dissertation author was one of the primary investigators and authors on this paper. This work is co-authored by Joyce R. Mok and Joanna McKittrick.

Chapter 6, in part, is in preparation for submission for publication as “Freeze Cast Composite of Hydroxyapatite and Demineralized Bone,” 2018. The dissertation author is the primary investigator and author on this paper. This work is co-authored by Gowri Viswanathan, Justin Salim, and Katherine Tang, and Joanna McKittrick.

This work is supported financially National Science Foundation, Biomaterials (grant numbers DMR-1507978 and 1507169) and a Multi-University Research Initiative through the Air Force Office of Scientific Research (grant number AFOSR-FA9550-15-1-0009).

VITA

- 2014 Bachelor of Science, Harvey Mudd College
- 2015 Master of Science, University of California San Diego
- 2014-2018 Graduate Research Assistant, University of California San Diego
- 2018 Teaching Assistant, University of California San Diego
- 2018 Doctor of Philosophy, University of California San Diego

PUBLICATIONS

Booster, N.A., Su, F.Y., Adolph, S.C., and Ahn, A.N. "Effect of temperature on leg kinematics in sprinting tarantulas (*Aphonopelma hentzi*): high speed may limit hydraulic joint actuation." *Journal of Experimental Biology*, 218(7): p. 977-982 (2015).

DOI: 10.1242/jeb.111922

Su, F.Y., Bushong, E.A., Deerinck, T.J., Seo, K., Herrera, S., Graeve, O.A., Kisailus, D., Lubarda, V.A., and McKittrick, J. "Spines of the porcupine fish: Structure, composition, and mechanical properties." *Journal of the Mechanical Behavior of Biomedical Materials*, 73: p. 38-49 (2017).

DOI: 10.1016/j.jmbbm.2017.02.029

Su, F.Y., Pang, S.Y., Ling, Y.T.T., Shyu, P., Novitskaya, E., Seo, K., Lambert, S., Zarate, K., Graeve, O.A., Jasiuk, I., and McKittrick, J. "Deproteinization of cortical bone: effects of different treatments." *Calcified Tissue International*, 103(5): p. 554-566 (2018).

DOI: 10.1007/s00223-018-0453-x

Jasiuk, I., Abueidda, D.W., Kozuch, C., Pang, S.Y., Su, F.Y., and McKittrick, J., "An overview on additive manufacturing of polymers," *JOM*, 70(3): p. 275-283 (2018).

DOI: 10.1007/s11837-017-2730-y

Sabet, F.A., Su, F.Y., McKittrick, J., and Jasiuk, I. "Mechanical properties of model two-phase composites with continuous compared to discontinuous phases." *Advanced Engineering Materials*, 20:1800505, p. 1-6 (2018).

DOI: 10.1002/adem.201800505

Pang, S.Y., Su, F.Y., Green, A., Salim, J., McKittrick, J., and Jasiuk, I. "Demineralization of cortical bone using various protocols." Submitted to *ACS Biomaterials Science and Engineering*.

Su, F.Y., Mok, J.R., and McKittrick, J. “Radial and concentric freeze casting bioinspired by the porcupine fish.” In preparation.

Su, F.Y., Sabet, F.A., Tang, K., Hsiong, R., Tolley, M., Jasiuk, I., and McKittrick, J. “Size and scale effects on mechanical properties of additively manufactured two-phase composites with continuous or discontinuous phases.” In preparation.

Su, F.Y., Viswanathan, G., Salim, J., Tang, K., and McKittrick, J. “Combined freeze casting of hydroxyapatite and collagen for bone implant applications.” In preparation.

FIELDS OF STUDY

Major Field: Materials Science and Engineering

Studies in Bioinspired Materials
Professor Joanna McKittrick

ABSTRACT OF THE DISSERTATION

Exploring Bone Nanostructure: Isolation of Phases and Bioinspiration

by

Frances Yenan Su

Doctor of Philosophy in Materials Science and Engineering

University of California San Diego, 2018

Professor Joanna McKittrick, Chair

Bone can achieve high strength and toughness simultaneously through its composite structure and multiple structural hierarchies, which are revealed from the nanoscale to macroscale. While numerous studies have been published on hierarchical structure of bone, the nanostructure is still a topic of debate. To date, there are three main models of bone at the nanoscale. The first and most widely accepted is the staggered crystal model which states that hydroxyapatite (HA) crystals are generally confined to the gap regions in the collagen matrix. Another model states that mineral is primarily extrafibrillar, surrounding collagen fibrils as

curved lamellae. Finally, we propose that bone is an interpenetrating phase composite with a continuous mineral phase.

This doctoral dissertation explores whether bone is an interpenetrating composite by isolating the component phases in bone through either deproteinization to remove the organic phase (collagen) or demineralization to remove the mineral phase (non-stoichiometric hydroxyapatite). In these studies, the most efficient chemical treatments that also preserve residual phases was found. Quality of the remaining phases was examined using techniques such as Raman spectroscopy, Fourier transform infrared spectroscopy, x-ray diffraction, and scanning electron microscopy. Mineral was found to form a continuous phase in bone from the deproteinization study, and demineralized bone was used to make a collagen scaffold with biomedical applications.

Next, the effect of geometrical arrangement of phases on mechanical properties was explored through 3D printing and finite element modeling. The geometrical arrangements tested include a discontinuous phase composite, a matrix inclusion composite with a stiff or soft frame, and an interpenetrating composite with a stiff or soft phase representing the mineral and protein phases of bone, respectively. A continuous stiff phase was found to increase composite stiffness. The soft phase functioned to redistribute stress. Size effects of 3D print features on mechanical properties of composites are also discussed, showing that imperfections in additive manufacturing have a large effect on mechanical properties.

Finally, drawing inspiration from two collagen-hydroxyapatite composites (porcupine fish spines and bone), synthetic scaffolds are designed and created using freeze casting. The effect of microstructure and hydration on mechanical properties is discussed for the topics, respectively.

1 Bioinspiration for the Development of New Materials

1.1 Engineering Motivations for Bioinspiration

Engineers design products given a certain set of functions, objectives, and constraints. What has increasingly become clear is that the ability of engineers to design is strongly dependent on constraints of the materials they are designing with—this is where the field of materials science and engineering comes in. Common material classes include metals, ceramics, semiconductors, and polymers with each having their own specific behaviors and properties that are better in some applications rather than others. A category of materials that has become increasingly important is composite materials, which include multiple phases or components with different properties. The blending of two materials to form a new one that often has new intermediate properties of the base materials.

Engineers have always been on a quest for lightweight materials that are strong and also tough. These materials would have a variety of uses in automotive, aerospace, defense, and as well as medicine. In nature, organisms have found ways to create strong and tough materials out of relatively lightweight components, which is a priority since organisms need protection as well as easy mobility to survive. Key base materials include the structural proteins collagen and keratin, mineral hydroxyapatite or calcite, and sugars such as chitin. Biological materials are often composed of one or more of these materials and are often highly ordered materials at multiple length scales, creating a hierarchical structure. These materials tend to perform better than equivalent compositions as predicted by a typical rule of mixtures (Figure 1.1).

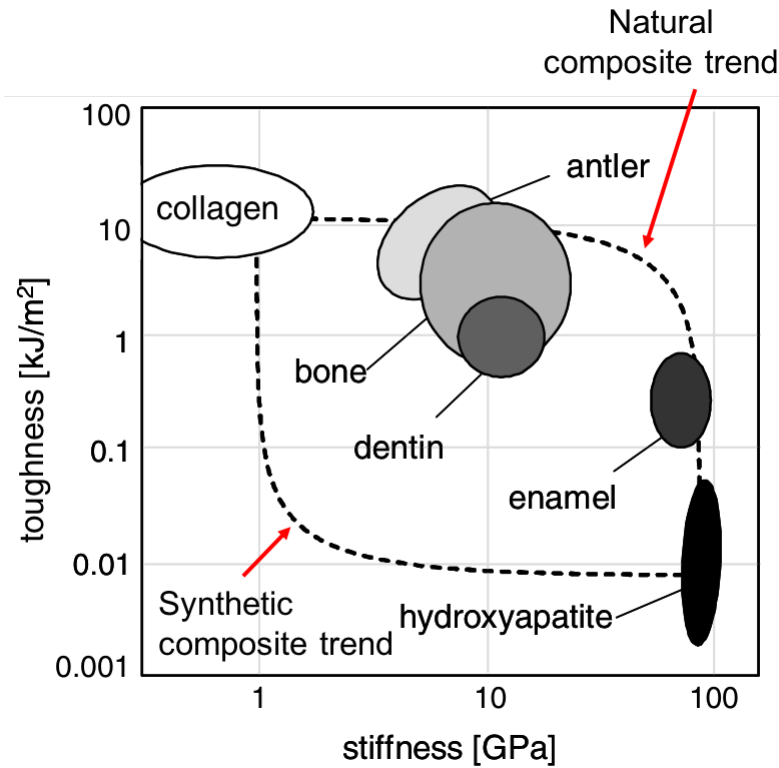


Figure 1.1. Toughness vs. stiffness of natural materials composed of collagen and hydroxyapatite compared with a synthetic composite trend predicted by rule of mixtures. Adapted from [1].

Structural themes have been identified throughout biological materials including fibrous, helical, gradient, layered, tubular, cellular, suture, and overlapping structures [2] (Figure 1.2). These common themes can be combined and exist at different length scales, and although the basic building blocks of biological materials are often relatively weak when compared with manmade materials, the structural hierarchy in biological materials can lead to mechanical properties far surpassing what is expected. Fibrous materials are a common theme in many biological materials and usually help with tensile properties. Helical arrangements

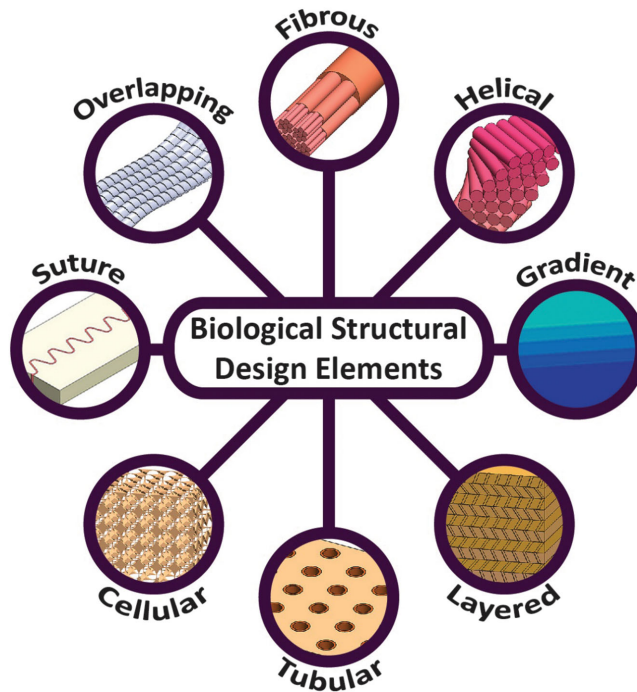


Figure 1.2. Biological structural design elements as described in Naleway, et al. [2].

Often, the greatest benefit that hierarchy instills is a dramatic increase in toughness. This is illustrated in the herringbone helical arrangement of mineralized fibers in the impact region of the mantis shrimp dactyl club (Figure 1.3), which increase toughness by making it difficult for cracks to propagate through the material [3]. Within bone, each level of hierarchy has a distinct mechanism for arresting cracks from the macro- to nanoscale including: crack deflection and twisting by osteons, uncracked ligament bridging, collagen-fibril bridging, constrained microcracking, sacrificial bonds between collagen fibers, fibrillary sliding, and molecular uncoiling of tropocollagen at the nanoscale [4]. The multi-hierarchy toughening mechanisms of bone are shown in Figure 1.4. The high toughness of these materials is where biological materials shine, motivating the field of bioinspiration, where humans use these design principles from nature to manufacture new engineering solutions.

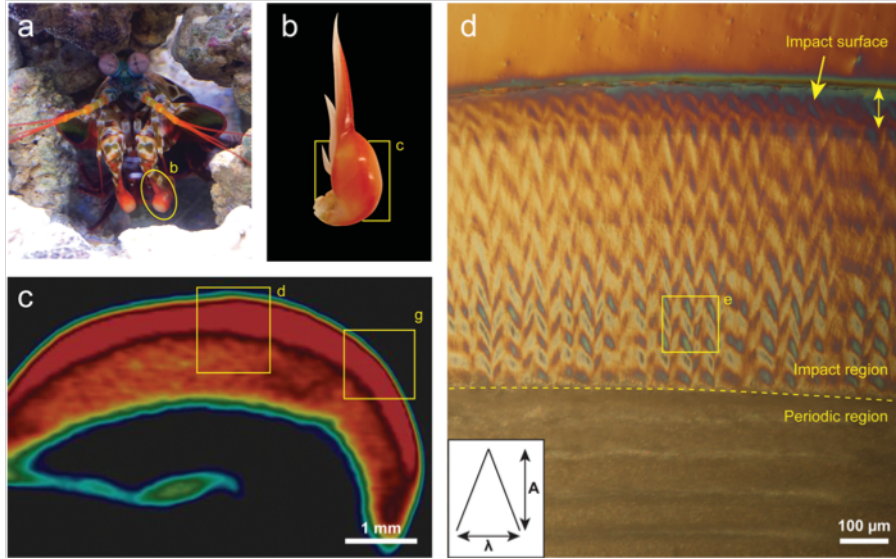


Figure 1.3. (a) Mantis shrimp with dactyl club circled in yellow. (b) Close-up image of dactyl club. (c) Computed tomography image of dactyl club sagittal plane. (d) Differential interference contrast image of boxed region in (c) showing the herringbone pattern of the impact region and linear pattern of the periodic region of the dactyl club. Figure taken from [3].

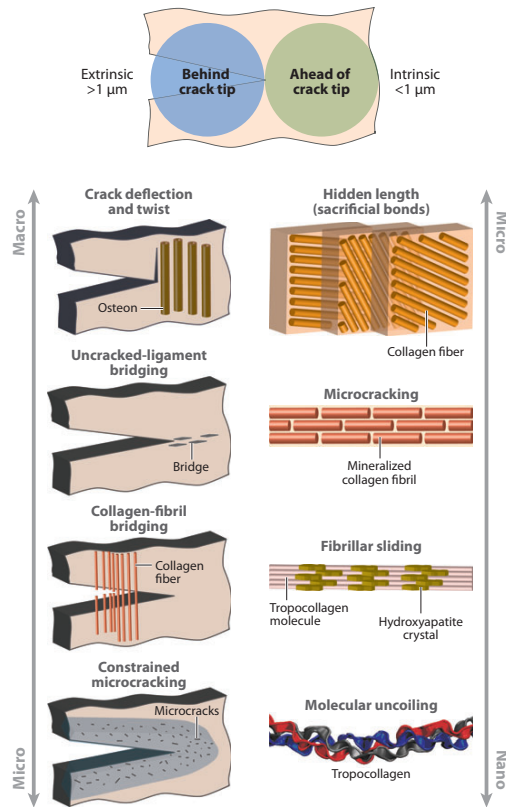


Figure 1.4. Extrinsic and intrinsic toughening mechanisms of bone at different length scales. Taken from Launey, et al. [4].

1.2 Bioinspiration to Create Tough Materials

Organisms have been a source of inspiration for a long time, from the flying machine designs of da Vinci inspired by birds to the advent of Velcro inspired by plant burrs. Many designs have focused on macrostructural features, such as the Japanese Shinkansen train based on the kingfisher beak to prevent sonic booms as trains go through tunnels and wind turbines inspired by the humpback whale fin to reduce drag [5]. However, as the microstructure of biological materials are cataloged and characterized, new materials are being developed with bioinspired microstructures to be strong and tough.

A method called freeze casting, which creates lamellar structures in porous ceramics, is one of the primary methods for imitating bone [6-9] and nacre's [10, 11] lamellar microstructure (Figure 1.5). In this method, a slurry containing ceramic particles, binding polymer, dispersant, and a solvent (usually water) is frozen directionally in a mold. The ice grows directionally from one end of the mold to the other, compacting the ceramic particles into lamellae. Water is then sublimated, leaving interconnected pores within a ceramic scaffold and the binding polymer holds the particles together. Finally, the ceramic green body is placed into a high temperature oven and the particles are sintered to form a continuous scaffold with aligned porosity. Porosity and microstructure can be varied through intrinsic and extrinsic means. Intrinsic properties include slurry solvent, and other additives such as alcohols to adjust porosity [8]. Extrinsic properties are outside influences on the system such as freezing direction and magnetic fields to align particles [7, 12]. After sintering, the scaffold can be infiltrated with another phase such as an epoxy or other polymer. Launey, et al. [13] took this a step further by infiltrating the alumina freeze cast scaffold with a metal to create a material much stronger than natural nacre.

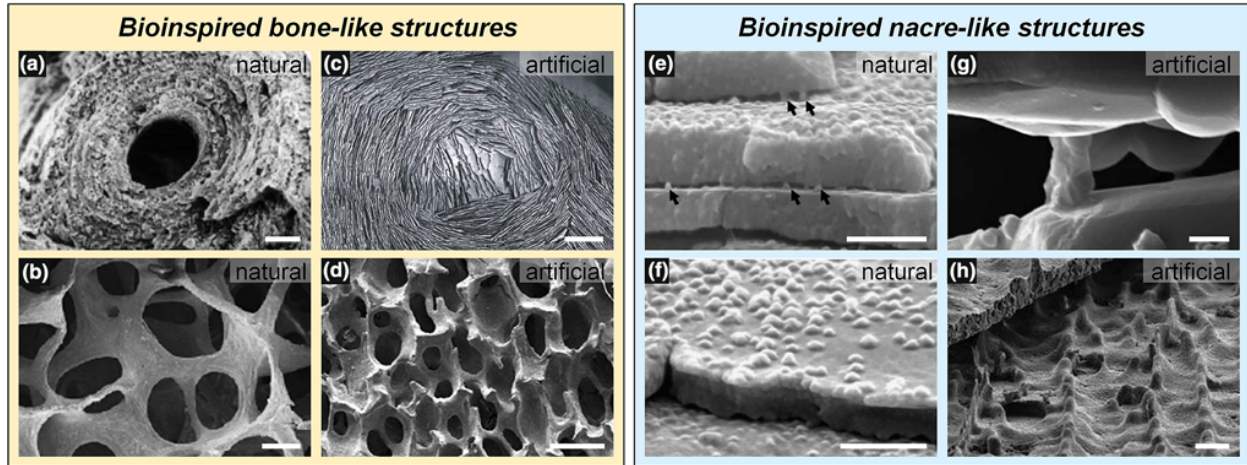


Figure 1.5. Bioinspired materials synthesized with freeze casting compared to their natural analogs. **(a,b)** Natural bone and their **(c,d)** bone-inspired counterparts are shown as well as **(e,f)** natural nacre and **(g,h)** nacre-like structures formed with freeze casting. Taken from Porter, et al. [14].

Aside from freeze casting, other techniques have been used to explore bioinspiration. Laser etching has been used to create patterned glass infiltrated with polyurethane to mimic the microstructure of nacre [15] (Figure 1.6a). These composites were found to exhibit similar deformation mechanisms as natural nacre. This laser etching technique has also been used to investigate crossply patterns in glass-polymer composites inspired by fish scale and arthropod cuticles [16] (Figure 1.6b). Findings show that this composite allows for large deformations and prevents brittle fracture of normal laminated glass while maintaining transparency. Finally, laser etching has also been used to create trenches in aluminum oxide plates to channel cracks to certain paths, a phenomenon seen in many biological materials such as bone, teeth, and mollusk shells [17]. These studies focus on guiding and controlling damage in materials to increase toughness of materials.

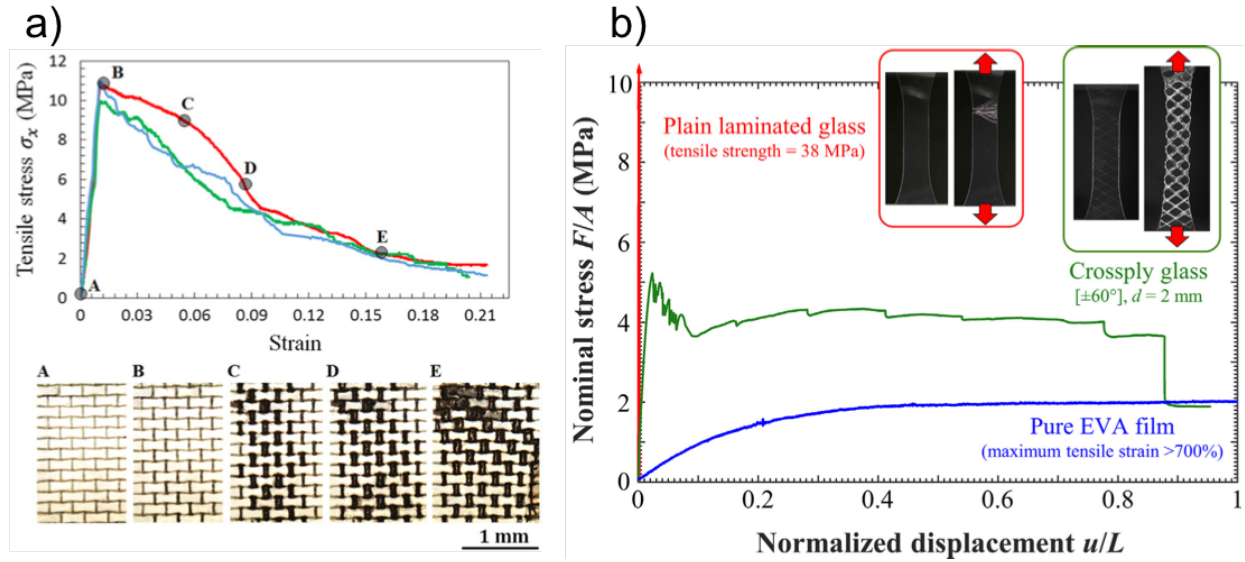


Figure 1.6. (a) Stress-strain curve and corresponding deformation at points A, B, C, D, and E on the curve of laser etched borosilicate glass infiltrated with polyurethane inspired by nacre. (b) Nominal stress vs normalized displacement of crossply glass inspired by fish scales. Figure adapted from [15] and [16].

One method that has become increasingly prominent in literature to understand biological material microstructure is additive manufacturing. As discussed in a recent review article written by Velasco-Hogan, et al. [18], additive manufacturing can be used to optimize designs inspired from nature through the process described in Figure 1.7. A template design is derived from natural materials and fabricated using additive manufacturing. These prototypes can then be characterized by mechanical testing. Refinement or optimization of these designs and repeated testing help elucidate new aspects of biological materials and therefore, engineering designs. Additive manufacturing has been used to investigate microstructural effects on energy dissipation, fracture toughness and strength, damage tolerance and flexibility, damage mechanisms, shape morphing, and dry adhesion. Additionally, Sullivan [19] used 3D printing to create a series of recoverable material designs inspired by the interlocking barbs and barbules in birds of flight.

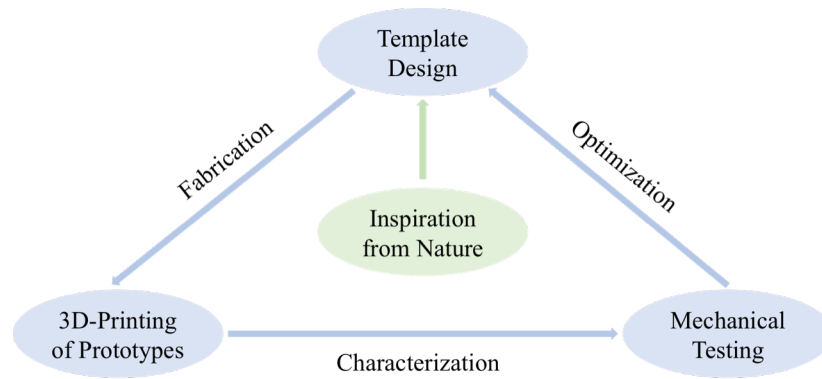


Figure 1.7. Steps to use additive manufacturing to explore biological materials and bioinspired designs. Taken from Velasco-Hogan, et al. [18].

Finally, bioinspiration is part of what has been dubbed the bioinspiration cycle (shown in Figure 1.8), which is a synergistic relationship between biology and engineering. Observations in biology can inspire new engineering designs. These engineering designs can then be used to understand more about biological phenomena. For example, the work of Porter, et al. [20] shows that a seahorse tail is square to prevent crushing of the spinal column while allowing flexibility of the prehensile tail. A tail with a circular cross-section was created through additive manufacturing for comparison and tested under the same crushing conditions as the square tail. The circular cross-section tail was not optimal for those loading conditions, informing biologists why seahorses may have developed the square tails instead of round ones through the course of evolution. Therefore, through the process of the bioinspiration cycle, one can learn more about the biological systems themselves.

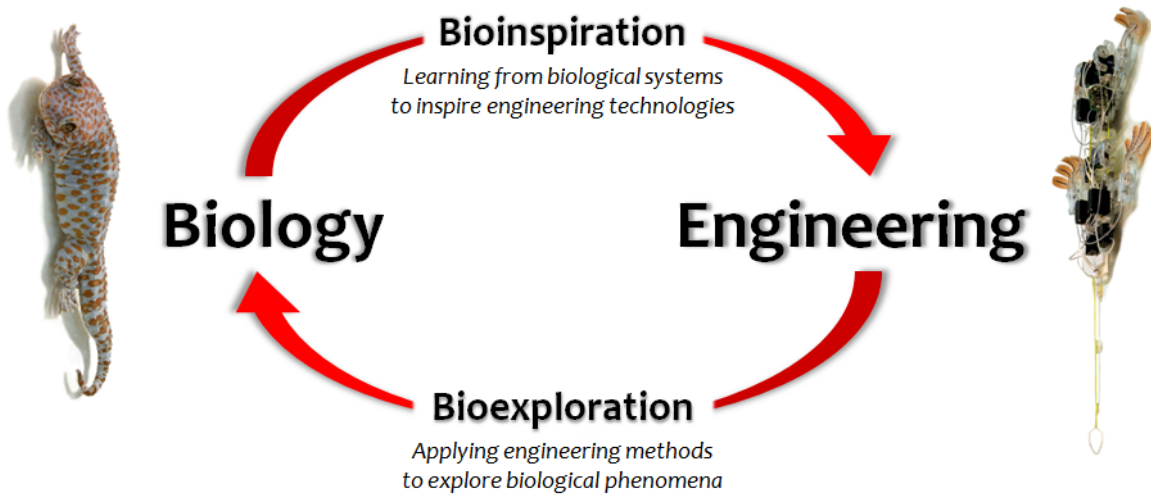


Figure 1.8. The bioinspiration cycle—a relationship between biology and engineering. Each field informs the other for better overall understanding. Example shown is the gecko and a gecko-inspired robot. Taken from Porter [21].

1.3 Models of Bone Nanostructure and Bone as an Interpenetrating Composite

Bone has been the subject of intense studies due to its high strength, stiffness, and toughness [22]. Strength and toughness are often mutually exclusive. However, biological materials such as bone can achieve high strength and toughness simultaneously [23]. Bone's impressive mechanical properties are a result of its composite structure and multiple structural hierarchies, which is revealed from the nanoscale to the macroscale [1]. Bone is composed of ~65 wt.% mineral—non-stoichiometric hydroxyapatite ($\text{Ca}_5(\text{PO}_4)_3(\text{OH})$), 10 wt.% water, and 25 wt.% organics. Organics include mainly type I collagen (~22.5 wt.%), noncollagenous proteins (2.5-3.75 wt.%), and lipids (1-10 wt. %) [24-26]. Starting at the nanoscale, amino acids form polypeptide chains that assemble into tropocollagen molecules. Tropocollagen then forms collagen fibrils with regular arrangements and a periodic spacing of 67 nm [27, 28]. At the microscale, fibrils mineralized with hydroxyapatite form larger fibers and fiber sheets called

lamellae. In cortical bone, the mineralized collagen sheets are arranged in concentric layers with rotating fiber arrangements. At the mesoscale, the concentric layers surround blood vessels, forming osteons in cortical bone. At the macroscale, cortical bone (dense) and trabecular bone (porous) form whole bone. The hierarchical structure of cortical bone is shown in Figure 1.9.

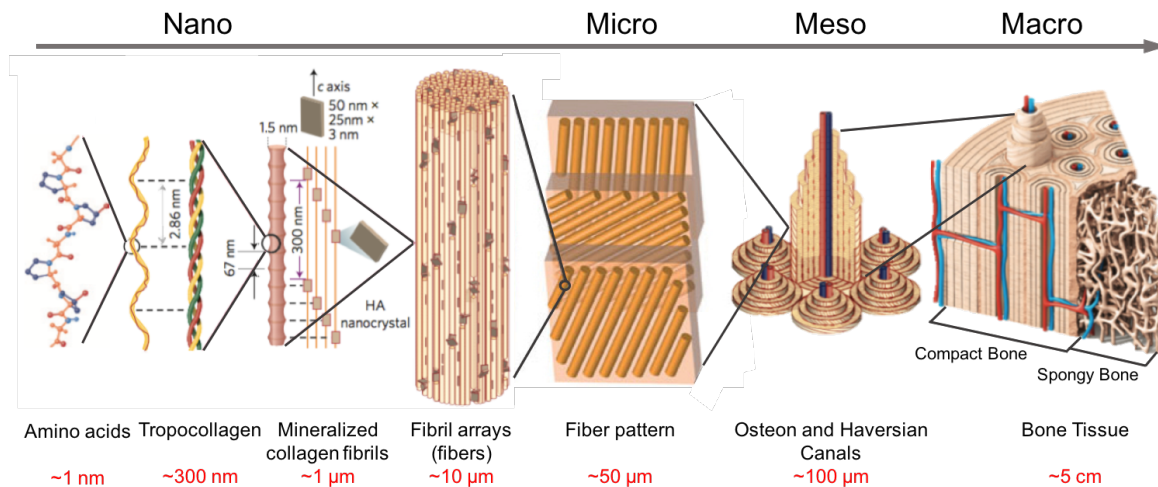


Figure 1.9. Cortical bone structure of mammalian long bone from nanoscale to mesoscale. Figure adapted from [23, 29].

While numerous studies have been published on the hierarchical structure of bone, the nanostructure is still a topic of debate. To date, there are three main models of bone at the nanoscale as illustrated in Figure 1.10. The first and most widely accepted is the staggered crystal model [30], which states that hydroxyapatite crystals are mainly confined to the gap regions of the collagen matrix. However, due to the limited volume available in collagen gap regions (40 nm) and knowing the volume ratio of collagen to hydroxyapatite is approximately 1:1 in bone [31], the staggered crystal model is likely not a full representation of the nanoscale structure of bone. Another model states that the mineral is primarily extrafibrillar [32-35]. It has also been suggested that extrafibrillar minerals are in the form of curved crystals [30] or lamellae (multiple layers of crystal arrays) [36] that wrap around collagen fibrils [30, 36]. Finally, bone

has been considered to be a composite with interpenetrating collagen and mineral phases at the nanoscale, meaning that both mineral and collagen form their own networks that are intertwined with each other. This was hypothesized after deproteinization of trabecular and cortical bone revealed an intact hydroxyapatite scaffold that did not collapse [37-40].

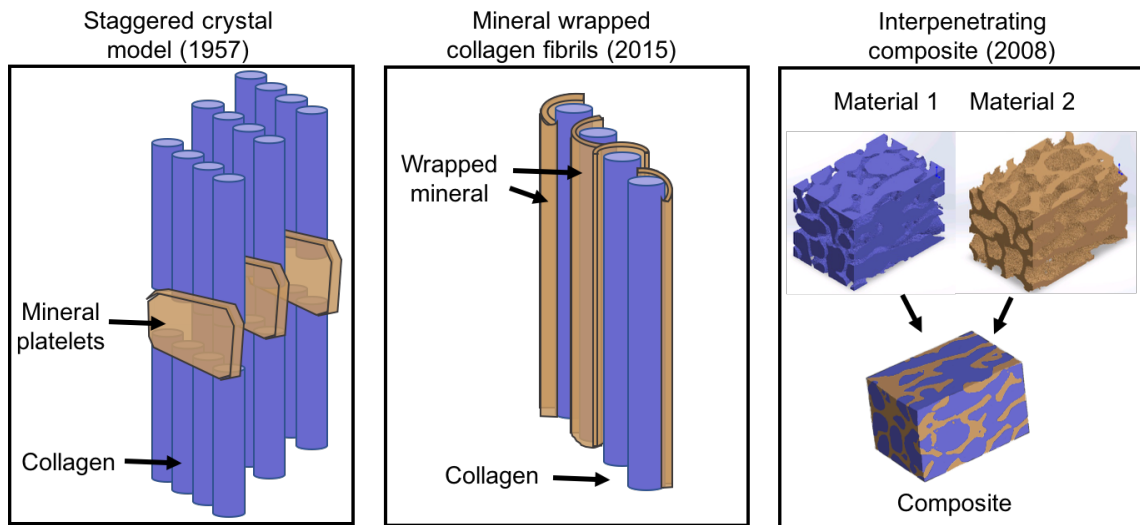


Figure 1.10. Nanoscale models of mineralized collagen in bone. The staggered crystal model [9], extrafibrillar mineral model [15], and composite with interpenetrating phases [17].

This doctoral dissertation explores the micro- and nanostructure of bone through 1) the isolation of component phases in bone, 2) determination of effects of geometric arrangement on 3D printed composites with soft and stiff phases, and finally 3) the synthesis of bioinspired materials through freeze casting. Isolation of each phases in bone through either deproteinization to remove the organic phase (collagen) or demineralization to remove the mineral phase (non-stoichiometric hydroxyapatite) was used to determine whether bone is an interpenetrating composite. In these isolation studies, the best chemical treatments to preserve the residual phases was found. The effect of material geometrical arrangement on mechanical properties is then explored through 3D printing and finite element modeling. The geometrical arrangements tested

include a discontinuous phase composite, a matrix inclusion composite with a stiff frame or soft frame, and an interpenetrating composite with either a stiff or soft phase. Size effects of 3D print features on mechanical properties of composites are also discussed. Last but not least, drawing inspiration from two collagen-hydroxyapatite composites (porcupine fish spines and bone), synthetic scaffolds are designed and created using freeze casting. The effect of microstructure and hydration on mechanical properties is discussed for the topics, respectively.

Chapter 1, in part, is a reprint of the material as it appears in “Deproteinization of cortical bone: Effects of different treatments” *Calcified Tissue International*, vol. 103, pp 554-556, 2018. The dissertation author was one of the primary investigators and authors on this paper. This paper was co-authored by Siyuan Pang, Yik Tung Tracy Ling, Peter Shyu, Ekaterina Novitskaya, Kyungah Seo, Sofia Lambert, Kimberlin Zarate, Olivia A. Graeve, Iwona Jasiuk, and Joanna McKittrick.

2 Deproteinization of Cortical Bone: Effects of Different Treatments

One way to better understand the mineral arrangement at the nanoscale is to deproteinize bone, i.e., remove the protein from bone. A few approaches have been employed in the past for isolating the mineral phase. These methods include calcination (thermal deproteinization), which uses high temperatures to degrade and combust organics. Collagen degradation occurs between 250–450°C and combustion between 450–700°C [41]. Calcination has been performed on fish [42], bovine [43, 44], and porcine [45] bones to isolate hydroxyapatite for bone scaffold applications. These studies have demonstrated differences in the thermal stability of hydroxyapatite between species, making calcination inconsistent between bones of different animals. Calcination was also found to increase the particle size of hydroxyapatite crystals through sintering [42, 46].

In contrast to deproteinization by calcination, chemical treatments have also been used to deproteinize bone. Hydrazine has been shown to be an effective method for deproteinization in bone and dentin research [47-50]; however, it is highly toxic and flammable. Deproteinization outcomes of bovine cancellous bone using 0.35 M sodium hypochlorite (NaOCl), 2 M peroxide (H₂O₂), 1 M potassium hydroxide (KOH) [51], and 1 M sodium hydroxide (NaOH) [52] solutions at 37°C were compared, where NaOCl and H₂O₂ treatments were found to be most effective [53]. Results from this study show that for NaOCl and H₂O₂ treated samples, ~11-13% of initial protein content was still present after 14 days of treatment. NaOH and KOH treatments were found to dissolve bone mineral after seven days of treatment. NaOCl has previously been shown to have minimal effects on mineral crystals in bone [54] and completely deproteinized bovine femur using NaOCl demonstrates that the mineral phase is continuous [38, 40]. Also,

porous structures at different length scales were preserved. Alkaline hydrolysis of fish bones using NaOH at 250°C was found to be more effective than calcination in preserving the size of hydroxyapatite crystals [42].

While most treatments measure the quantity of residual organic material, few papers explore the effects of different methods of deproteinization on the structure and composition of the resultant mineral phase. In addition, many previous studies destroy the microscale mineral structure by grinding bone into particles prior to deproteinization. The studies that have performed chemical deproteinization on intact bone use cancellous bone rather than cortical bone, which is used in this study. Therefore, this paper aims to determine the most effective method for complete cortical bone deproteinization without affecting the mineral structurally or chemically. By using four different deproteinization treatments, this study can help elucidate whether mineral in bone forms a continuous network. In addition to using deproteinization as a method to study the mineral phase of bone, deproteinized bone has biomedical applications as a bone scaffold.

2.1 Materials and Methods

2.1.1 Sample Preparation

Six-month-old porcine femur cortical bone (Animal Technologies Inc., Tyler, TX, USA) was first cut into samples of approximate dimensions $4 \times 2 \times 2$ mm using a diamond sectioning saw. Fine adjustments to sample dimensions were done with a variable speed grinder/polisher (VP-160, LECO Corporation, St. Joseph, MI, USA) with samples held in a custom-made sample holder and polished using a 600-grit sandpaper (BuehlerMet™ 2, Buehler, Lake Bluff, IL, USA) with water as the lubricant. All bone samples were prepared so that the longest dimension (4 mm) was parallel to the longitudinal direction of bone. Each sample was then submerged in a solution of either 0.35 M sodium hypochlorite (NaOCl) (Germicidal Ultra Bleach, WAXIE Sanitary

Supply, San Diego, CA, USA) [38], 1 M sodium hydroxide (NaOH) (Fisher Chemical, Pittsburgh, PA, USA) [52], 1 M potassium hydroxide (KOH) (P250-500, Fisher Chemical, Pittsburgh, PA, USA) [51], or 2 M hydrogen peroxide (H₂O₂) (H325-500, Fisher Chemical, Pittsburgh, PA, USA) [53] and placed on a rocker at room temperature for increased agitation during the chemical treatments. Hydrazine was not used in this study due to its toxicity and potential flammability. The solutions were changed daily, and treatments were halted every two days for analysis of protein content using thermogravimetric analysis. Two samples were prepared for each duration (every two days) together with two untreated samples, so that a total of 34 samples were tested. Treatment details including pH are summarized in Table 2.1. After each treatment, the samples were rinsed five times with deionized water.

Table 2.1. Deproteinization treatments.

Treatment	Concentration (M)	pH	Ionic Strength (M)	Duration of treatment (days)	Number of samples per duration
H ₂ O ₂	2.00	7.0	-	2, 4, 6	2
NaOCl	0.35	10.5	-	2, 4, 6	2
NaOH	1.00	14.0	1.00	2, 4, 6	2
KOH	1.00	14.0	1.00	2, 4, 6, 8, 10, 12, 14	2

2.1.2 Phosphate Ion Test

A phosphate ion test (Mars Fishcare Inc., Chalfont, PA, USA) was used to show whether phosphate ions, which are present in the mineral but not in the collagen, were leaching out during deproteinization treatments. While phosphate ions are present in some noncollagenous phosphoproteins [55-57], the relative quantities make it likely that phosphate ions from the mineral will have a much larger effect on the concentration observed through the phosphate ion test. The phosphate ion test uses an ammonium heptamolybdate solution together with a second solution of glycerol and stannous chloride to indicate the presence of phosphate ions, turning a

solution blue. Five samples were prepared with one of each treatment method and one untreated sample. After a day of treatment, 100 μL of the treatment solution was removed and placed in a test tube. Due to the high pH of NaOH and KOH solutions, the treatment solutions were diluted with 5 mL of deionized water. Six drops of the ammonium heptamolybdate were then added to the diluted treatment solutions and the test tube was shaken. Subsequently, six drops of the stannous chloride solution were added, and the mixture was agitated by shaking the vial.

2.1.3 Thermogravimetric Analysis

Thermogravimetric analysis (TGA) was used to determine protein content by mass after different intervals of each treatment (SDT Q600 Simultaneous TGA/DSC, TA Instruments, New Castle, DE, USA). Samples were heated in air from room temperature to 800°C at 10°C/min with a balance sensitivity of 0.1 μg . Samples were dabbed dry before TGA testing. For each treatment and number of days treated, two samples were analyzed using TGA. Results of TGA were analyzed according to Bigi, et al. [41], where mass loss up to 250°C is attributed to evaporated and bound water and mass loss between 250 and 700°C are attributed to collagen degradation and combustion.

2.1.4 X-ray Diffraction

X-ray diffraction (XRD) machine (Bruker D2 Phaser, Bruker, Billerica, MA, USA) with $\text{CuK}\alpha$ radiation was used to determine whether any of the chemical treatments had altered the crystal structure of the mineral in the post-treated bone. The scan rate of the test was 0.3 s per 0.014° increment and scans were performed in 20 to 70 degrees angle range. Prior to XRD, samples were dried by stepwise dehydration using ethanol and deionized water from 25 vol% to 100 vol% ethanol with 25 vol% increments with intervals of five minutes, with the 100% ethanol step done twice. Samples were then critically point dried using an Autosamdri-815 (Tousimis,

Rockville, MD, USA) with ethanol as the intermediate solvent. DIFFRAC.EVA software (Bruker, Billerica, MA, USA) was employed for XRD pattern analysis. Rietveld refinement was performed using TOPAS software (Bruker, Billerica, MA, USA) on one crushed sample of each treatment and untreated bone. The Scherrer equation was used to calculate c-axis and a,b-axis crystallite sizes. Details for Rietveld refinement and crystallite size calculation are described in Appendix A.

2.1.5 Scanning Electron Microscopy

Scanning electron microscopy (SEM) was used to observe the microstructure of the untreated and treated bone. Before imaging, the same drying procedure was used as for the XRD. Samples were then sputtered with iridium (Emitech K575X, Quorum Technologies Ltd, East Sussex, UK). Low-resolution imaging was performed using an environmental SEM (FEI/Philips XL-30, FEI, Hillsboro, OR, USA) with an acceleration voltage of 10kV. High-resolution images of the same samples were acquired using a field emission SEM (ZEISS Sigma 500, Carl Zeiss AG, Oberkochen, Germany) within a voltage range between 1 and 3 kV.

2.1.6 Raman Spectroscopy

Raman spectroscopy (RAMAN-11, Nanophoton, Osaka, Japan) was used to measure mineral and collagen compositions of bone by capturing a scattered light due to the difference of molecule and ion vibrations. The same drying procedure was employed as for XRD samples. Samples used for Raman were not crushed after treatment. A 785 nm laser with 1mW power was used for beam excitation. Each sample was scanned by line-imaging infrared through a 20×/0.3 objective with 100 s exposure time. The spectra wavenumbers were detected from 400 cm⁻¹ to 1800 cm⁻¹ as the critical collagen bands are present within this range [58, 59]. Baseline was corrected for fluorescence background by cubic spline interpolation. The spectrum intensity was

normalized to the primary phosphate band $\nu_1\text{PO}_4^{3-}$ at the wavenumber of 959 cm^{-1} such that every other peak represents the amount of value per $\nu_1\text{PO}_4^{3-}$ [60]. Raman spectrum also reveals fibril orientation effect from phosphate bands $\nu_1\text{PO}_4^{3-}$, while $\nu_2\text{PO}_4^{3-}$ is orientation independent. In this paper, only $\nu_1\text{PO}_4^{3-}$ was used to analyze the chemical composition as fibril orientation was not taken into account.

2.1.7 Delipidation

To remove as much organic material as possible, delipidation was considered due to the presence of fat in bone. While NaOH and KOH are both saponifiers that react with fats by hydrolysis to create a salt and an alcohol, NaOCl does not dissolve lipids. Therefore, a 2:1 chloroform-methanol solution was used to remove fat from NaOCl treated samples [61, 62]. Supercritical CO_2 treatment could also be used for delipidation [62, 63], but this was not attempted. Three different sequences of treatments were used combined with deproteinization: 1) deproteinization for 10 days, and then one day of defatting; 2) defatting for one day and then deproteinization for 10 days; and 3) defatting for one day, deproteinization for 10 days, and then defatting for one more day. Samples were then analyzed using Raman spectroscopy to determine whether the order of defatting influenced deproteinization outcomes.

2.2 Results and Discussion

Deproteinization was performed over the course of six days for treatments of H_2O_2 , NaOH, KOH, and NaOCl (photograph of samples is shown in Figure 2.1). At the end of the six-day treatments, the H_2O_2 treated samples showed little to no change in appearance when compared to untreated samples. NaOH and KOH treated samples appeared to expand in volume, and the resulting solids had enlarged cracks and vascular channels. The specimens were fragile

and difficult to handle. NaOCl treated samples became more brittle after deproteinization but did not change in shape or size. A change in color was observed in KOH, NaOH, and NaOCl samples, where the post-treatment specimens were white after protein removal. The lack of color change in H₂O₂ treated specimens may imply that the amount of protein is similar to the one in untreated bone.



Figure 2.1. Photograph of untreated (UT) porcine femur sample and specimens after six days of treatments using KOH, NaOH, NaOCl, and H₂O₂.

2.2.1 Scanning Electron Microscopy

Six-month-old porcine bone is primarily fibrolamellar, which is also known as plexiform or laminar bone [64-66]. This bone type is characterized by circumferentially arranged lamellae, vascular components, and a lack or a small number of osteons. Fibrolamellar bone has a different arrangement than mature bone and is observed in large, fast-growing mammals including pigs [67], cows [61, 68], sheep [68], and buffalo [65]. The microstructures of the deproteinized samples are shown in Figure 2.2, where larger images show overall structures and defects present in the specimens and the inset images are high-resolution micrographs of the mineral structure. In the micrographs, the bone image is oriented so that the longitudinal (parallel with lamellae) direction is in the plane of the page, meaning that features such as vascular compartments and lamellae run approximately vertically in the images.

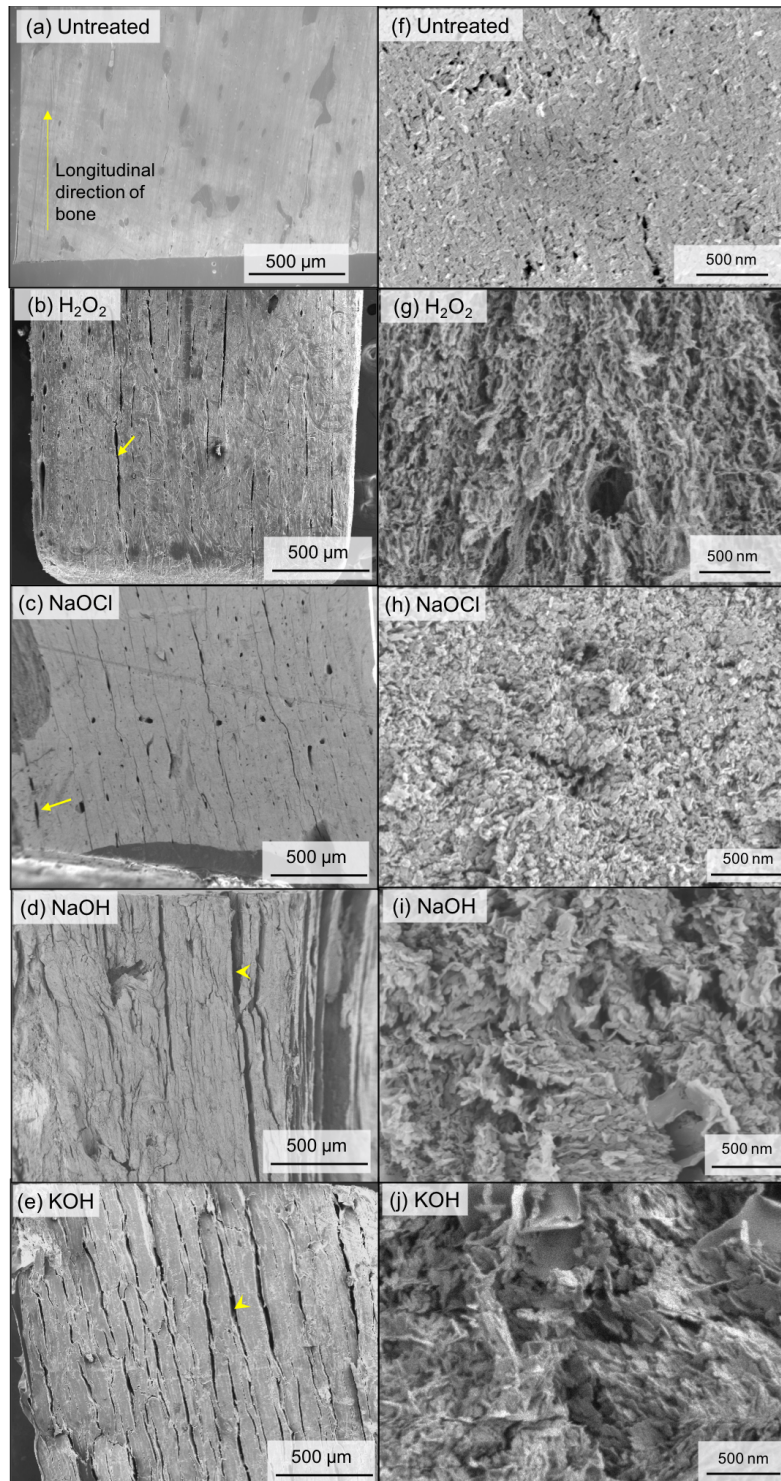


Figure 2.2. Scanning electron microscopy (SEM) images of untreated (**a,f**) and chemically treated samples using: (**b,g**) H_2O_2 , (**c,h**) NaOCl , (**d,i**) NaOH , and (**e,j**) KOH . (f), (g), (h), (i) and (j) are high resolution SEM images of each sample. The bone growth direction is in the plane of the page. Arrows in (b) and (c) point out longitudinal vascular compartments, and arrowheads in (d) and (e) show vascular compartments damaged by base treatments.

Untreated bone (Figure 2.2a) shows vascular channels generally aligned in the longitudinal direction. Both H₂O₂ (Figure 2.2b) and NaOCl (Figure 2.2c) treated bones show that the overall structure of the bone has not changed. In the H₂O₂ treated sample, vascular channels are visible after removal of some protein. In NaOCl treated samples, cracks form in the longitudinal direction of the bone. The NaOCl treated samples are brittle, which may contribute to the formation of cracks mostly in the longitudinal direction near the vascular compartments. Both NaOH (Figure 2.2d) and KOH (Figure 2.2e) treated samples exhibit a longitudinal crack formation. Additionally, it appears that the formation of these cracks expands the volume of the treated bone, as seen in Figure 2.1. From the phosphate ion test (Figure 2.3), NaOH and KOH treated specimens display a blue color, indicating the presence of dissolved phosphate ions. It has been known that calcium phosphates with low calcium-phosphate ratios dissolve in basic and neutral conditions and re-precipitate as hydroxyapatite [69]. Based on the pH of the basic treatments used (shown in Table 2.1), we hypothesize that the leaching of phosphate ions causes the remaining Ca ions to attract hydroxide ions, leading to hydrogen bonding from the surrounding water and the increase of bound water thereby creating swelling of the sample.

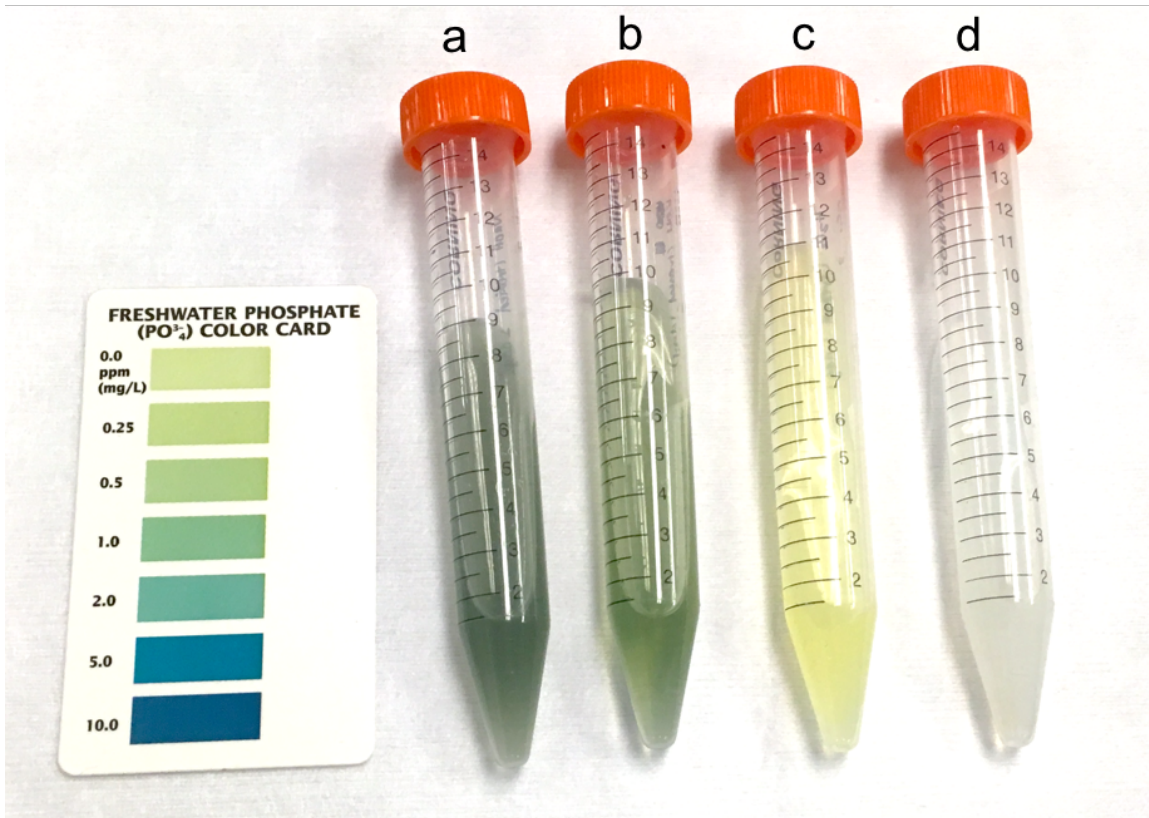


Figure 2.3. Phosphate ion test of different deproteinization treatment solutions after one day of deproteinization: (a) NaOH, (b) KOH, (c) H₂O₂, and (d) NaOCl.

Observing the high-resolution SEM images, mineral particles can be seen in untreated bone (Figure 2.2f). H₂O₂ treated samples (Figure 2.2g) exhibit a fibrous appearance, which may be a degraded, mineralized collagen. Mineral structures seen in untreated bone are most similar to those seen in NaOCl (Figure 2.2h) treated samples. The morphology of particles seen in the NaOCl treated samples match those described in the study performed by Weiner, et al. [54], even though species studied and length of treatment time (4 hours maximum) were different from the current study. Mineral platelets do not seem to be arranged in any larger pattern as was previously reported for deproteinized canine femur [70], bovine femur [71], armadillo and turtle osteoderms [71]; however, different species likely have different crystal morphologies [24, 72]. In contrast, NaOH (Figure 2.2i) and KOH (Figure 2.2j) treated samples exhibit larger, plate-like

features with sizes up to 500 μm . These large plate-like features may be re-precipitated hydroxyapatite that settles on the bone after treatment and have been seen by [38].

2.2.2 Thermogravimetric Analysis

Thermogravimetric analysis results of the deproteinized samples are shown in Figure 2.4. After the first six days of treatment, H_2O_2 yielded no change in weight percentage of protein and therefore was not found to be effective at removing protein. The base treatments, NaOH and KOH, decreased the weight percentage of both mineral and organic material in bone. Upon closer examination and comparison of total weights in the treated samples (Table 2.2), it can be observed that while organic material decreases slightly in weight, the largest change is an increase in water [53]. This suggests that the basic treatments dissolve bone mineral. However, this is not observed in the current experiment. The large increase in water matches with the SEM observations, where it is seen that the overall treated sample and its cracks expand after treatments with NaOH and KOH.

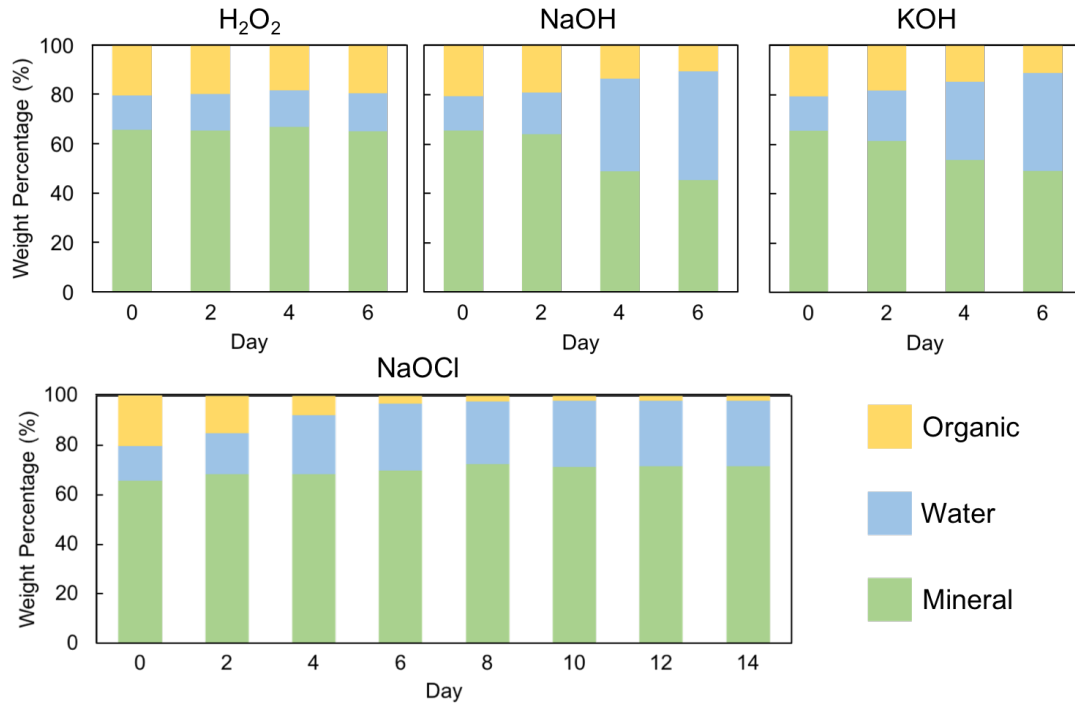


Figure 2.4. Thermogravimetric analysis taken over six days for samples treated with H₂O₂, NaOH, and KOH and for 14 days with NaOCl. Yellow represents weight percentage of organic materials, while blue and green represent weight percentages of water and mineral, respectively. TGA was performed up to 800°C.

The treatment with NaOCl proved to be the most effective, decreasing the amount of organic material while retaining the mineral. This treatment was extended to 14 days to determine the maximum possible deproteinization amount. However, even after 14 days, ~2 wt.% organics were still present in bone samples. This may be a result of the much denser structure of cortical bone, which makes the proteins difficult to remove entirely when compared to the trabecular bone that was successfully deproteinized previously [38, 39, 73]. It has also been suggested that since NaOCl does not dissolve the mineral, residual organics may be collagen encapsulated in the mineral [74]. Table 2.2 shows that mineral weight in NaOCl treated samples stays consistent, while the weight of organics decreases dramatically. The increase in the weight of water can be attributed to water replacing the physical spaces that were once occupied by the organics.

Table 2.2. The average weight of bone constituents by thermogravimetric analysis during four chemical treatments (n=2).

Treatment	Day	Water weight (mg)	Organic weight (mg)	Mineral weight (mg)	Total weight (mg)
Untreated	0	4.2601	6.4824	19.9971	30.7396
	2	5.0862	6.8300	22.5088	34.4251
H ₂ O ₂	4	4.4632	5.6072	20.3572	30.4276
	6	4.0166	5.0954	16.9560	26.0680
NaOH	2	5.8434	6.5556	22.1101	34.5091
	4	14.54321	5.1429	18.3562	38.0423
	6	20.1997	4.8632	20.7156	45.7785
KOH	2	7.0704	6.4162	21.6035	35.0901
	4	12.3453	5.7487	20.9702	39.0642
	6	15.4067	4.2736	18.9311	38.6114
NaOCl	2	5.2465	4.8194	21.7829	31.8489
	4	7.5077	2.4807	21.6185	31.6070
	6	7.9548	0.9917	20.5031	29.4497
	8	7.3059	0.7376	20.9838	29.0272
	10	8.4755	0.6691	22.4531	31.5978
	12	7.3720	0.5736	20.0229	27.9685
	14	8.1637	0.6275	21.9099	30.7011

With the exception of H₂O₂ having little to no effect on the protein content in bone, these results agree with previously observed results on bovine cancellous bone studied by [53].

Comparing the final weight of organics to the original weight in untreated bone, it was found that like Uklejewski's results, ~9 wt.% of the original organics remained after 14 days of NaOCl treatment. One difference to note in the methods is that all treatments in this paper are performed at room temperature, while treatments in the previously mentioned paper were done at 37°C. This may explain, for example, the large difference in the effectiveness of the H₂O₂ treatment.

2.2.3 X-ray Diffraction

Figure 2.5a summarizes X-ray diffraction results of treated and untreated samples and demonstrates that there is no change in the crystal structure or crystallite size after the various

six-day deproteinization treatments when compared to the untreated bone. Deproteinized specimens whose spectra shown in Figure 2.5a were not ground down prior to XRD analysis to discern whether composition as well as orientations of the mineral crystals were affected by the deproteinization treatments. Spectra of treated samples were compared with the powder diffraction file (PDF) for hydroxyapatite (PDF 00-055-0592) [75], it is observed that the relative intensities of reflections do not match the PDF as predicted. Specifically, the peaks at 2θ values of 32.9° , 46.7° , 58.1° , and 63.0° match, while peaks at $2\theta = 21.2^\circ$, $2\theta = 38.6^\circ$, and $2\theta = 52.5^\circ$ do not match those of the PDF. The presence and absence of certain peaks can be attributed to the preferential alignment of hydroxyapatite *c*-axis in the longitudinal direction of the bone [76]. It is important to point out that the spectra show no differences after deproteinization treatments, meaning that minerals have not been altered during the process and that the arrangement of the mineral is preserved since the relative intensities of peaks are similar. Rietveld refinement results (Table A.1) show that the calculated lattice parameters of treated samples are comparable to those of untreated samples. Crystallite sizes for the *c*-axis and *a,b*-axes (Table A.2) are similar between all samples and to those found in literature [77]. This is somewhat at odds with earlier results showing that mineral dissolves in NaOH and KOH treatments. However, since the dissolved mineral re-precipitates as hydroxyapatite [69], it does not change the XRD spectra, and the mineral arrangement may also be similar until the mineral is dissolved and the solid collapses.

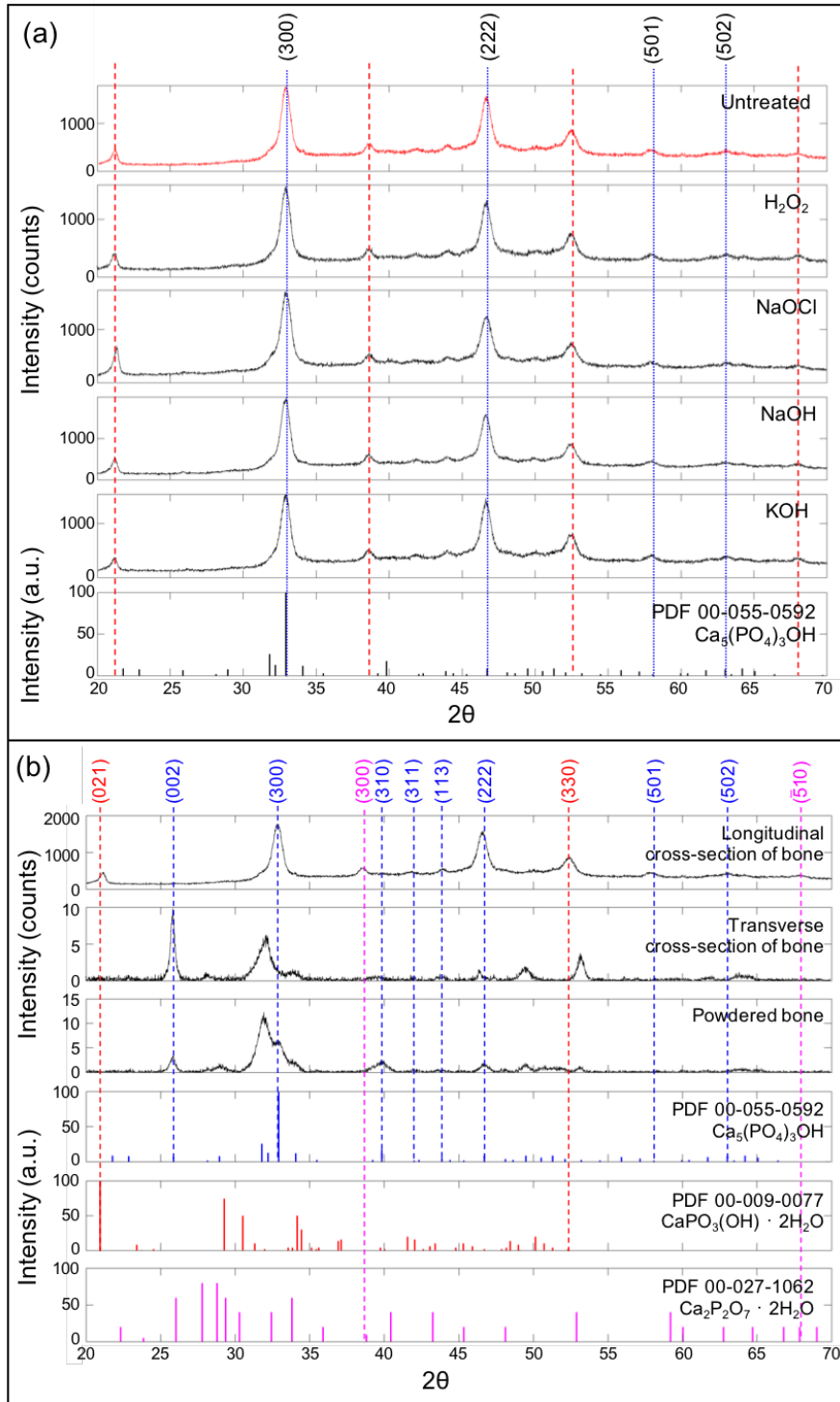


Figure 2.5. (a) X-ray diffraction patterns of untreated and chemically treated samples. Blue dotted lines indicate peaks that match those of the PDF for hexagonal hydroxyapatite. Red dotted lines indicate peaks that do not match or are shifted. (b) X-ray diffraction of intact, untreated bone in different orientations compared to deproteinized, powdered bone along with the powder diffraction file for hydroxyapatite (blue), brushite hydrate (red), and calcium phosphate hydrate (pink).

Figure 2.5b demonstrates that an alignment of bone mineral affects the resulting XRD spectra depending on the orientation used for testing. Since the unmatched peaks at $2\theta = 21.2^\circ$ and $2\theta = 38.6^\circ$ for longitudinally tested samples are not found in hydroxyapatite, DIFFRAC.EVA was used to search for compounds containing Ca, P, O, and H with powder diffraction files that contain the unmatched peaks. The peaks seem to correspond with $\text{CaPO}_3\text{OH}\cdot 2\text{H}_2\text{O}$ (brushite hydrate) and $\text{Ca}_2\text{P}_2\text{O}_7\cdot 2\text{H}_2\text{O}$ (calcium pyrophosphate dihydrate); both thought to be intermediate products of bone hydroxyapatite formation [78-80]. Since preferential alignment of hydroxyapatite in bone influences the peaks that are detectable, it was assumed brushite hydrate and calcium pyrophosphate dihydrate may be similarly textured and additional peaks may not be visible. While hydroxyapatite is the most stable form of calcium phosphate at body temperature and pH, it is possible that brushite forms and is maintained in the presence of Mg^{2+} ions that severely inhibit hydroxyapatite crystal growth [81]. The presence of octacalcium phosphate, which is hypothesized to be present in bone [82], could not be verified since the primary peak occurs at $2\theta=4.7^\circ$ and is outside of the range of the XRD instrument used in this study. Powdered samples of the deproteinized bone exhibit peaks that match with the hydroxyapatite PDF.

2.2.4 Raman Spectroscopy

Having determined through SEM and TGA that NaOCl is the most effective deproteinization method, Raman spectroscopy was used to detect the chemical composition of the residual protein in the bone samples throughout 14 days of treatment with NaOCl. Collagen bands at wavenumbers around 853 cm^{-1} , 872 cm^{-1} , $1242\text{-}1340\text{ cm}^{-1}$, 1446 cm^{-1} , $1660\text{-}1690\text{ cm}^{-1}$ corresponding to proline, hydroxyproline, amide III, protein CH_2 deformation, and amide I bands

were marked [59]. For the mineral bands, the primary phosphate band $\nu_1\text{PO}_4^{3-}$ at 959 cm^{-1} , $\nu_2\text{PO}_4^{3-}$ at 428 cm^{-1} , $\nu_4\text{PO}_4^{3-}$ at 590 cm^{-1} , and carbonate band $\nu_1\text{CO}_3^{2-}$ at 1070 cm^{-1} were marked [59].

Raman spectroscopy results are shown in Figure 2.6. The collagen bands of proline, hydroxyproline, amide I, and CH_2 deformation were eliminated after the 4th day of treatment. However, a small amount of the amide III band was still visible after a 14-day treatment. Statistical significance of the amide III band was calculated using one-way ANOVA and is summarized in Table 2.3. The area under the amide III band was largely scattered for the 4-day treatment, leading to statistically insignificant results when compared with 8-day, 10-day, 12-day, and 14-day treatments, as the deproteinization reaction may not have been fully completed for the whole sample. The deviation became smaller with the longer treatment time since collagen was gradually removed. The amount of amide III remaining decreased during a 10-day treatment. During the 10 to 14-day treatments, the residual amide III band became more stable, but still could not be fully eliminated. Since a decreasing trend was observed as treatment time increased, and there was still a significant difference ($p < 0.05$) between 12-day and 14-day amide band area, a longer treatment time could be investigated in the future. The analysis of mineral-to-matrix ratio ($\nu_1\text{PO}_4^{3-} / \text{amide III}$), carbonate-to-mineral ratio ($\nu_1\text{CO}_3^{2-} / \nu_1\text{PO}_4^{3-}$), and crystallinity ($1/\text{FWHM of } \nu_1\text{PO}_4^{3-}$) were calculated for different treatment days as shown in Figure 2.7. Due to the elimination of amide III bands, the mineral-to-matrix ratio increased significantly after 14-day treatment ($p < 0.05$). However, both carbonate-to-mineral ratio and crystallinity did not show statistical change ($p > 0.05$) during the treatment period. It was also observed that the phosphate bands ($\nu_1\text{PO}_4^{3-}$) and the carbonate and phosphate bands ($\nu_1\text{CO}_3^{2-}$ and $\nu_3\text{PO}_4^{3-}$) that overlapped at wavenumbers between 1035 cm^{-1} to 1076 cm^{-1} did not change after the 14-day treatment. These results indicate that the deproteinization process removed most of the collagen while preserving

the mineral content and crystallinity of the crystals in bones.

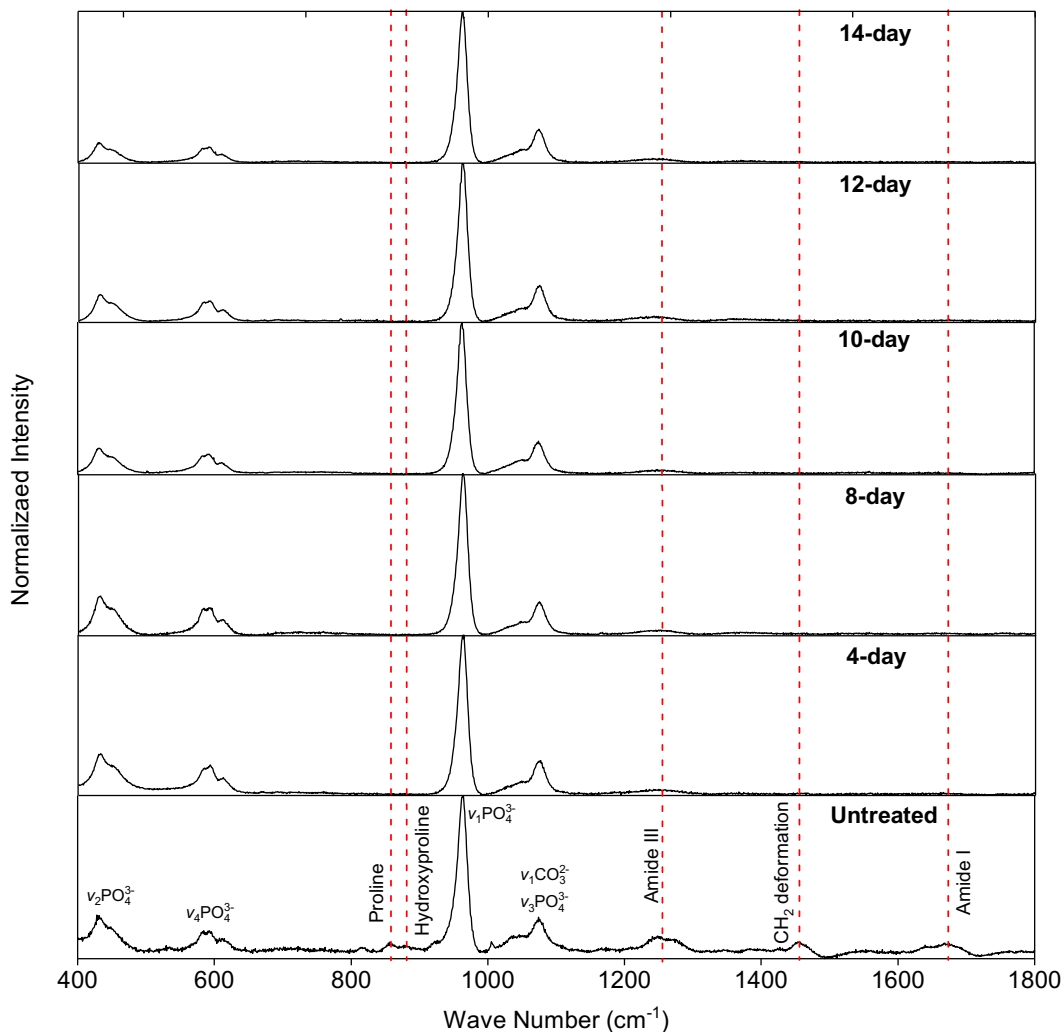


Figure 2.6. Raman spectra of untreated bone and samples treated with NaOCl (4, 8, 10, 12, and 14 days). Red dotted lines indicate bands associated with collagen.

Table 2.3. Statistical significance between each treatment duration presented by *p*-value.

Untreated	4-day	8-day	10-day	12-day					
4-day	<i>p</i> <0.05	8-day	<i>p</i> >0.05	10-day	<i>p</i> >0.05	12-day	<i>p</i> >0.05	14-day	<i>p</i> <0.05
8-day	<i>p</i> <0.05	10-day	<i>p</i> >0.05	12-day	<i>p</i> >0.05	14-day	<i>p</i> <0.05		
10-day	<i>p</i> <0.05	12-day	<i>p</i> >0.05	14-day	<i>p</i> <0.05				
12-day	<i>p</i> <0.05	14-day	<i>p</i> >0.05						
14-day	<i>p</i> <0.05								

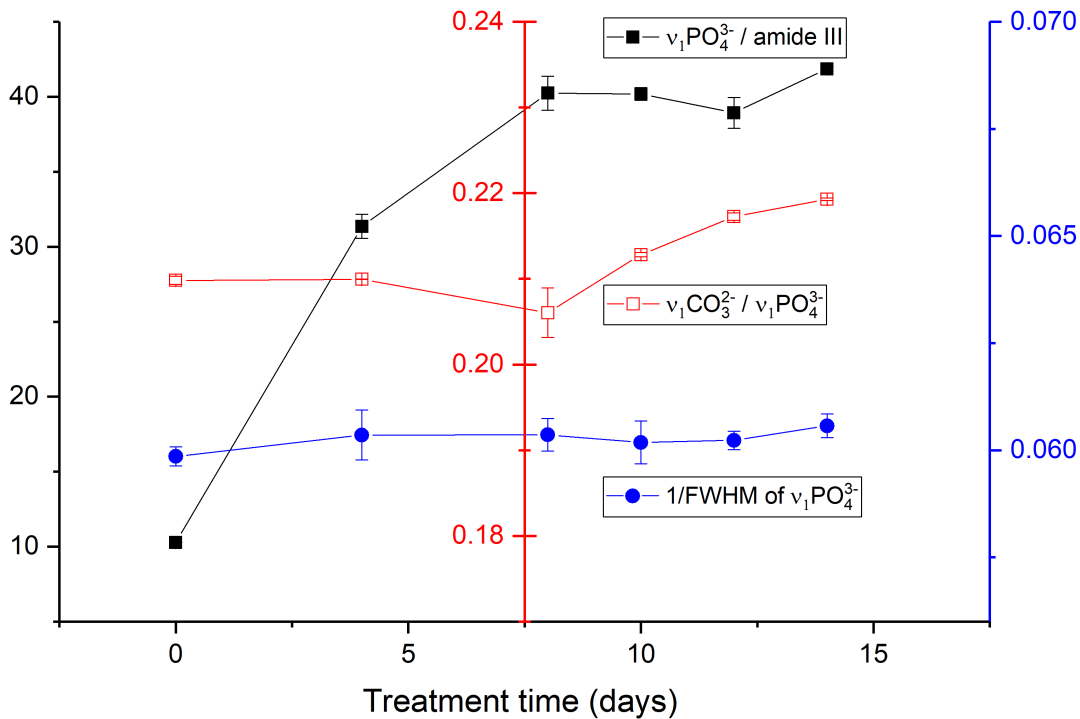


Figure 2.7. The mineral-to matrix ratio ($\nu_1\text{PO}_4^{3-} / \text{amide III}$), carbonate-to-mineral ratio ($\nu_1\text{CO}_3^{2-} / \nu_1\text{PO}_4^{3-}$), and crystallinity ($1/\text{FWHM of } \nu_1\text{PO}_4^{3-}$) calculated from Raman imaging for untreated bone and samples treated with NaOCl for 4, 8, 12, and 14 days given as average \pm S.D. (standard deviation).

The existing signals under amide III ($1242\text{-}1340\text{ cm}^{-1}$) band may be due to other organics. Lipids are possible components present at that wavelength. Czamara *et al.* [83] reported a low-intensity signal of $=\text{C-H}$ bending at around 1260 cm^{-1} for lipids, which appears under the amide III band in the experiments. Delipidation may determine if the signals observed under amide III bands were from lipids.

Delipidation using chloroform-methanol solution was performed on samples in addition to deproteinization using NaOCl. The three treatment sequences were deproteinization and then defatting (DP-DF), defatting and then deproteinization (DF-DP), deproteinization, defatting, and then deproteinization (DP-DF-DP). After the treatments, the samples were compared using Raman spectroscopy. The sequence of deproteinization and defatting treatments, shown in

Figure 2.8, exerted little effect on collagen bands, and the amide III band was not eliminated. The observation implies the bands detected at 1260 cm^{-1} are not likely due to the presence of lipids. The retained signals under amide III band were not removed by either the 14-day treatment or defatting process, indicating that we may need longer deproteinization and defatting treatments or that there is some other organic that the treatments do not remove.

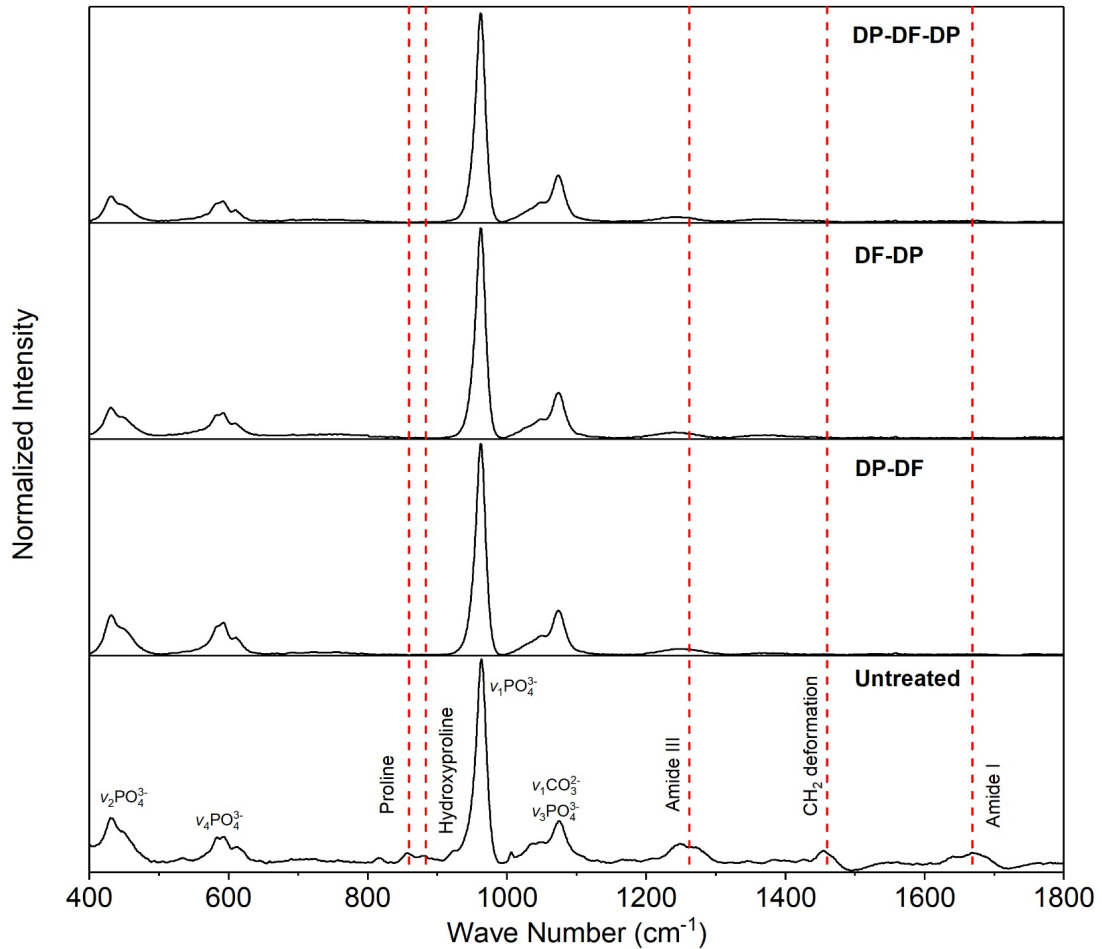


Figure 2.8. Raman spectroscopy of untreated bone and three different sequences of treatments: DP-DF (deproteinization, then defatting); DF-DP (defatting, then deproteinization); and DP-DF-DP (defatting, deproteinization, and then defatting again). Red dotted lines indicate bands associated with collagen.

2.3 Conclusions

This paper describes the results of different chemical deproteinization methods on porcine cortical bone. Deproteinization was carried out with sodium hypochlorite (NaOCl), hydrogen peroxide (H₂O₂), sodium hydroxide (NaOH) or potassium hydroxide (KOH). The treated samples were evaluated by thermogravimetric analysis (TGA), X-ray diffraction, scanning electron microscopy (SEM) and Raman spectroscopy. In addition, samples were defatted to remove any possible lipids present in the samples. The goal was to determine the best treatment that removes the most organic material while preserving the mineral crystal structure and microstructure. The major findings from the experiments are:

- NaOCl with a concentration of 0.35 M in water is the most effective method for deproteinization while maintaining the structure of the mineral.
- Other methods such as 2 M H₂O₂, 1 M NaOH, and 1 M KOH solutions have little to no effect on the amount of remaining protein.
- SEM showed that H₂O₂ and NaOCl treatments damaged the mineral less than NaOH and KOH, which were destructive to the mineral microstructure through leaching of phosphate ions. Comparison of high-resolution images showed that the microstructure of NaOCl treated bone was most similar to that of untreated bone.
- X-ray diffraction showed that chemical treatments resulted in no changes to the carbonated apatite crystal composition and structure. The effect of phosphate ion leaching in the base-treated samples may not be significant enough to change XRD spectra, since dissolved calcium phosphates re-precipitate as hydroxyapatite.
- Raman spectroscopy showed that the collagen bands were mostly eliminated after four days of NaOCl treatment and the amide III band was still detected in samples after 14

days of treatment. The mineral-to-matrix ratio showed that the amide III band decreased dramatically after 10 days but still could be detected in samples after 14 days of treatment. Carbonate-to-mineral ratio and mineral crystallinity analysis indicated that the mineral content and crystallinity were preserved during the 14-day deproteinization treatment.

- The delipidation process in bone combined with deproteinization showed no difference in the Raman spectra. In addition, the existing signals around 1260cm^{-1} were not eliminated by defatting treatment, which indicates the retained bands under amide III peak were not components of lipid.

The findings of this study support the hypothesis that bone is an interpenetrating composite with a continuous mineral phase. The addition of a delipidation process shows that other organics do not contribute to supporting the mineral phase, and that the mineral is a self-standing network. Despite the fact that it remains unclear whether the mineral is held together by residual lipids and proteins or by van der Waals forces, this information can be used to develop more reliable nanoscale models of bone.

Chapter 2, in part, is a reprint of the material as it appears in “Deproteinization of cortical bone: Effects of different treatments” *Calcified Tissue International*, vol. 103, pp 554-556, 2018. The dissertation author was one of the primary investigators and authors on this paper. This paper was co-authored by Siyuan Pang, Yik Tung Tracy Ling, Peter Shyu, Ekaterina Novitskaya, Kyungah Seo, Sofia Lambert, Kimberlin Zarate, Olivia A. Graeve, Iwona Jasiuk, and Joanna McKittrick.

3 Demineralization of Cortical Bone using Several Protocols and Synthesis of a Collagen Scaffold

Bone is a natural composite material with a complex structure that gives bone high strength and high toughness that is required for its diverse functions while being light-weight [31, 84]. The structural organization of bone involves several hierarchical levels [22, 84, 85]. The macroscale (larger than 10 mm) represents a whole bone, while the mesoscale ($\sim 500 \mu\text{m}$ to 10 mm) includes cancellous and cortical bones. The microscale ($\sim 10 \mu\text{m}$ to $500 \mu\text{m}$) consists of osteons (cortical bone) and trabeculae (cancellous bone) which at the sub-microscale ($\sim 1\text{--}10 \mu\text{m}$) are made of lamellae. At the nanoscale lamellae contain collagen fibrils ($\sim 50\text{--}100 \text{ nm}$ in diameter) mineralized with intra- and extra-fibrillar hydroxyapatite crystals ($\sim 50 \times 25 \times 3 \text{ nm}^3$). Bone is a composite material made of organic components (90% type I collagen and 10% non-collagen proteins), inorganic phase (mineral), and water, that occupy around 40, 40, and 20 vol% of bone, respectively [24].

Collagen is the most abundant protein in mammals, and is thus of high scientific, archaeological, and clinical interests. Bone nanostructure can be studied by comparing untreated and demineralized bone (e.g., [73]). Collagen fibril organization of bone can be analyzed by transmission electron microscopy of demineralized bone samples (e.g., [86]). In archaeological studies, collagen is being isolated from bone for radiocarbon dating (e.g., [87]). Also, stable isotope ratios of carbon and nitrogen from bone collagen and minerals provide diet information (e.g., [88]). Clinically, collagen has been used for tissue constructs and scaffolds for humans [89-92] and animals [93-95]. For example, a commercially purchased allogenic human freeze-dried demineralized bone matrix (DBM) was incorporated into human dental implantation and found

to improve bone formation at bone-implant interface [92]. Two DBM products, Flex-DBM and Putty-DBM, have been used as graft materials for rat bones, which resulted in a better formation of new bone than in control groups [94]. The transplantation of demineralized rat dentin matrix into three species (pig, mouse, and rat) showed that fibroblasts were transformed by the collagen implantation [95]. To produce DBM, bone is usually first ground into particles ranging from 100 – 500 μm or cut into other small units. Bone is demineralized with either HCl or ethylenediamine tetraacetic acid (EDTA) and studies focus on the ability of DBM for cell growth. While DBM seems to be useful for new bone formation, the processing methods result in the loss of the hierarchical structure of bone. Therefore, it is still not well understood how demineralization methods affect overall collagen structure, and thus, more studies are needed on how to obtain high-quality DBM for various applications. Additional studies can also provide further insights into the collagen architecture in bone, and on collagen properties in general.

Demineralization agents such as EDTA, hydrochloric acid (HCl), formic acid (CH_2O_2), and citric acid have been employed [96-100] to obtain isolated collagen. The reaction rate, demineralization efficiency, and the effect on residual collagen were taken into account by previous studies when comparing different agents. The chemical solutions can be categorized as organic acids such as acetic, formic, or citric; inorganic acids such as hydrochloric, nitric or sulfuric; and calcium chelating solutions such as EDTA [100]. EDTA [101, 102] and HCl [39, 40, 73, 103-105] are the most common agents for demineralization. The selection of EDTA is mainly due to its ability to preserve tissue antigenicity [39, 103, 104]. In contrast, some studies concluded that HCl would alter the collagen morphology and antigenicity. A comparison of 0.1M EDTA and 0.6M HCl found that EDTA resulted in an almost intact, hierarchically ordered collagen structure, while the hydrolysis induced by HCl destroyed the collagen structure [103].

Several studies used CH_2O_2 as a demineralization agent [97, 106], and this agent is considered more effective at demineralization than EDTA as it requires less time to remove retained chemicals from bone samples, and can remove minerals as much as EDTA [96]. A newly proposed solution called ETDA (HCl/EDTA mixture) is a mixture of 12% HCl (3.3 M), 0.07% EDTA (2.4 mM), 0.014% sodium tartrate ($\text{C}_4\text{H}_4\text{O}_6\text{Na}_2$) (0.72 mM), and 0.8% potassium tartrate ($\text{KNaC}_4\text{H}_4\text{O}_6 \cdot 4\text{H}_2\text{O}$) (28 mM) in water [100]. This study showed that the HCl/EDTA mixture performed similarly to EDTA to remove minerals with preservation of the collagen structure, but the reaction rate was far more rapid than that of EDTA. However, the collagen integrity after the HCl/EDTA mixture treatment was only determined by observing the collagen morphology. A more quantitative study should be conducted to investigate the effectiveness of this method. So far, comparison studies have used a formalin-fixed bone as a starting material of demineralization since most comparison studies use demineralization for histology sample preparation. This fixation affects not only the chemical properties but also the mechanical properties of demineralized bone. A comparison study of demineralization methods using unfixed bone has yet to be published and is the subject of the current study.

Several experimental techniques have been used to qualitatively and quantitatively determine the efficiency of removing the mineral and preserving the structural integrity of the collagen. Raman and Fourier-transform infrared (FTIR) spectroscopies have been used to evaluate the chemical composition of demineralized bones [107-109]. However, at present, there are no studies that use both Raman and FTIR spectroscopies to compare different demineralization agents and quantitatively analyze the mineral and collagen components. Raman and FTIR spectroscopies illustrate the intensity of functional groups in terms of wavenumbers. The molecule transition has to undergo a dipole moment change during vibration to be detectable

through FTIR. For the Raman spectroscopy, the molecule must have a positional change [110]. Therefore, both FTIR and Raman spectroscopies should be performed to complement and validate results since some functional groups that cannot be detected by one technique can be measured by the other. In addition to spectroscopy, researchers studied the DBM that was demineralized by HCl, CH_2O_2 , or EDTA using a scanning electron microscope to observe the collagen structure under high magnification [104, 106, 111, 112], and using a thermogravimetric analysis [113, 114] to measure the weight percentage of compositions in demineralized bone.

Since collagen structure is lost when producing DBM using traditional methods, in which bone is first ground into particles, it would be useful to be able to mimic the structure of bone for clinical studies. One method of doing so is a technique called freeze casting or ice templating, which makes solids with interconnected porosity. This method usually employs the use of a slurry of ceramic particles suspended in a solvent. The slurry is frozen during which the particles are separated from the solvent and form walls. The experimental setup for freeze casting is shown in Figure B.1 in Appendix B. After freezing, the solvent is sublimated, leaving interconnected pores where the solvent originally was. Post-processing can be done to improve mechanical properties such as sintering in the case of ceramic freeze casting [115]. When used with water as a solvent and frozen directionally, lamellar microstructure can be formed that are similar to those found in cancellous bone [14, 116]. While the process is commonly used with ceramic particles, it has been used for hydrogels [117] and, more recently, collagen [118]. This method shows promise as a way to give DBM an organized structure for cells to potentially grow on.

In this paper, we focus on four demineralization agents: EDTA, HCl, CH_2O_2 , and the EDTA (HCl/EDTA mixture). The effectiveness of these chemical treatments on the

demineralization process of bone and their influence on collagen are examined. Several characterization techniques are employed: Raman spectroscopy, FTIR spectroscopy, thermogravimetric analysis (TGA), and scanning electron microscopy (SEM). One-way ANOVA (analysis of variance) is performed for statistical analysis. Finally, using the HCl treatment to demineralize six-month-old porcine femur, collagen is extracted from bone and freeze cast into a porous collagen scaffold. The objective of this study was to identify best demineralization protocols to obtain high-quality collagen from bone for scientific studies focusing on medical applications.

3.1 Materials and Methods

3.1.1 Sample Preparation

Femurs from six-month-old pigs were obtained from the Meat Science Lab at the University of Illinois at Urbana-Champaign and Animal Technologies, Inc. (Tyler, TX, USA). Cortical bone was cut into dimensions of 2 mm x 2 mm x 4 mm by a diamond blade sectioning saw (Isomet 1000, Buehler, USA), and smoothed using 1200 grit sandpaper. The samples were then submerged into solutions at room temperature of either 1M EDTA (E9884, Sigma-Aldrich, St. Louis, MO, USA), 0.5M CH₂O₂ (ACROS Organics, New Jersey, USA), 0.5M HCl (EMD Millipore Corporation, Billerica, MA, USA), or the HCl/EDTA mixture. The samples were placed on a rocker to ensure agitation. Solutions were changed each day. Specimens submerged in HCl, CH₂O₂, and the HCl/EDTA mixture were treated until they were translucent, defined as an endpoint. EDTA-treated samples did not become transparent, so these samples were weighed to determine the endpoint. For the weight loss method, samples were removed from the solution, dabbed dry with a tissue, and weighed. If the weight decreased, the solution would be changed, and the sample would be treated for another day. After each treatment, samples were placed in a

sonicator for 15 minutes with deionized water to rinse residual chemicals. The water was rinsed five times for five minutes. A brief description of the sample preparations is shown in Table 3.1.

Table 3.1. Sample preparation by demineralization agents: EDTA (ethylene-diamine tetraacetic acid), formic acid (CH_2O_2), hydrogen chloride (HCl), and HCl/EDTA mixture.

Agents	Concentration	Treatment time	Brief procedures
Untreated	N/A	N/A	Cut samples to 2 mm x 2 mm x 4 mm; polish; demineralization treatments on an agitation rocker until the samples were translucent (except for HCl/EDTA mixture – endpoint was based on the weighing method; remove chemicals by a sonicator; rinse samples by deionized water; dehydration by ethanol; critical point drying.
EDTA	1M	7 days	
CH_2O_2	0.5M	2 days	
HCl	0.5M	7 hrs.	
HCl/EDTA mixture	3.3M HCl, 2.4 mM EDTA, 0.72 mM $\text{C}_4\text{H}_4\text{O}_6\text{Na}_2$, 28 mM $\text{KNaC}_4\text{H}_4\text{O}_6 \cdot 4\text{H}_2\text{O}$	3 hrs.	

3.1.2 Raman Spectroscopy

The samples prepared for Raman spectroscopy were dehydrated in water/ethanol solutions where the ethanol concentration was gradually elevated from 25%, 50%, 75%, to 100 vol. %, each for five minutes. After being critical point dried (Autosamdri-931 Series Supercritical Point Dryer, Tousimis, Rockville, MD, USA), samples were then imaged with a Raman spectrometer (NanoPhoton Raman 11, Osaka, Japan). A 785 nm laser with 1 mW power for 100 seconds of exposure was employed, and a 20x/0.45 objective was used with line-imaging infrared for scanning. The baseline drift due to fluorescence background was subtracted by cubic spline fitting [119]. Three samples from each treatment and untreated bones were tested.

To quantitatively assess the effectiveness of the demineralization chemicals and measure level of mineralization, the mineral-to-matrix ratio, which is the intensity ratio of the primary phosphate band at $\nu_1\text{PO}_4^{3-}$ to the amide I band at 1660 cm^{-1} was calculated [120, 121]. The mineral crystallinity is expressed by the inverse of full-width-half-maximum (1/FWHM) of the

$\nu_1\text{PO}_4^{3-}$ [60, 122-124]. The smaller the value of FWHM, the better the mineral crystals are ordered [58]. The collagen quality parameter, defined as the band area ratio of 1660 cm^{-1} to 1690 cm^{-1} under the amide I envelope, was determined [120, 121].

3.1.3 Fourier-Transform Infrared Spectroscopy

FTIR samples were prepared using the same method described in Section 2.2. The spectra were collected in the absorbance mode in air with $\sim 25\text{ N}$ of force applied to the specimen measurement surface using an ATR Spectrum Two (PerkinElmer, Waltham, MA, USA). A background spectrum was first taken every thirty minutes to ensure accurate background subtraction from the spectra using Spectrum 10™ software (PerkinElmer, Waltham, MA, USA). The baseline of each spectrum was corrected by the same methods as for Raman spectroscopy. Measurements were performed on three samples for each treatment case and untreated bone.

3.1.4 Scanning Electron Microscopy

After demineralization treatments were performed, samples were fixed with neutral buffered formalin for one day to prevent sample degradation. Specimens were then rinsed and dehydrated using the methods described in Section 2.2. Subsequently, samples were embedded in epoxy (Epoxicure 2 Resin and Hardener, Buehler, USA) and the surface was smoothed with a Leica Ultracut UCT ultramicrotome (Leica Biosystems, Wetzlar, Germany) with a diamond knife. Specimens were sputtered with iridium in an Emitech K575X (Quorum Technologies Ltd, East Sussex, UK). A field emission SEM (ZEISS Sigma 500, Carl Zeiss AG, Oberkochen, Germany) was employed to image the collagen structure. The voltage range used was between 1 and 3 kV.

Energy dispersive X-ray spectroscopy (EDS) was performed on each sample using the IXRF Iridium Ultra (IXRF Systems, Inc., Austin, TX, USA) at 20 kV to measure an atomic

percentage and a weight percentage of the main elements in bone: C, N, O, P, Ca, and Na.

Iridium Ultra uses the ZAF algorithm to calculate mass and atomic percentages.

3.1.5 Thermogravimetric Analysis

Specimens were dehydrated using the same methods as described in Section 2.2. After dehydration, specimens were heated from room temperature to 800°C at 10°C/min in a TGA instrument (Pyris 1, PerkinElmer, Waltham, MA, USA). For mineralized collagen, 250°C is the point where all free and bound water is evaporated, and collagen decomposition and combustion take place from 250°C to 750°C [41]. The remaining solid after 750°C is the mineral. Two samples of each treatment and two untreated samples were tested.

3.1.6 Collagen Extraction and Freeze Casting

Collagen was extracted from demineralized bone using a process similar to that described in Rajan, et al. [125]. Collagen was then dissolved in 0.05 M acetic acid solution to make a 2 wt% collagen solution similarly as in Divakar, et al. [118]. Scaffolds were freeze cast in a polyvinyl chloride mold at a cooling rate of -10°C/min, after which samples were lyophilized. The resulting scaffold was then crosslinked in a solution of 33 mM 1-Ethyl-3-(3-dimethylaminopropyl)-carbodiimide (EDC), 6 mM N-hydroxysuccinimide (NHS), and ethanol. A detailed description of the scaffold making process is given in the Supplementary Materials.

3.2 Results and Discussion

Endpoints of demineralization (sample translucency) were different for every chemical treatment. The transparency method was used since it was shown to give similar results as the x-ray method, which is considered to be the most accurate method for endpoint determination [126]. For the strong acid solutions, which include HCl/EDTA mixture and HCl, the endpoints

were reached at approximately three and seven hours, respectively. CH_2O_2 became transparent after approximately two days of treatment. The EDTA-treated specimens reached the endpoint after 5-7 days. Selection of endpoint determination methods is key to the preservation of intact collagen because collagen begins to degrade in acidic solutions once mineral is completely reacted [127]. For the weight loss method, demineralization is complete when weight loss stops. Failure to stop the HCl/EDTA mixture after sample transparency was reached resulted in shrunken samples and possibly degraded collagen (Figure 3.1). Samples shown in Figure 3.1 have undergone critical point drying and are therefore no longer transparent. The EDTA-treated samples did not become transparent during demineralization, so the weight loss method was used.

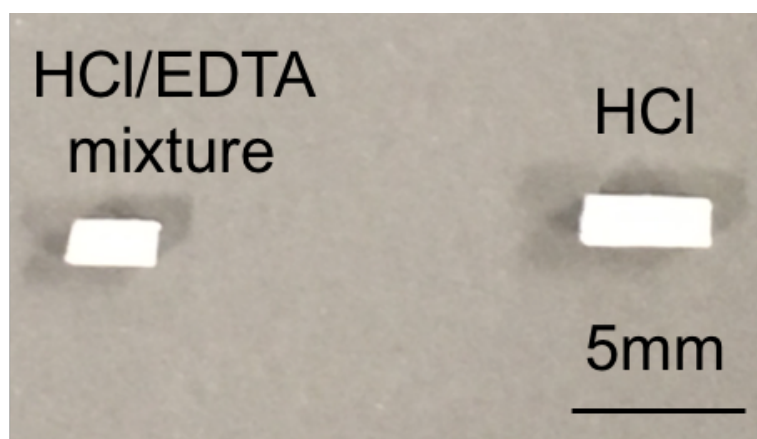


Figure 3.1. Hydrochloric acid/ ethylene-diamine tetraacetic acid (HCl/EDTA) mixture treated sample that is over demineralized and shrunken compared to HCl treated samples.

3.2.1 Raman spectroscopy

Functional groups and their corresponding wavelengths have been published for collagen and hydroxyapatite [58, 59]. As shown in Figure 3.2a, most of the mineral bands of $\nu_1\text{PO}_4^{3-}$ ($\sim 959\text{ cm}^{-1}$), $\nu_2\text{PO}_4^{3-}$ ($\sim 430\text{ cm}^{-1}$), and $\nu_4\text{PO}_4^{3-}$ ($609\text{ cm}^{-1} - 668\text{ cm}^{-1}$) are eliminated by all chemical treatments, except the overlapping bands of $\nu_3\text{PO}_4^{3-}$ ($\sim 1035\text{ cm}^{-1}$ and $\sim 1076\text{ cm}^{-1}$) and $\nu_1\text{CO}_3^{2-}$

($\sim 1070\text{ cm}^{-1}$). The remaining signals detected within that overlapping range are possibly proline $\nu(\text{C-C})$ component (a type of collagen-polymer chain with carbon backbone) [59], which were not removed by demineralization agents. The EDTA treatment has the highest intensity for $\nu_3\text{PO}_4^{3-}$ and $\nu_1\text{CO}_3^{2-}$. There are some weak signals detected near the shoulder of the $\nu_1\text{PO}_4^{3-}$ band at 940 cm^{-1} where the HCl/EDTA mixture treatment has the smallest intensity (Figure 3.2b). The collagen bands of proline ($\sim 853\text{ cm}^{-1}$), hydroxyproline ($\sim 872\text{ cm}^{-1}$), amide I (1660 cm^{-1} , 1690 cm^{-1}), amide III ($1242 - 1340\text{ cm}^{-1}$), and CH_2 ($\sim 1446\text{ cm}^{-1}$) are mostly preserved compared to the untreated samples. In contrast to the mineral trend, the HCl/EDTA mixture treatment leaves the least amount of collagen compared with the other treatments. The intensities of the bands in the HCl and CH_2O_2 treated sample signals are between the EDTA and HCl/EDTA mixture treatments. The hydroxyproline collagen band is most affected by demineralization, as the peak intensity is largely reduced. A previous study using a lower HCl concentration and a longer treating time than the conditions in this paper retained the hydroxyproline band [128]. However, other collagen bands were not investigated. Demineralization conditions should be further studied to optimize mineral elimination and collagen retention.

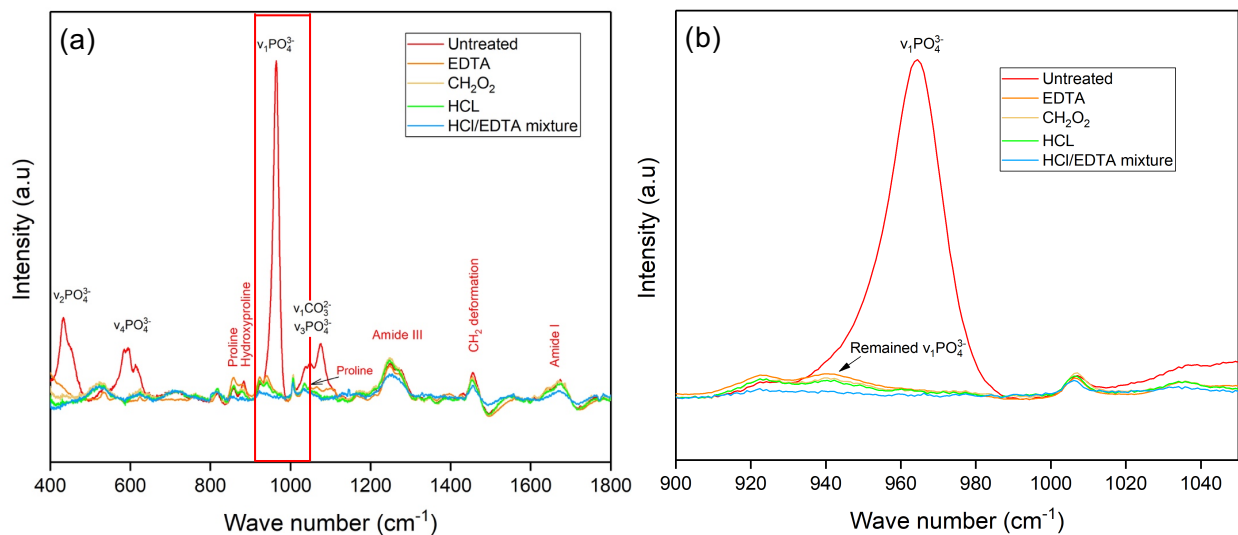


Figure 3.2. (a) Representative Raman spectra indicate mineral and collagen bands for the control bone (Untreated), and for ethylene-diamine tetraacetic acid (EDTA), formic acid (CH₂O₂), hydrochloric acid (HCl) and the HCl/EDTA mixture. (b) Outlined area in (a) with a solid border is shown with the primary phosphate band.

The mineral-to-matrix ratio, mineral crystallinity, and collagen quality are determined for the four types of treated samples ($p > 0.05$) and control samples ($p < 0.05$). Figure 3.3a, b shows that from the CH₂O₂ treatment, the mineral-to-matrix ratio and mineral crystallinity are smallest, and the collagen is best preserved (Figure 3.3c). The low crystallinity indicates that the hydroxyapatite changes to a more disordered structure. The HCl/EDTA mixture treated samples contain the smallest amounts of $\nu_1\text{PO}_4^{3-}$ mineral-to-matrix ratio. The main chemicals in HCl/EDTA solution are HCl and a small amount of EDTA (~0.1%), and the high concentration of HCl resulted in a faster treatment but had a strong effect on the remaining collagen. This led to a smaller amount of mineral and a short treatment time, which was found in a previous study [100]. However, the present results show more changes in the collagen structure from the HCl/EDTA mixture treatment compared to the EDTA treatment, which is not in agreement with this previous study. The different result may be due to uncertainties in determining the endpoint, and the precision of qualitative (histological analysis with H&E staining [100]) and quantitative

analysis (Raman analytical study). Also, the samples treated with chemicals may not be demineralized homogeneously. The position under Raman scans can lead to differences. From our results, the collagen components are less affected by the CH_2O_2 , HCl and EDTA treatments. Among these, the CH_2O_2 and HCl preserve the most collagen. Although the trends between the two procedures are not apparent from the figure, it provides an analytical study using different demineralization agents. To further compare the Raman results, more studies could focus on the control of the concentration of demineralization agents and the reaction endpoint.

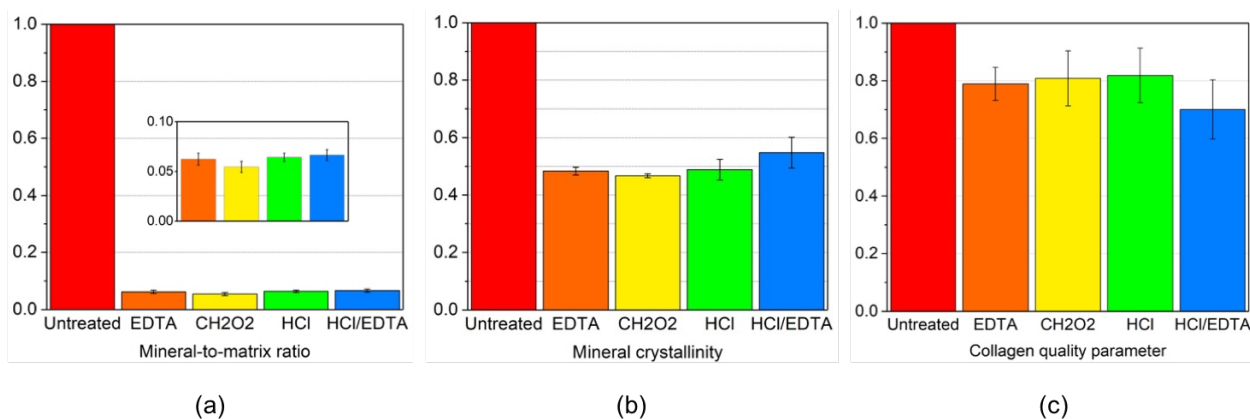


Figure 3.3. Raman spectroscopy analytical study of mineral and collagen content for control bone, and for ethylene-diamine tetraacetic acid (EDTA), formic acid (CH_2O_2), hydrochloric acid (HCl) and the HCl/EDTA mixture treated bone. **(a)** The inset is an enlarged plot of the mineral-to-matrix ratio. Mineral-to-matrix ratio is determined by the intensity ratio of $\nu_1\text{PO}_4^{3-}$ to amide I bands, **(b)** the mineral crystallinity is defined as $1/\text{FWHM}$ of band $\nu_1\text{PO}_4^{3-}$ and **(c)** the collagen quality is the area ratio of $1660/1690\text{ cm}^{-1}$ under amide III band. The three parameters are normalized from 0 to 1 with respect to untreated bone.

Considering the treatment efficiency, HCl only takes seven hours to achieve the similar effect as CH_2O_2 , which took two days. Acids such as HCl, CH_2O_2 and HCl/EDTA mixture (mostly composed of HCl) dissolve the minerals from the low pH. On the other hand, EDTA removes minerals by binding to calcium ions, resulting in the slowly reduced mineral crystal size,

which is a diffusion related process [100]. From this perspective, HCl can be considered the best for treatment speed. A summary of the demineralization efficiency is shown in Table 3.2.

Table 3.2. Effectiveness summary for EDTA (ethylene-diamine tetraacetic acid), formic acid (CH_2O_2), hydrochloric acid (HCl), and HCl/EDTA mixture as determined from Raman spectroscopy.

Treatments	Effectiveness comments
EDTA	Similar ability as HCl to remove minerals and preserve collagen structure; long treating time.
CH_2O_2	Best agent to eliminate most of the minerals and preserve collagen integrity; medium treating time.
HCl	Collagen preservation is as good as for CH_2O_2 . The ability to remove mineral composition is relatively weaker compared to CH_2O_2 ; fast treating time.
HCl/EDTA mixture	Remove largest amount of minerals; collagen integrity is worse than EDTA and HCl; fast treating time.

3.2.2 Fourier-Transform Infrared Spectroscopy

Figure 3.4 shows the FTIR absorption bands of untreated and treated bones. The bands near 560 cm^{-1} and 600 cm^{-1} , 960 cm^{-1} , and 1012 cm^{-1} represent a phosphate functional group (PO_4^{3-}) with different vibration modes. The bands around 870 cm^{-1} and 1410 cm^{-1} are from carbonate functional group (CO_3^{2-}). More band assignments are listed in Table 3.3. The PO_4^{3-} and the CO_3^{2-} groups are found in untreated bone but disappear in treated bone. Under the $\nu_3\text{PO}_4^{3-}$ band, residual peaks between 1000 cm^{-1} - 1100 cm^{-1} are observed in treated samples. The remaining peaks under the band $\nu_3\text{CO}_3^{2-}$ near 1410 cm^{-1} are the CH_2 wag and CH_2 bend, which are collagen markers [109]. The existence of collagen composition has good agreement with the remained signal under $\nu_3\text{PO}_4^{3-}$ ($\sim 1035\text{ cm}^{-1}$ and $\sim 1076\text{ cm}^{-1}$) and $\nu_1\text{CO}_3^{2-}$ ($\sim 1070\text{ cm}^{-1}$) overlapping bands in the Raman spectra.

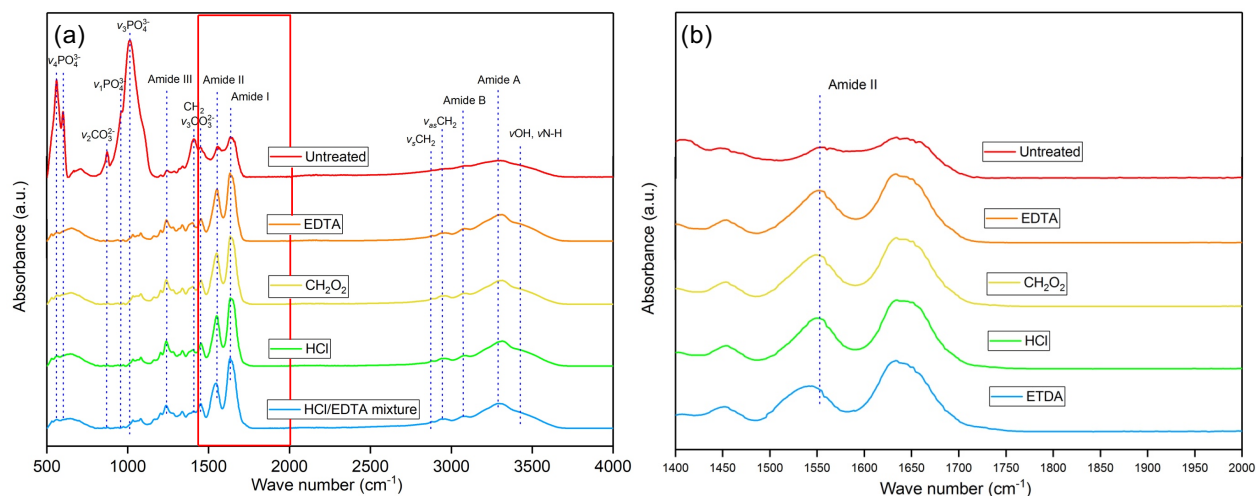


Figure 3.4. (a) Fourier-transform infrared spectra for control bone (Untreated), and for ethylenediamine tetraacetic acid (EDTA), formic acid (CH_2O_2), hydrochloric acid (HCl) and the HCl/EDTA mixture treated bone. (b) Magnified spectra from boxed region in (a) showing the shift in the amide II band.

Table 3.3. Fourier-transform infrared spectroscopy absorption bands for bone and their functional groups.

Wave Number (cm^{-1})	Assignments	Reference
560, 600	$\nu_4\text{PO}_4^{3-}$	[109, 129]
870	$\nu_2\text{CO}_3^{2-}$	[109, 130]
960	$\nu_1\text{PO}_4^{3-}$	[131, 132]
1012	$\nu_3\text{PO}_4^{3-}$	[109]
1240	Amide III	[133, 134]
1410	$\nu_3\text{CO}_3^{2-}$	[109, 129, 135]
1555	Amide II	[136, 137]
1634	Amide I	[109, 136]
2850	CH_2 symmetric stretch	[109, 129]
2930	CH_2 antisymmetric stretch	[109, 129]
3070	Amide B	[138]
3278	Amide A	[109, 130]
3407, 3420	νOH , νNH	[129]

As shown in Figure 3.4a, the collagen markers of amide I, II, III, amide A, B, and symmetric and antisymmetric CH_2 bands are preserved after demineralization. The CH_2 symmetric (2850 cm^{-1}) and antisymmetric stretch bands (2930 cm^{-1}) have an increased intensity for all treatments, which indicates the change in protein secondary structure [129]. The protein

secondary structure is a three-dimensional form that consists of repeated hydrogen-bonding with helical and ladder-like patterns [139]. It is found that the positions of amide II bands are shifted from 1555 cm^{-1} to a lower wavenumber 1540 cm^{-1} in the HCl/EDTA treated bone (Figure 3.4b). This shift in the amide II band can be attributed to the changes in the secondary structure of collagen from an α -helix to β -sheet formation [140, 141]. The decreasing shift from 1546 cm^{-1} by around 10 cm^{-1} of amide II band was observed in a previous study for EDTA treated samples [129]. The EDTA, CH_2O_2 , and HCl treated samples in this paper only changed by around 5 cm^{-1} , which is much smaller than the shift in HCl/EDTA treated samples. The HCl/EDTA mixture results in the most significant change of collagen is in agreement with the Raman analysis. Amide A and amide B bands were found to have increased intensity after all demineralization. This change leads to more vibrational motion for the protein due to the broken hydrogen bonds between the collagen and the mineral [129].

Both FTIR and Raman spectroscopies are used in this study to find different bone compositions. The indication of collagen secondary structure change from the observation of amide II, and CH_2 symmetric and antisymmetric stretches are seen in the FTIR spectra but not in the Raman spectra. Also, in the Raman spectroscopy, the amide A, B bands are not visible as they are in the FTIR spectra. In addition, it is difficult to identify the overlapping bands of $\nu_3\text{PO}_4^{3-}$ and $\nu_1\text{CO}_3^{2-}$ in Raman, while it is straightforward in FTIR as $\nu_3\text{PO}_4^{3-}$ and $\nu_1\text{CO}_3^{2-}$ bands are independent and have strong signals. Meanwhile, Raman spectra supplements several mineral and collagen bands such as the $\nu_2\text{PO}_4^{3-}$ band, which is outside of the viewable range in FTIR, and the proline and hydroxyproline bands, which not easily detectable in FTIR. Most importantly, the Raman can quantitatively measure the change in the bone composition after demineralization.

3.2.3 Thermogravimetric Analysis

Figure 3.5 shows that EDTA and HCl treatments were most effective at removing mineral, while CH_2O_2 and HCl/EDTA treatments left ~10 wt.%. This result is at odds with the Raman results, which show that the CH_2O_2 treatment removed the mineral while preserving collagen components. The discrepancy between the Raman and TGA results may be attributed to the sample size - Raman spectroscopy is a surface measurement while TGA tests the whole sample. The residual mineral in the samples indicates that the treatment endpoints are difficult to determine using the methods employed in this paper. In particular, The HCl/EDTA mixture was difficult to gauge due to its high HCl concentration, and as a result, there is a delicate balance between the complete demineralization and collagen degradation from over-treating the samples.

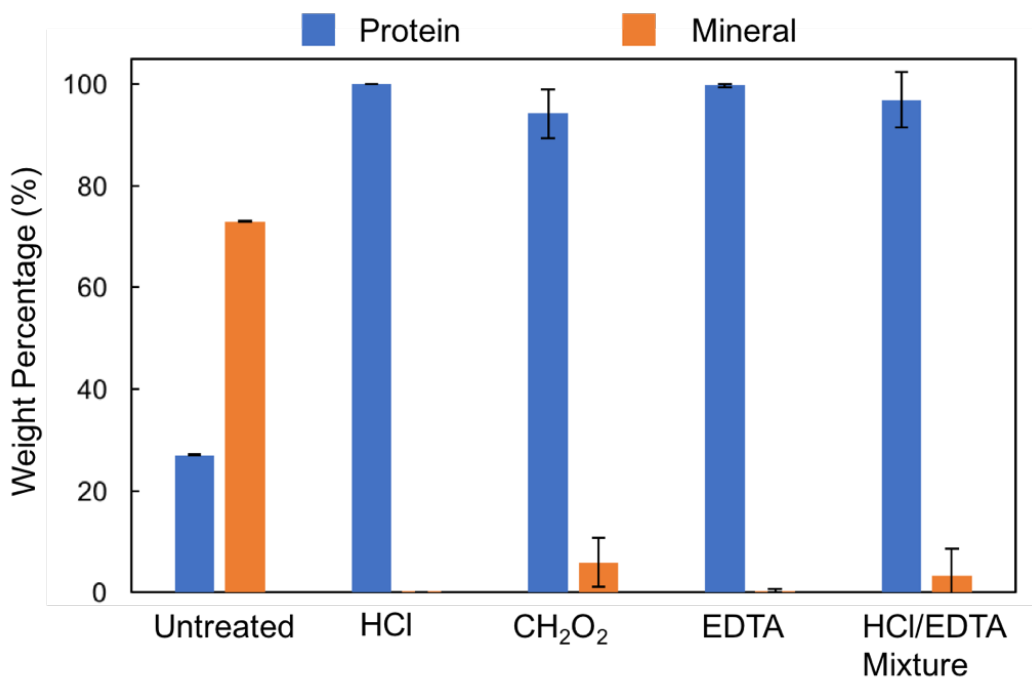


Figure 3.5. Thermogravimetric analysis results after heating to 800°C: weight percentage of mineral and protein once water is removed after each demineralization treatment.

3.2.4 Scanning Electron Microscopy

In untreated bone (Figure 3.6a) the main distinguishable features are mineral particles. After demineralization, aligned collagen fibrils can be seen in all samples where collagen fibrils are outlined with dotted lines and the characteristic *d*-spacing of collagen is indicated by arrows. In the EDTA (Figure 3.6b), HCl (Figure 3.6c) and HCl/EDTA (Figure 3.6d) treated specimens, the collagen network in bone is visible, and fibrils are aligned. Samples treated with CH₂O₂ have regions where aligned collagen is visible but more difficult to see than in other samples (Figure 3.6e) and mineralized regions where the collagen structure is not visible (Figure 3.6f). This demonstrates that CH₂O₂ treated samples are not entirely demineralized. EDS results (Table 3.4) showed that for all samples excluding the CH₂O₂ treated samples, the at.% and wt.% of Ca were zero. This corroborates TGA results that EDTA, HCl, and HCl/EDTA are more effective methods for demineralization than CH₂O₂. The mismatch between wt. % calculated from EDS and TGA is likely due EDS being a surface measurement, while TGA measures the mass throughout the whole sample. Therefore, TGA results are likely more reliable than the EDS measurements.

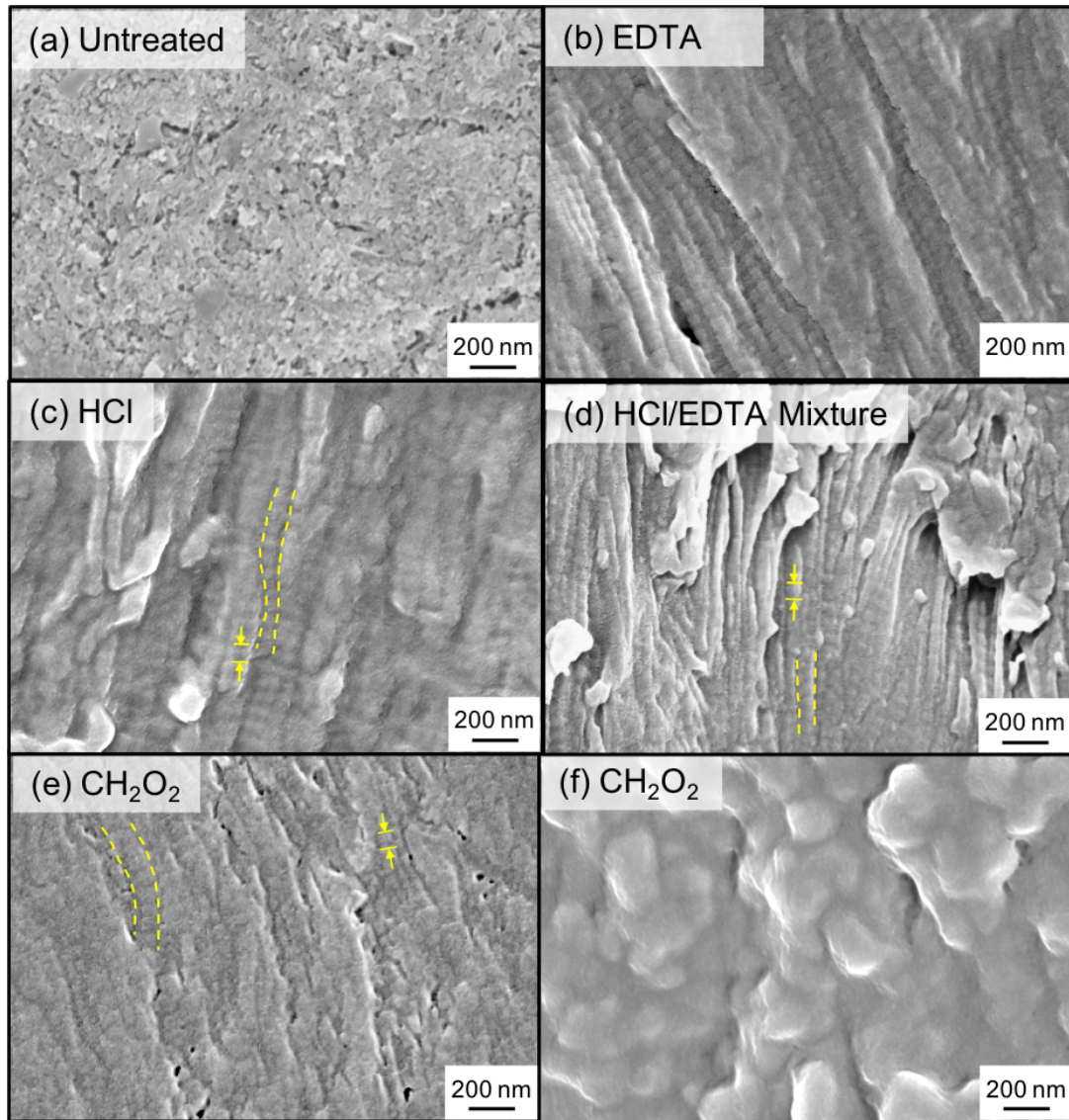


Figure 3.6. Scanning electron microscopy images of (a) untreated bone and demineralized bone using (b) ethylene-diamine tetraacetic acid (EDTA), (c) hydrochloric acid (HCl), (d) HCl/EDTA mixture, and (e,f) formic acid (CH_2O_2). Visible fibrils are outlined in yellow, dotted lines and *d*-spacing is indicated by arrows.

3.2.5 Biomaterial Scaffold Made from Demineralized Bone

In this section, we explored one possible application of demineralized bone. More specifically, a collagen freeze cast scaffold was successfully made with demineralized porcine femur bone using HCl as the demineralizing agent and the end result can be seen in Figure 3.7a. Figure 3.7b shows the transverse cross-section of the collagen scaffold with interconnected micro-porosity. Figure 3.7c shows that collagen banding is present at high magnifications. Due to the crosslinking, which is necessary to keep the scaffold from collapsing when hydrated, there are likely some chemical and structural differences from natural collagen. However, with this method, it is now possible to shape DBM into a porous structure that cells can grow into. Future work should be done to investigate the bioactivity of such a scaffold. Successful cell growth, indicating biocompatibility, has already been shown for a commercial bovine collagen [118].

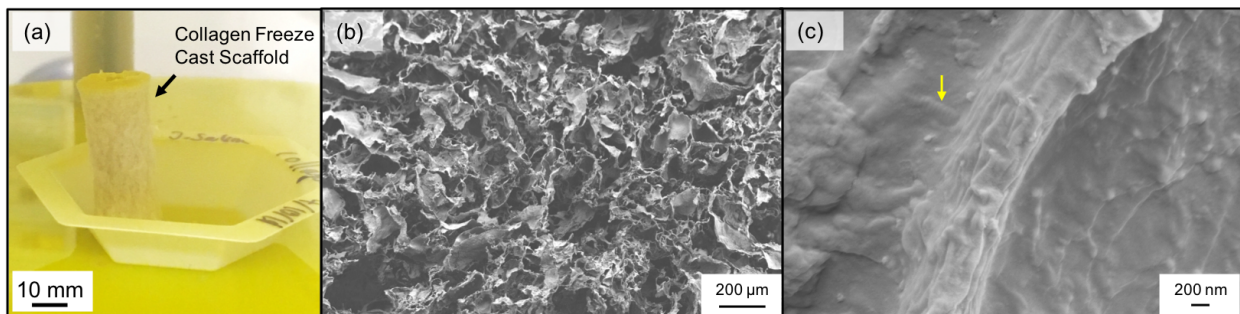


Figure 3.7. (a) An image of the freeze cast collagen scaffold. Scanning electron microscopy images of (b) the transverse cross-section of the freeze cast collagen scaffold and (c) magnified image of collagen scaffold where visible collagen fibrils can be seen indicated by the yellow arrow.

3.3 Conclusions

Four demineralization agents: ethylene-diamine tetraacetic acid (EDTA), hydrochloric acid (HCl), formic acid (CH_2O_2), and EDTA (HCL/EDTA mixture) were used to isolate collagen from six-month-old porcine femurs. The efficacy of mineral removal and the preservation of collagen structure were compared by qualitative and quantitative methods: Raman spectroscopy,

Fourier transform infrared (FTIR) spectroscopy, scanning electron microscopy (SEM) and thermogravimetric analysis (TGA).

- From Raman spectroscopy, CH_2O_2 was found to have the best capability to remove minerals (by 95%)’ and the collagen integrity was best preserved.
 - EDTA and HCl had similar effects on removing minerals and preserving the collagen structure. However, the EDTA treatment was more time-consuming.
 - Although HCl/EDTA mixture was a faster process and removed the largest amount of minerals, it also altered the collagen structure more than the other agents.
- FTIR revealed that all four treatments affected the secondary structure of collagen from the observation of increased amide A and B bands. Among all treatments, the HCl/EDTA solution affected the secondary collagen structure most as documented by the shifted amide II bands. Phosphate bands were mainly removed except for a small amount of $\nu_3\text{PO}_4^{3-}$.
- TGA showed that HCl and EDTA treatments were best at removing mineral, which is not in agreement with the Raman analysis. This observation is attributed to the difference between bulk measurement (TGA) and surface measurement (Raman).
- SEM showed aligned collagen fibrils in all demineralized samples. In the CH_2O_2 treated specimen residual mineral was observed in certain areas of the sample visually and from EDS elemental analysis.
- A porous scaffold made from demineralized bone tissue was prepared from the HCl demineralized bone to illustrate an application of this research. Such scaffolds can be used in regenerative medicine to repair damaged tissues.

The findings from the above experiments revealed that mineral elimination and collagen preservation highly depends on the demineralization agents and the characterization methods. Determination of the endpoint of demineralization can be better controlled with future experiments, as it is critical to the process. Overall, this study provides new insights into the efficiency of different demineralization methods for bone. Such knowledge is of high interest to scientific and tissue engineering communities.

Chapter 3, in part, is a reprint of the material as it appears in “Demineralization of Cortical Bone using Several Protocols and Synthesis of a Collagen Scaffold,” which has been submitted for publication. The dissertation author was one of the primary investigators and authors on this paper. This paper was co-authored by Siyuan Pang, Amesha Green, Justin Salim, Joanna McKittrick, and Iwona Jasiuk.

4 Size and Scale Effects on Mechanical Properties of Additively Manufactured Two-phase Composites with Continuous or Discontinuous Phases

4.1 Introduction and Background

Recently, additive manufacturing (AM), also called 3D printing, has become a new tool for studying the mechanical properties of materials with different microstructures and architectures. In particular, 3D printing has been used for fabricating bioinspired materials and structures. For example, the shape of the seahorse tail and why it has a square cross-section was explored by comparing 3D printed tails with a square or round cross-sections [20]. Square tails were shown to increase resilience of the tail and impact resistance to crushing forces when compared to round tails. 3D printing was also employed to adapt the mouthpiece of the sea urchin for use as a sediment sampler [142]. In composite microstructure studies, nacre and bone have been important sources of bioinspiration. Fracture toughness [143, 144], impact resistance [145], and energy dissipation [146] of nacre and bone inspired microstructures have been tested with AM. A bioinspired design incorporating two levels of hierarchy of nacre showed that impact resistance improved dramatically over only having one level of nacre structure [147]. The significance of suture structures and their geometries in bioinspired materials were also tested using AM techniques [148, 149]. In their recent review, Velasco-Hogan, et al. [18] provide a framework for using additive manufacturing for bioinspiration.

Aside from the bioinspired materials, AM has also been a vehicle for evaluating the effect of composite architectures on mechanical properties of materials containing phases with disparate stiffnesses [150]. Cho, et al. [151] investigated the effects of geometric arrangements by changing the connectivity of a soft and stiff phase in a composite. Bi-continuous, also called

interpenetrating phases, were found to be critical in improving mechanical properties of composites and controlling their deformation behavior. Mineral bridges, or a continuous stiff phase, have also been shown to play an important role in maintaining stiffness and improving toughness in a nacre-inspired 3D printed composite [152].

In particular, multi-material additive manufacturing has been useful for studying architectures of composites and structures given the flexibility of designs and production using this method. Printers can even blend different polymer to achieve more fine-tuned material properties [151]. However, given that the technology is still in development, there are some shortcomings and artifacts present in the resulting prints. For example, Yap, et al. [153] found that dimensional accuracy was dependent on printing orientation, position on the printing surface, and surface finish of the print (glossy or matte). Dimensions were found to be most accurate in the height dimension of matte finish prints. Material properties of 3D printed materials are dependent on print conditions, AM technique used, dimensions of the sample, and other factors [154]. Bass, et al. [155] showed that a print orientation has a larger effect on material anisotropy of soft materials (Tango) rather than stiff materials (Vero) printed with the Objet 350 printer. The effect of aging on mechanical tensile properties was also explored, and mechanical properties of both materials showed no change until the sixth week, after which tensile strength and elastic modulus increases. While the influence of some print factors on mechanical properties has been explored, most studies focus on tensile properties and single material properties. Moreover, there is a dearth in literature on size and scale effects in 3D printed composites.

In this paper, we investigate the influence of the size of the unit cell and scale on mechanical properties of two-phase composites with different architectures. To clarify our terminology, size effects refer to changes in properties based on the physical sample size of

composites, while scale effects involve varying the number of unit cells within a sample which is also associated with boundary conditions effects. More specifically, boundary conditions will generally influence results when number of unit cells is small, i.e., when there is no representative volume element. Following Hill, representative volume element is defined as a region large enough so size of inclusions is much smaller than the size of the sample and overall material properties do not depend on boundary condition. We consider two cases, one where the size of the sample is fixed but number of unit cell sizes increases and the second involving only one unit cell and changing its size. We conduct this study experimentally by 3D printing three types of composites: a discontinuous composite (DPC), a matrix inclusion composite (MIC) with one continuous phase with cubic inclusions, and an interpenetrating phase composite (IPC) with two continuous phases, following Sabet, et al. [156], and compare results with finite element method (FEM) simulations. Our prior study focused on the mechanical behavior of such composites [17]. It was found that a continuous stiff phase increases elastic modulus and that compressive load is carried mainly by the stiff phase while the soft phase contributes to deformation of these composites. The focus of this study is to vary the size and number of unit cells to understand their effects on mechanical properties 3D printed composite materials and compare these results to those of FEM.

4.2 Materials and Methods

4.2.1 Additive Manufacturing

Cell geometries were created in Solidworks (Dassault Systèmes, Vélizy-Villacoublay, France) and printed using an Objet 350 Connex3 printer (Stratasys, Poway, CA, USA) in Digital Materials Mode, which uses ~ 30 μm layer thickness. Materials used for 3D printing were VeroClear, which represents the stiff phase, and TangoBlackPlus, which is the soft phase.

Properties of the individual materials are summarized in **Table 4.1**. Three types of two-phase periodic composites were printed: a discontinuous phase composite (DPC), a matrix-inclusion composite (MIC), and an interpenetrating phase composite (IPC) (first column of **Figure 4.1**), following [156]. Samples were printed with the “matte” setting to ensure uniform support material coverage as opposed to the glossy setting, which uses support material at the bottom but no support material on other surfaces when printing a cube sample. After printing, support material was removed from samples using a high-pressure waterjet. Specimens were allowed to dry at least overnight before testing.

Table 4.1. Mechanical properties of the stiff and soft polymer materials used for additive manufacturing. TangoBlack+ has no elastic modulus value since it is a nonlinear material. Poisson’s ratio was given by the manufacturer. Values are given as average (s.d.).

Material	Elastic Modulus (MPa)	Compressive Strength (MPa)				Poisson’s Ratio
VeroClear (stiff)	1,220 (40)	67.3 (0.7)				0.41
TangoBlack+ (soft)	-	2.9 (0.2)				0.49


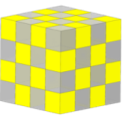
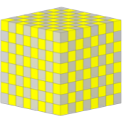
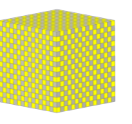


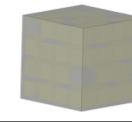
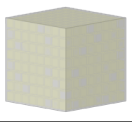
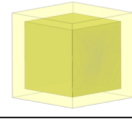
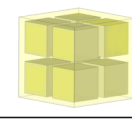
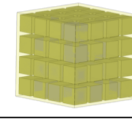
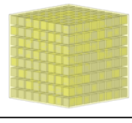
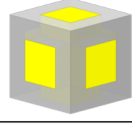
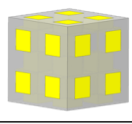
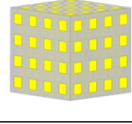
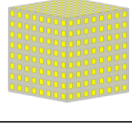
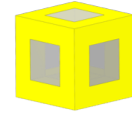
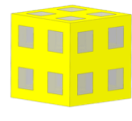
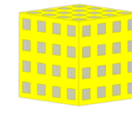
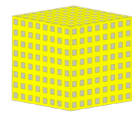
		1x1x1	2x2x2	4x4x4	8x8x8
Discontinuous phase composite	-				
Matrix-inclusion composite	Soft frame				
	Stiff frame				
Interpenetrating composite	Soft frame				
	Stiff frame				

Figure 4.1. Types of unit cells and samples with varying numbers of unit cells.

4.2.2 Mechanical Testing and Analysis

Quasi-static compression tests were performed according to ASTM Standard D695 – 15 (citation) at a strain rate of 0.1% per second. Sample geometry was changed from 2:1 to 1:1 length to width ratio compared to the ASTM standard since some samples were prone to buckling and slipping out of the mechanical testing machine. Samples were tested so that the printing direction, which dictates lamellar alignment, was perpendicular to the axis of compression. This was done because samples tend to split when compressed parallel to the direction of printing due to the innate microstructural features from layer-by-layer printing. Testing order of specimens was also randomized using a random number generator. A linear fit was applied to determine elastic modulus of samples. Average curves were plotted by interpolating stress-strain curves at evenly spaced intervals.

Two sets of compression experiments were conducted: (1) one with the same sized samples ($12.7 \times 12.7 \times 12.7 \text{ mm}^3$) with different numbers of unit cells including the single unit cell (1x1x1), 2x2x2, 4x4x4, and 8x8x8 shown in Figure 4.1, and (2) individual unit cells with edge lengths of 12.7, 6.35, 3.18, and 1.58 mm that correspond to the sizes of single unit cells in the samples described in set (1). The first set of tests explores the effects of scale under mixed boundary conditions and approximates periodic boundary conditions by increasing the number of unit cells. The second set of tests explores the mechanical properties of unit cells of a smaller size. The minimum feature size was $\sim 0.21 \text{ mm}$, which is almost an order of magnitude larger than the resolution of the 3D printer $\sim 0.030 \text{ mm}$. Six samples were printed out for each sample type in experimental set (1) and three samples were printed for each sample type in experimental set (2) after experimental set (1) showed consistent mechanical properties.

To perform a digital image correlation (DIC) on the samples, compression tests were recorded using a Coolpix L830 (Nikon Inc, Tokyo, Japan) at 720p and 30 fps. Videos were cropped and processed using a Matlab script so that every 25th frame was converted to a TIFF image. Ncorr [157] was used for DIC to look at planar (2D) displacement and strain maps. First, a reference image was loaded, and then a region of interest was selected as the sample surface facing the camera. DIC parameters such as subset radius and spacing were changed according to the sample, but had values of approximately 25 and 5, respectively. Step analysis with seed propagation and auto propagation of seeds was enabled.

4.2.3 Finite Element Modeling

The model composites were also modeled using a finite element (FE) software Abaqus (v. 6.14). The stiff and soft polymers were modeled as elastic-plastic and non-linear hyperplastic materials, respectively. Young's modulus (E) of 1.22 GPa, and Poisson's ratio of 0.41 (provided by the manufacturer) were used for the stiff phase with a maximum stress of 67.3 MPa after which a perfectly plastic behavior was assumed. The soft phase was modeled using Yeoh formulations [158]. The Yeoh model, also called the third-order reduced polynomial form, is used to describe isotropic incompressible rubber-like materials. In this model, the strain energy function (W) is described by Eq. 1:

$$W = \sum_{i=1}^3 C_{i0}(I_1 - 3)^i \quad (1)$$

where C_{i0} are material parameters and I_1 is the first strain invariant. Yeoh model depends only on the first strain invariant as given in Eq. 1. There are two options for inputting properties of the Yeoh model in Abaqus software. The first option is to enter coefficients of the model while the second option is to directly input stress-strain results so the software calculates the coefficients for the model. Poisson's ratio of 0.495 was used for the soft polymer as provided by the

manufacturer. In this study, the experimental test results on the soft polymer were directly entered into Abaqus. The interfaces between stiff and soft phases were assumed to be perfectly bonded. The models were also simulated allowing free slippage/separation at interfaces. In normal direction, hard contacts were set up while frictionless slip was assumed in tangential direction. It was observed that assuming free slippage/separation at interfaces did not significantly affect the overall modulus or maximum obtainable stress. To model the DPC, each cubic block of material (either soft or stiff) was imported separately into Abaqus and then proper constraints (perfect bonding) were applied at the interfaces. Another option is to import all four blocks of each phase as a whole in which case a stiffer response is expected. 10-node quadratic tetrahedron elements (C3D10) were used to mesh the models and a mesh convergence study was done for each geometry to ensure adequate fineness of the mesh. Mixed boundary conditions (MBC) were applied to mimic the experimentally applied boundary conditions. The bottom surface was fixed in all directions, while the four sides were traction free. A displacement equivalent to up to 15% apparent strain was applied on the top surface to compress the models.

4.3 Results and Discussion

It is important to document the variance in 3D printed composites depending on the printing direction. The printed samples had an average density ranging from 1.058 g/cm³ to 1.075 g/cm³ with an average density of 1.070 ± 0.003 g/cm³. The pure material average densities were found to be 1.10 g/cm³ for VeroClear and 1.06 g/cm³ for TangoBlack+. Different dimensions were also measured depending on the direction of printing as observed from other studies [159]. The height of the samples, which is the dimension perpendicular to the printing plane, is shorter than the two dimensions parallel to the printing plane.

4.3.1 Increasing Number of Unit Cells

The first set of samples tested included the three different composite types with four different numbers of unit cells in a given sample while keeping the overall test sample size constant. The effect of this constraint is to test the effects of the size of a unit cell as well as understand mechanical behavior of the composites when changing size of the microstructure, i.e. changing scale. Samples were tested in compression under mixed boundary conditions: side walls were traction free, and the base and top platen had roughness, resulting in zero applied displacement at the base and changing vertical displacement with approximately zero horizontal displacement. Following results of Huet [160], it is expected that periodic boundary conditions are approached by increasing the number of unit cells. During the test, loads were kept within a reasonable range for the load cells available.

Stress-strain curves (Figure 4.2) are separated by composite type and include results from samples with different numbers of unit cells and FE modeling for $1 \times 1 \times 1$ samples with MBC or PBC and a $2 \times 2 \times 2$ sample with MBC. Behaviors of single unit cells are described in Sabet, et al. [156] and average stress-strain curves of unit cells are shown in Appendix C (Figure C.1). Experimentally, as the number of unit cells increases, the DPC (Figure 4.2a) maintains an almost constant elastic modulus, but increases in yield strain and correspondingly, yield strength. The MIC with soft frame unit cell (Figure 4.2b) exhibits a characteristic low stiffness at low strains when the load is being carried by the soft phase, and stiffening as the strain increases due to the load being supported by the stiff phase at higher strains. However, as the number of cells increases, this behavior that is visible in the $1 \times 1 \times 1$ and $2 \times 2 \times 2$ unit cells, disappears for $4 \times 4 \times 4$ and $8 \times 8 \times 8$. This implies a homogenization that is occurring at a larger number of unit cells. It is clear that the characteristic behavior seen in the unit cell is present in the FE modeling results

even with periodic conditions, so it is possible that the homogenization is a result of increased interface effects with smaller unit cells. Finally, for the MIC with stiff frame and IPC geometries (Figure 4.2c, d, and e), the stiffness decreases as number of unit cells increases.

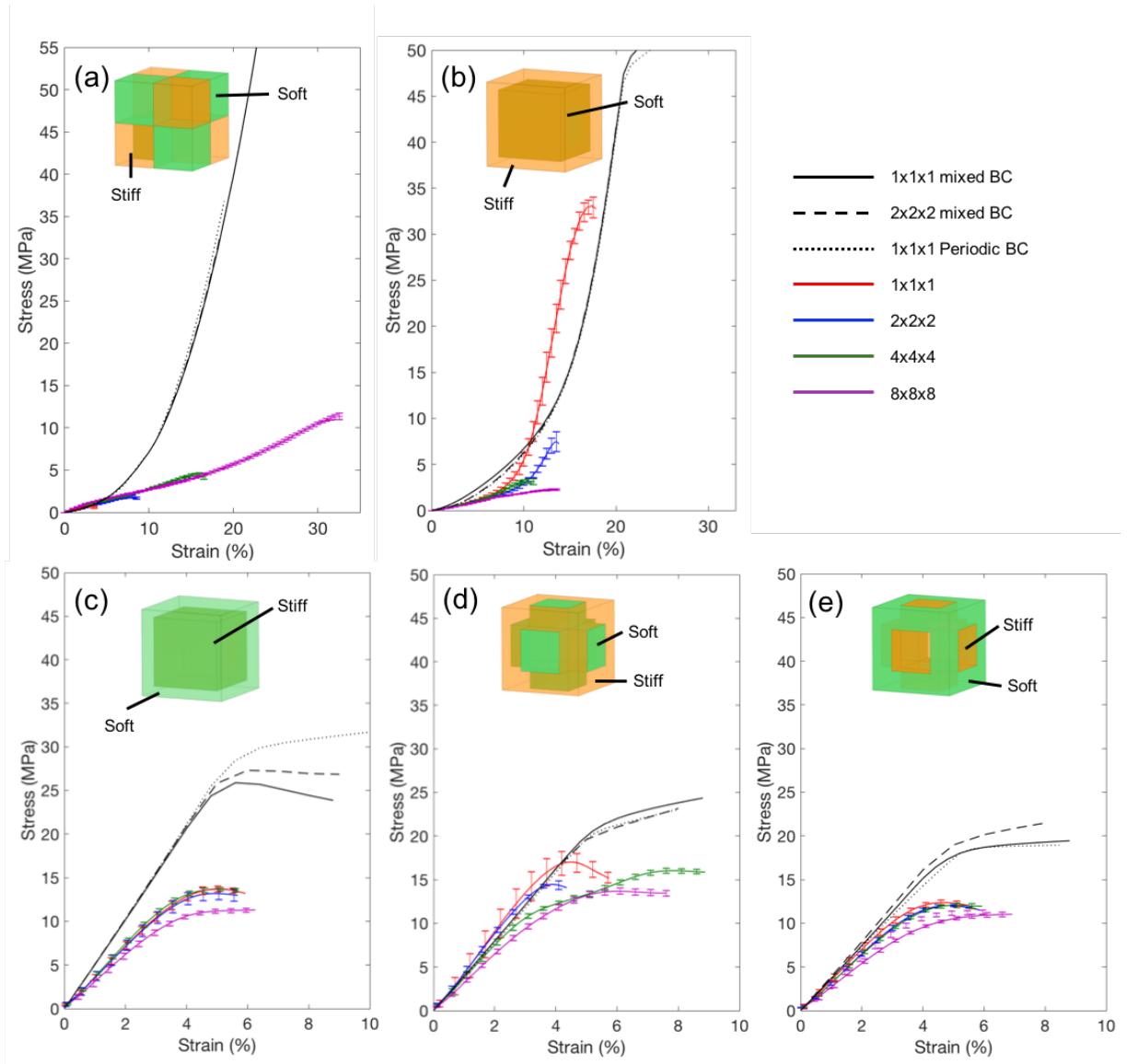


Figure 4.2. Stress-strain curves of 3D printed samples for (a) discontinuous phase composites, (b) matrix-inclusion composite with soft frame, (c) matrix-inclusion composite with stiff frame, (d) interpenetrating composite with soft frame, and (e) interpenetrating composite with stiff frame. Results from finite element modeling of each composite type is also shown.

In the context of cellular solids, which include open and closed-cell foams, scale effects occur when the cell size of the material is in the range of 2-6 mm [161]. These effects manifest from a change the number of cells exposed to certain boundary conditions, and as scale increases, moduli increase in ductile cellular solids materials [161]. In experiments, modulus was found to increase up to a plateau when a $L/d \approx 6$, where L is the specimen size and d is cell size, and strength also increased with increased number of unit cells [162]. This is the opposite of the trend that is observed in our study, where larger scale results in decreased modulus and compressive strength. In agreement with our results are the findings from Alkhader, et al. [163] that show from modeling that increasing the number of repeated units of a cellular solid in the loading direction results in a decrease in compressive strength. It is necessary to point out that our material is a filled composite rather than a porous, cellular solid, which is most often discussed in literature. The difference in manufacturing method of these materials could also be a source of deviation in the reported trends. It is unclear what the effects size effects would be on individual composite phase and it is a topic that warrants further study for 3D printed materials.

In the realm of composites, most studies on scale observe the influence of different sized particles in particle-reinforced composites with stiff inclusions and a soft matrix [164, 165], which are similar to the MIC with soft frame described in this paper. The change in particle size with constant volume loading is analogous to having smaller cell sizes for the same specimen size, which was done in the present study. Fu, et al. [165] show that in particulate-polymer composites with low volume fractions (10-18 vol.%) of the stiff phase, modulus is constant with particle size. In higher volume fractions (30-46 vol.%), elastic modulus shows a slight decrease as particle size is increased, which is not consistent with what is observed in the MIC with soft

frame in our work. In addition, the effects of size and scale have not been studied extensively for composites with periodic structure, especially for IPCs and DPCs.

In almost every geometry, the FE models predict higher strength and are generally consistent with each other regardless of boundary conditions (Table C.1). Meanwhile, yield strain (Figure 4.3b) is similar for all geometries with a continuous stiff phase (MIC with stiff frame and IPCs). FE models also generally predict higher elastic moduli for all of the networks (Figure 4.3c). The exceptions to this rule are the DPC and IPC soft frame composites, which have higher elastic moduli but lower strengths compared to FE results. Values for yield strain, yield stress, and elastic modulus are given in Table C.1 in Supplementary Material for experimental and FE results. Results from FEM are generally consistent regardless of boundary condition or number of unit cells tested. Values for elastic modulus can also be compared to those estimated from the following effective modulus equations based on a constant volume ratio of 0.5 for each phase: Voigt, Reuss, Voigt-Reuss-Hill, and Hashin-Shtrikman models, which are described in the equations shown in Table 4.2. Values in Table 4.2 were calculated with mechanical properties of the component stiff and soft polymers given in Table 4.1. In order for these equations for effective elastic moduli to be used, materials are assumed to be isotropic and linear. In the case of the soft phase TangoBlackPlus, we assume approximate linear and elastic behavior at strains below 10% and a modulus of 1.25 MPa was used, which was measured from mechanical testing. The Voigt and Reuss models overestimate and underestimate the elastic modulus, respectively, though the Voigt model is much closer to the value of the elastic moduli for $1 \times 1 \times 1$ IPC composites and the MIC with stiff frame due to the assumption of constant strain, while the Reuss model assumes a constant stress, making it closer to the behavior of the MIC with a soft frame and stiff inclusions [166]. It is clear from previous work with these geometries

that uniform stress is not present and that the stress is mainly localized in the stiff phase when the stiff phase is continuous [156]. While uniform strain is not a precise assumption either, it is a closer approximation than uniform stress. The Hashin-Shtrikman model has narrower bounds than the rule of mixtures to predict effective elastic modulus and the Voigt-Reuss-Hill model is a quick way to approximate properties since the predictions of the Voigt and Reuss models' values are so different [166]. The Voigt-Reuss-Hill and Hashin-Shtrikman upper bound models more closely match the properties observed in experiments for the MIC stiff frame and IPC elastic moduli.

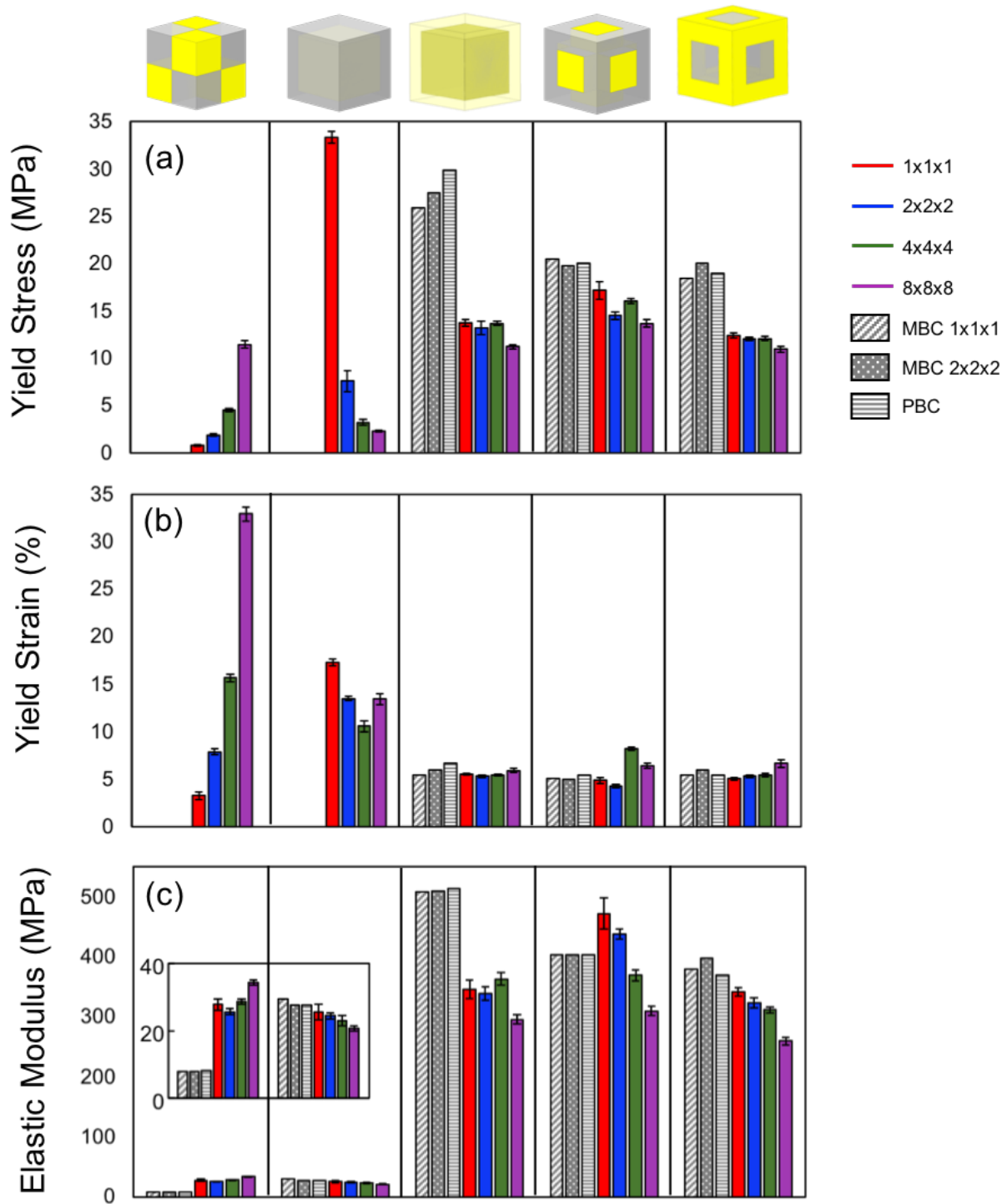


Figure 4.3. (a) Yield stress, (b) yield strain, (c) elastic moduli of composites with increasing number of cells, where gray bars show modeling results and colored bars show experimental results.

Table 4.2. Effective modulus equations and calculated values based on properties of VeroClear and TangoBlackPlus with a volume fraction (ϕ) of 0.5 for each phase. Values are calculated with mechanical properties of the stiff and soft polymers given in Table 1.

Model Type	Equation	Effective Modulus (MPa)
Voigt	$E_{Voigt} = \sum_{m=1}^n \phi_m E_m$	610
Reuss	$E_{Reuss}^{-1} = \sum_{m=1}^n \phi_m E_m^{-1}$	2.5
Voigt-Reuss-Hill	$E_{VRH} = \frac{E_{Voigt} + E_{Reuss}}{2}$	306
Hashin-Shtrikman (upper bound)	$E_{HS^+} = -E_M + \left(\frac{\phi_M}{2E_M} + \frac{\phi_T}{E_T + E_M} \right)^{-1}$	409
Hashin-Shtrikman (lower bound)	$E_{HS^-} = -E_T + \left(\frac{\phi_M}{E_T + E_M} + \frac{\phi_T}{2E_T} \right)^{-1}$	3.74

2D strains were measured using DIC and results for ε_{xy} and ε_{yy} are shown in Figure 4.4. As previously observed in Sabet, et al. [156], the soft phase contributes more to deformation. As the number of unit cells is increased, one can see that for ε_{yy} the strain is mostly in the soft phase and for ε_{xy} , the strain is at the interface between the stiff and soft phase. Samples after compression are shown in Figure 4.5, and deformation of composites are distinctly different depending on geometries. Starting with the DPC, it can be seen that the soft phase undergoes compression while the stiff polymer regions generally stay relatively uncompressed. This leads to eventual debonding between the laterally adjacent stiff and soft units, since the corners between phases cannot stay joined when only the soft phase deforms. This is most visible in the $1 \times 1 \times 1$ and $2 \times 2 \times 2$ samples, and bulging out of the soft phase can be seen and is corroborated by the high shear strain seen in DIC results. As the number of unit cells increases, it appears that the

strain is more distributed throughout the whole sample, leading to larger overall strains as the platen can be seen compressing the sample more for 4x4x4 and 8x8x8 samples.

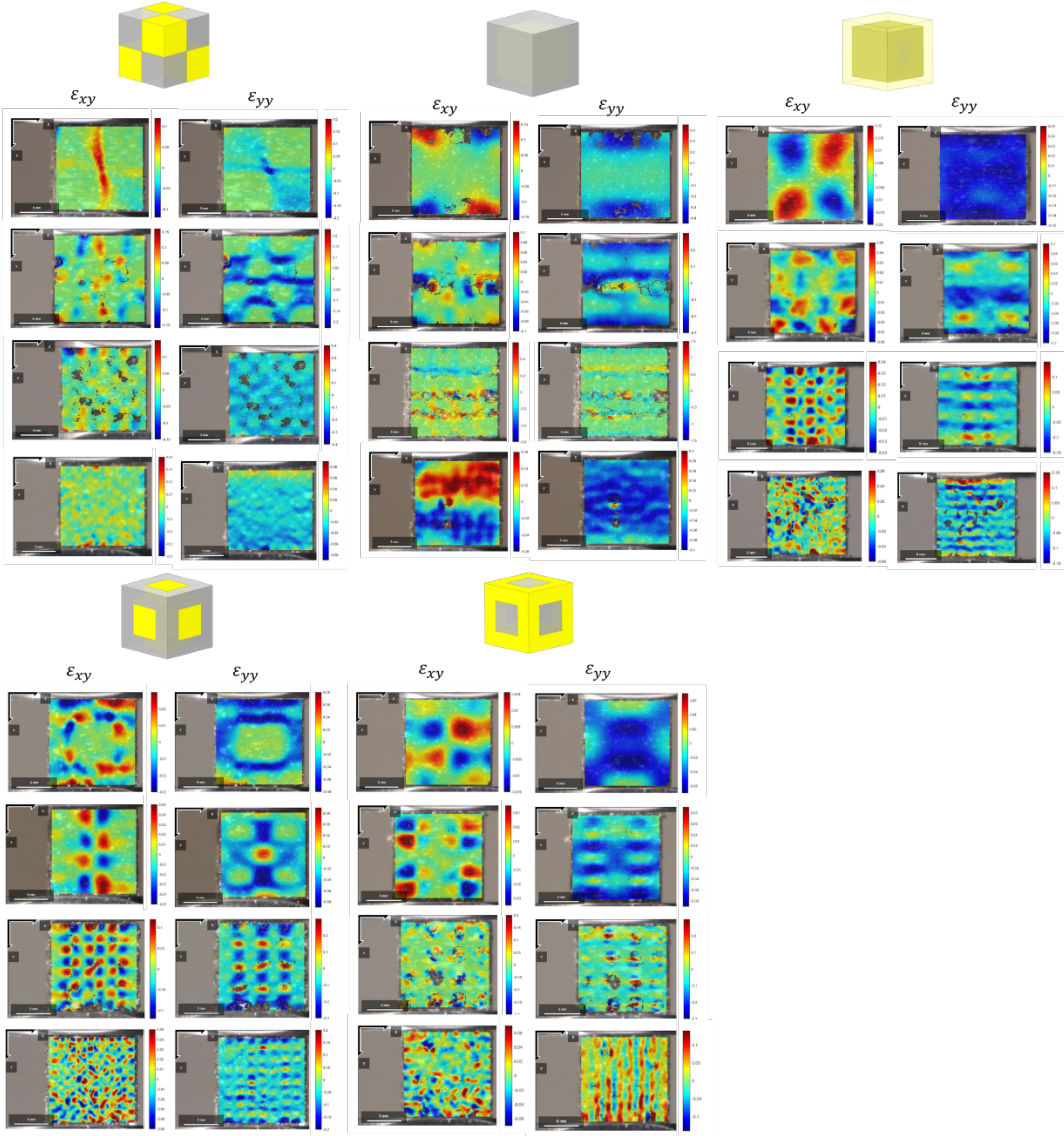


Figure 4.4. Strain maps for ϵ_{xy} and ϵ_{yy} for each composite geometry

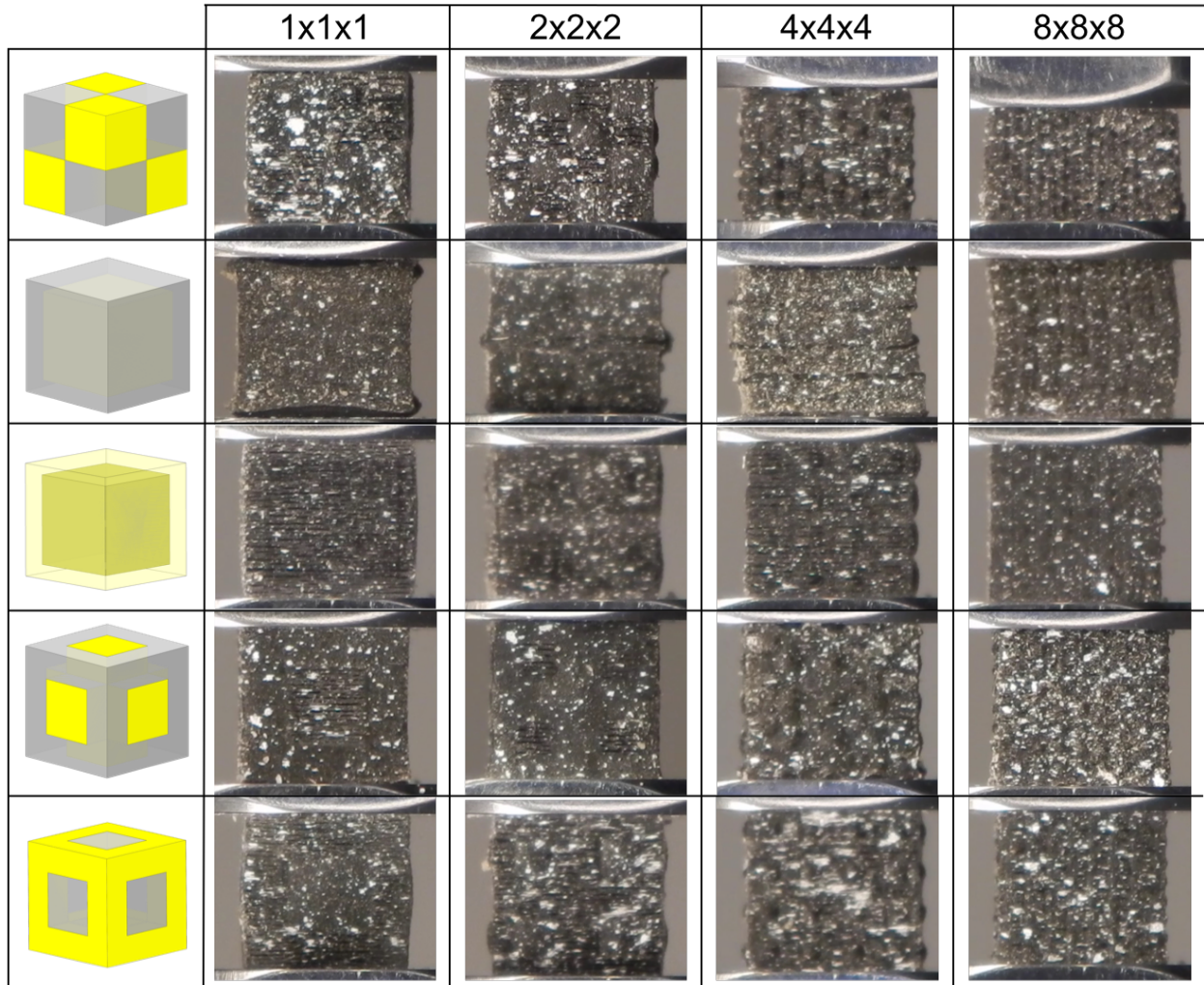


Figure 4.5. Deformation of different composite types with different numbers of unit cells. All samples measure 12.7 mm in side length.

For the MIC with a soft frame, a strain is localized in the soft phase as the number of unit cells increases. The localization develops in regions in between the stiff inclusions and leads to overall material bending during compression, which is visible in the 4x4x4 and 8x8x8 samples. In the DIC results (Figure 4.4), shear strains are localized in the regions between the stiff inclusions for the 2x2x2 and 4x4x4 samples. Additionally, there is overall shear between the top and bottom halves of the 8x8x8 sample as can be seen by the red and blue coloration. Strain localizations have less of an effect on overall material stability when there is a continuous stiff phase. This is seen in the MIC with stiff frame and both IPCs. For the MIC with stiff frame,

bulging can be seen at the lateral walls of the material. As the soft phase deforms, it pushes the thin walls at the edge of the samples outwards. In both IPCs the load is carried by the stiff phase, so the compression of the soft phase and restriction from the stiff phase causes the soft phase to bulge where it can. This translates to bulging of the soft phase side limbs.

While 3D printing has been used extensively to study many composites and their behaviors, the influence of interface properties and thickness have not been studied in depth and are generally assumed to be perfectly bonded. Dimas, et al. [143] made the assumption of perfect bonding after observing that the interface adherence was stronger than the strength of the soft phase; however, this may be due to the small dimensions of the soft phase, which was only 250 μm wide. Their paper mentions earlier that certain topologies were not synthesized well from the printing process due to the small dimensions of the print and that mixing likely occurs at the interface between the different materials in the composite. With the additive manufacturing method used, which is the same as what is used in the current study, mixing of materials at the interface is likely inevitable, and the influence of this mixing is magnified as feature sizes become smaller. As the number of unit cells is increased while keeping the overall sample size the same, the interface surface-area-to-sample-volume ratio increases. These values were calculated for our sample size and are shown in Table 4.3. Based on these results, we can see that for a $12.7 \times 12.7 \times 12.7 \text{ mm}^3$ sample, we expect the stiffness of the DPC to drop the most between the $1 \times 1 \times 1$ and $8 \times 8 \times 8$, since the surface area-to-sample volume ratio increases the most. After that is the MIC, and finally, the IPC. Looking back to Figure 4.3, we notice the exact opposite of this trend, where the DPC stiffness increases slightly with number of unit cells, MICs have a slight decreasing trend, and IPCs decrease in stiffness the most with number of unit cells. It is not very apparent why this would be the case.

Table 4.3. Surface area of the interface between the two phases to volume ratio of the overall sample with dimensions $12.7 \times 12.7 \times 12.7 \text{ mm}^3$. Units are in mm^{-1} .

	1×1×1	2×2×2	4×4×4	8×8×8
Discontinuous Phase Composite	0.24	0.71	1.65	3.55
Matrix-inclusion Composite	0.29	0.59	1.18	2.36
Interpenetrating Composite	0.24	0.47	0.94	1.89

The perfect bonding assumption was not found to be valid through observations of the composite materials during experiments. Debonding can be seen most easily in the DPC 1x1x1 composite at the corner region between the phases, where there is high shear strain. Other composite types did not show as dramatic debonding behavior. However, it is clear that modeling of composites could be improved in the future by measuring the interfacial strength between the two polymers.

4.3.2 Decreasing Size of Unit Cell

The second set of samples involved testing individual unit cells at different sizes. This was done to observe whether unit cell size has an influence on mechanical properties, and if so, what the effects are. This case provides insights on size effects of 3D printed composites. Figure 4.6 shows the average curves for each composite type related to size, and analysis was done for specimens of the component materials (Figure 4.6a-b) and for the composites (Figure 4.6c-g).

Starting with the single phases samples and based on general materials concepts, it is expected that the elastic modulus should remain the same while the strength increases when sample size is decreased. Previous studies using brittle materials, such as ceramics and crystalline polymers, have shown that strength increases because the probability that defects are present in a material decreases as sample size decreases, both in both tension and compression testing [166-168]. This also holds true for polymers in tension [169, 170]. The effect of sample

size has not been studied in depth for additively manufactured composites and is still poorly understood across different printing techniques. The homogeneous stiff and soft materials stress-strain curves are shown in Figure 4.6a, b. The soft material (TangoBlack+) shows an increase in strength and that the nonlinear behavior changes and stiffer behavior is seen as the sample size decreases. This behavior is in line with expectations in terms of higher strength. Conversely, the stiff polymer (VeroClear) does not seem to follow predicted trends in materials as both the elastic modulus and strength decrease as sample size decreases. The change in stiffness may imply that the microstructure of the print at small dimensions is different, resulting in a decreased elastic modulus. Further exploration in the future using scanning electron microscopy should be done to look at microstructure of prints.

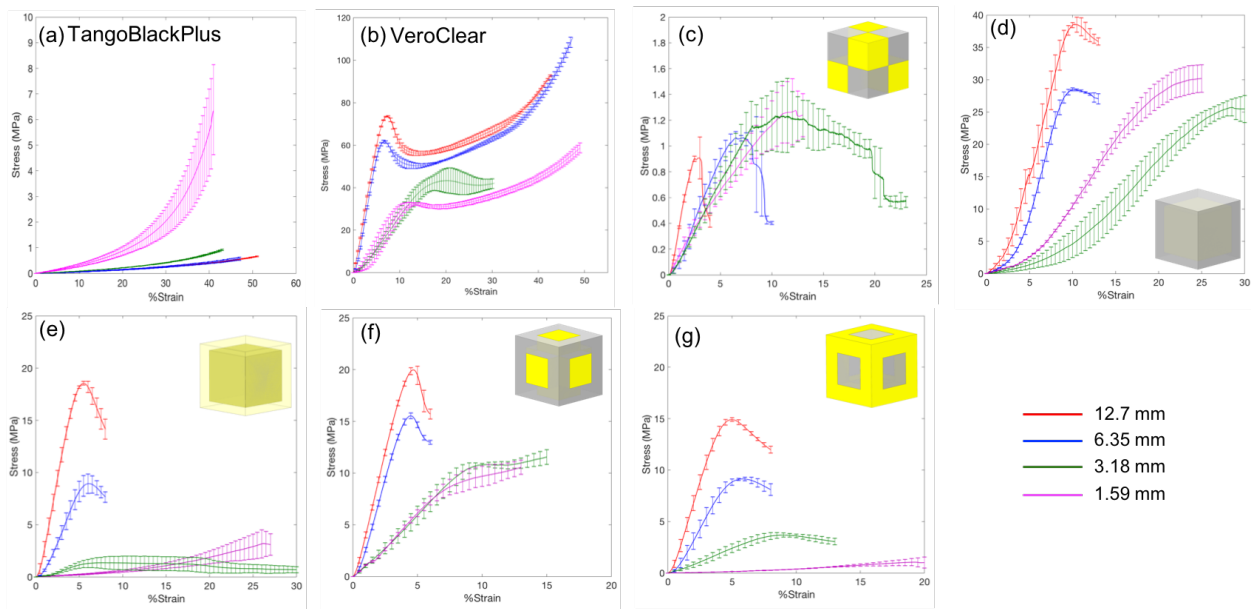


Figure 4.6. Average stress-strain curves for samples with different sizes. Component materials **(a)** soft phase material (TangoBlackPlus) and **(b)** stiff phase material (VeroClear) and composite geometries **(c)** discontinuous composite, **(d)** matrix-inclusion composite with stiff shell, **(e)** matrix-inclusion composite with stiff frame, **(f)** interpenetrating composite with soft frame, and **(g)** interpenetrating composite with stiff frame are shown. Red, blue, green, and magenta curves represent unit cells with side lengths 12.7, 6.35, 3.18, and 1.59 mm, respectively.

For all composites, the elastic moduli of unit cells decrease as sample size decrease, which is unexpected given that elastic modulus should either stay the same or increase with size. This is supported by Cosserat elasticity which predicts that a decrease in sample diameter results in increased sample stiffening [171]. However, softening can occur as sample size decreases due to surface damage effects [172]. This leads us to hypothesize that the softening is primarily due to printing defects at the surface of samples. At small sizes, the surface area to volume ratio decreases. Therefore, there are likely competing factors when traditional materials theory is applied to 3D printed composites.

Strength was found to decrease dramatically with the smaller sample size. This is especially pronounced in the MIC and IPC samples with stiff frames. In Figure 4.6, the elastic modulus drops off dramatically for the aforementioned composite types when transitioning from 3.18 mm edge length to 1.58 mm edge length. As the sample becomes smaller, the thickness of the frame becomes very thin and any printing defects on the surface of the unit cell likely have a large effect. In comparison, the MIC and IPC with a soft frame show lower drop-offs in strength and stiffness. The central column in the IPC with soft frame likely helps maintain strength and stiffness. DPCs show that strength increases when unit cell size decreases, which is a similar result to what is seen in DPC when the number of unit cells is increased.

Comparing results to those described in Chapter 4.3.1, some key observations can be made. The decrease in stiffness and strength is more dramatic for decreasing the sample size of a single unit cell when compared to decreasing unit cell size while keeping sample size the same. Therefore, it is reasonable to think that there are different factors effecting the decrease in mechanical properties in each scenario. Whereas experiment (1) results show lower mechanical

properties due to imperfect boundaries and polymer mixing, experiment (2) seems to largely be affected by imperfections on the surface of prints due.

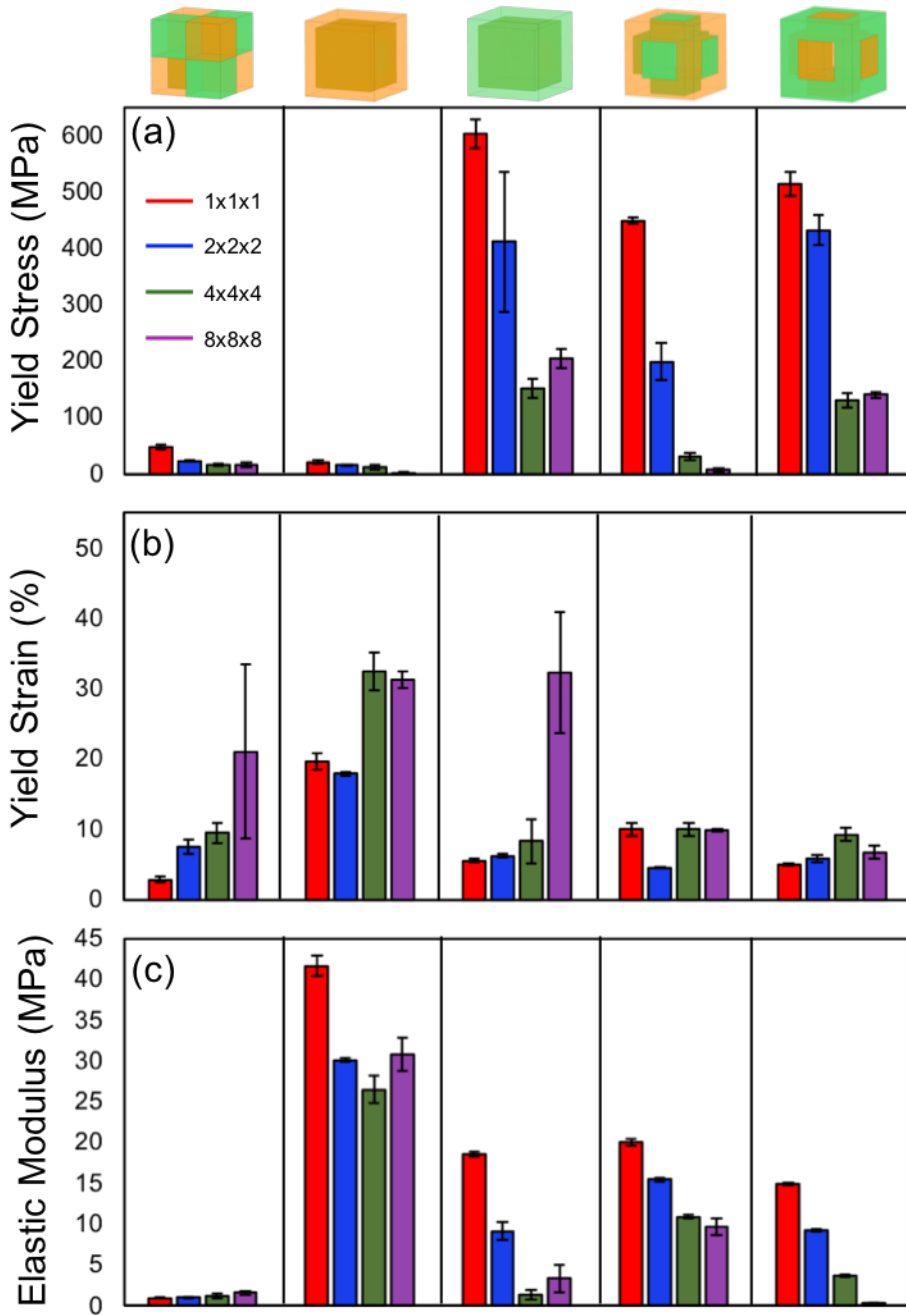


Figure 4.7. (a) Yield strain, (b) yield strength, and (c) elastic moduli of composites with decreasing unit cell size from experiments.

4.4 Conclusions

To summarize, five geometries of polymer composites were tested: a discontinuous phase composite (DPC), a matrix-inclusion composite (MIC) with stiff frame and one with a soft frame, and interpenetrating phase composites (IPC) with either a stiff or soft frame. Two types of comparison tests were performed. The first was to increase the number of unit cells while keeping the overall sample size the same, which effectively decreases the unit cell size. The second set of experiments explored the size effect of the unit cells on the mechanical properties of the composites. Key findings are:

- Yield strength and elastic modulus generally decrease as unit cell size decreases with the exception of the DPC, which has a fairly consistent elastic modulus and increased yield strength.
- While strain is predominantly in the soft phase (TangoBlack+) and localization of strain is seen in all samples, shear banding in the matrix-inclusion composite with a soft frame leads to overall material instability and sample bending for 4x4x4 and 8x8x8 samples.
- Contrary to the expected trends in most materials where smaller sample sizes result in higher strength, smaller 3D printed composites were shown to decrease in both strength and elastic modulus. Imperfections from 3D printing process are likely the cause of these results.

Chapter 4, in part, is in preparation for submission for publication as “Size and Scale Effects on Mechanical Properties of Additively Manufactured Two-phase Composites with Continuous or Discontinuous Phases,” 2018. The dissertation author is the primary investigator

and author on this paper. The work is co-authored by Fereshteh A. Sabet, Katherine Tang, Rachel Hsiong, Michael Tolley, Iwona Jasiuk, and Joanna McKittrick.

5 Radial-Concentric Freeze Casting Inspired by Porcupine Fish Spines

Freeze casting was introduced as early as the mid-20th century for technical applications requiring the use of refractory materials. The method uses the directional freezing of a colloidal suspension to produce a material with a controlled microstructure. As solvent crystals grow from one end of a suspension to another, particles become packed in between individual crystal arms, as shown in Figure 5.1. Then, the solvent is removed through lyophilizing (freeze-drying) so that a scaffold with a porous, aligned microstructure remains.

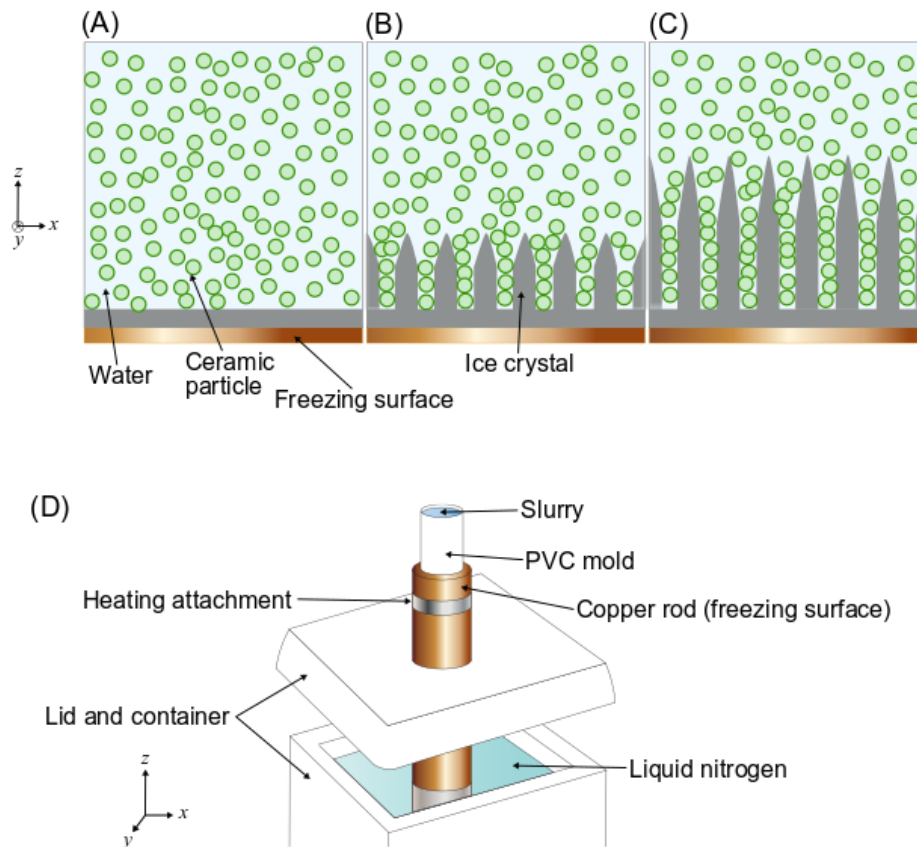


Figure 5.1. Packing of ceramic particles in between ice crystals during freeze casting. **(A)** Slurry of ceramic particles (green) suspended within water, in contact with freezing surface before cooling is applied. **(B)** Cooling of the freezing surface begins, and ice crystals begin to form at the freezing surface. **(C)** Cooling continues and ice crystals grow deeper into the slurry, packing more solute particles between them. **(D)** Conventional freeze casting setup.

Its benefit as a “near net-shape” processing method originally made it a candidate for the manufacturing of parts with complex curvatures such as turbine blades [173]. The flexibility of the freeze casting method quickly expanded the scope of research. To date, freeze casting has been used to manufacture a variety of cellular materials including metallic foams [174-177], nanowhisker scaffolds [178-181], graphene monoliths [182], and ceramic substrates for the aquaculture of coral [183]. In addition, the potential application to the manufacturing of biomaterials was recognized [184], as freeze casting results in a porous material with interconnected channels to allow for the proliferation of cells, and one may choose to cast materials that are biocompatible or bioactive. Therefore, others have focused on the freeze casting of porous scaffolds using biomedical grade ceramics such as hydroxyapatite [6, 185-188], alumina [189], and zirconia [190]. However, a continuing issue with these scaffolds is their ensuing lack of strength and toughness due to their high porosity.

Some researchers have used bioinspiration to improve the mechanical properties of freeze cast ceramics. A dense ceramic inspired by abalone nacre, using a slurry of alumina platelets mixed with alumina nanoparticles to create a ceramic material with high strength, toughness, compressive modulus, and thermal stability was manufactured by Bouville et al. [191]. Inspired by the narwhal tusk, Porter *et al.* [12, 116] used a rotating magnetic field to align magnetized ceramic particles during freezing; the resulting spiraling ceramic scaffold showed greater strength and stiffness in the direction of the magnetic field. Likewise, a magnetic field was used to align magnetized alumina particles during freeze casting; the resulting microstructures mimicked the aligned pores of spongy bone [7].

5.1 Microstructural control in freeze casting for bioinspired materials

The freezing process begins when cooling is applied to one end of a colloidal suspension of particles, called the slurry, and a planar freezing front (the advancing interface between solidified solvent crystals and liquid suspension) forms, as in Figure 5.1A. As the freezing front progresses, particles in the suspension can be rejected or engulfed by the solidifying solvent [192, 193]. Whether or not particles are engulfed or rejected depends on what configuration is favored by the interfacial free energy (between particle-solid, particle-liquid, and liquid-solid) [192]. An instability in the planar freezing front instigates a transition to dendritic growth of the solvent crystals, as in Figure 5.1B. Peppin *et al.* [194, 195], show through a linear stability analysis and experiments that constitutional supercooling in the liquid suspension ahead of the freezing front can cause such an instability. Then, freezing proceeds with the solvent crystals aligning themselves parallel to the thermal gradient imposed in the suspension [196]. Particles are rearranged and “packed” in between the solvent crystals, as in Figure 5.1C.

In conventional freeze casting setups (see Figure 5.1D), the slurry is contained in a non-conductive cylindrical mold (usually polyvinyl chloride, or PVC) positioned on top of a copper rod. Cooling is applied by immersing the bottom half of the copper rod in liquid nitrogen. The top surface of the copper rod, which is in contact with the slurry, acts as a “freezing surface.” This freezing surface imposes a vertically aligned gradient in temperature throughout the slurry so that growing solvent crystals are aligned longitudinally. Once the sample is completely frozen, the solvent phase is removed through freeze drying, and the resulting porous ceramic structure is typically held together by remaining polymer binder. The sample can be further processed through sintering or infiltration with a polymer.

Through freeze casting, one may specify the pore shape, pore size, and microstructural alignment by controlling the growth of solvent crystals during freezing. Microstructural control of the freeze cast ceramic can be achieved through “intrinsic” and “extrinsic” methods [8]. Intrinsic methods change the inherent freezing characteristics of the slurry and can include the choice of solvent, additives to the slurry, and choice of particle. For example, freeze casting a slurry of alumina particles in camphene results in a scaffold with rounded pores [14, 193, 197-199]. Meanwhile, freeze casting a slurry of alumina particles in water results in a scaffold with lamellar pores [200-203]. Extrinsic methods impose outside forces or parameters to affect the freezing process [8]. Examples of extrinsic methods of control include the magnetic freeze casting procedure [7, 12, 116] and a double freeze casting procedure, in which a freeze cast scaffold with one direction of alignment is infiltrated with slurry and freeze casted a second time orthogonal to the first direction of alignment, to make a scaffold with an interpenetrating “grid-like” structure with two directions of alignment [14, 115, 204]. Another extrinsic freeze casting method is “two-step freeze casting” where slurry is poured around a conventionally freeze cast scaffold which has not been lyophilized and the whole sample is freeze cast a second time; in this method, melting and refreezing of the first freeze cast scaffold was seen to create a blended interface between it and the portion of freeze cast scaffold from the second step [205].

A novel bioinspired freeze casting method was developed, which builds off of the extrinsic method hereafter referred to as “radial freeze casting.” Moon et al. [206] first developed a form of radial freeze casting using a metal cylindrical mold as the freezing surface so that resulting scaffolds were radially aligned. Later, an altered a conventional freeze casting setup (of the kind shown in Figure 5.1) by using a copper mold in lieu of a PVC mold was developed [207]. Thus, the bottom freezing surface imparted cooling to the copper mold so that the mold

acted as a second freezing surface. The microstructures of the resulting ceramic scaffolds were both longitudinally and radially aligned. The method described in this paper, which will be referred to as "radial-concentric freeze casting," uses radial freeze casting to create longitudinally and radially aligned structures. However, through a two-step process, it also introduces concentric structures. First, a radial freeze cast is performed similar to that in [207], with the exception of a copper pin placed in the center of the copper mold. Second, the copper pin is removed from the frozen solid, the void left by the pin is filled with more slurry, and a second freeze cast is performed. This step in the radial-concentric freeze casting method is similar to the two-step freeze casting method previously described [205], but it differs from two-step freeze casting in that the temperatures of the freeze cast solid and additional slurry are first equilibrated to prevent partial melting-recrystallization. The morphology of the layers arising from each step and the interfaces between them are explored in this paper.

5.2 Bioinspiration from the porcupine fish spine

This novel freeze casting method was inspired by the defensive spines of the porcupine fish, members of the family *Diodontidae*, which are found throughout most oceans in temperate environments [208]. Similar to the pufferfish, porcupine fish can inflate to approximately three times their initial volume by filling their stomachs with water or air; it is hypothesized that they do so to become too large for a predator to swallow [209]. However, porcupine fish also have an added layer of defense – modified scales in the form of stiff, sharp spines covering the body that orient outward when the fish inflates. One may infer that these spines must be strong enough to protect against a predator's bite. Meanwhile, the hundreds of spines covering the fish's body [210] must be lightweight enough for the fish to maintain neutral buoyancy.

In previous work, the defensive spines of the species *Diodon holocanthus* and *Diodon hystrix* were characterized [210]. The porcupine fish spine is composed of a combination of hydroxyapatite and collagen [210], similar to other fish scales [211]. It was shown that the hydroxyapatite and collagen phases form a concentric and radial alignment, as shown in Figure 5.2 [210]. Mechanical tests showed both transverse stiffness and strength many times greater than that of similarly composed biological materials [210, 211]. The authors of [210] posited that these mechanical property improvements derive from the radial and concentric alignment of the hydroxyapatite and collagen phases. This hypothesis has precedent from the literature, such as ceramics of alternating layers of dense and porous SiC [212] and CeZrO₂/Al₂O₃ [213] layered ceramics fabricated through slip casting.

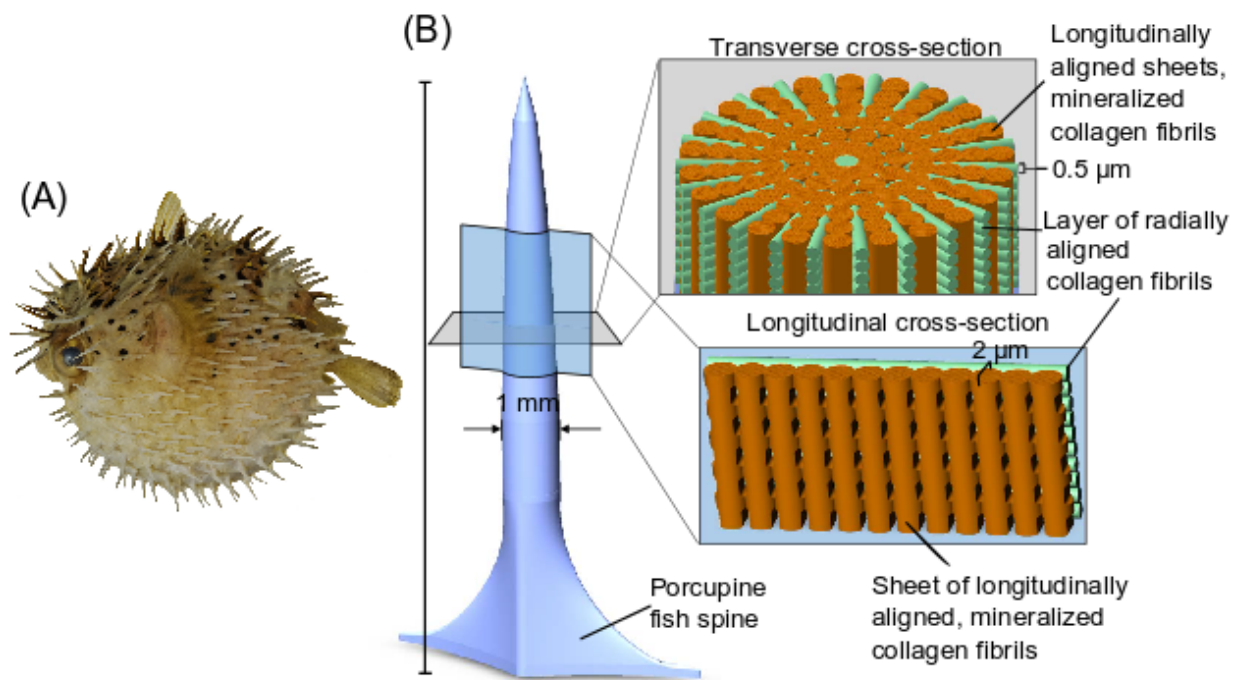


Figure 5.2. (A) Porcupine fish fully inflated, with defensive spines oriented outwards [214]. (B) Schematic of ultrastructure and microstructure of the porcupine fish spine, adapted from [210].

Inspired by the defensive spines of *Diodon holocanthus*, the radial-concentric freeze casting method was developed to align the scaffold's microstructure both radially and concentrically. Microstructures of the radial– concentric freeze cast ceramics were characterized using scanning electron microscopy (SEM) and compared to those of both conventional and radial freeze cast ceramics. Finally, axial (longitudinal direction parallel to bottom freezing surface) compression and Brazilian tests on conventional, radial, and radial-concentric freeze cast samples were performed.

5.3 Materials and Methods

5.3.1 Freeze casting

Ceramic slurries of 30 vol.% were made using alumina (Al_2O_3) powder (SM8, Baikowski, USA, Charlotte, NC) with a particle size of 300 nm as the solute and deionized water as the solvent. Water was chosen as a solvent so that ice crystals would form lamellar pores resembling the radially aligned hydroxyapatite phases of the porcupine fish spine. A binder of 1 wt.% polyethylene glycol (PEG 400, Alfa Aesar, USA, Ward Hill, MA) and a dispersant of 1 wt.% sodium polyacrylate solution (Darvan 811, Vanderbilt Minerals, LLC, USA, Norwalk, CT) were used. The Al_2O_3 powder was mixed with the binder and dispersant in deionized water and ball-milled for 24 hours. The ball-milled slurry was then degassed in a desiccator for 20 minutes and freeze cast at a cooling rate of -10°C per minute from 10°C to -170°C .

Conventional, radial, and radial-concentric freeze cast samples were prepared (see Figure 5.3A-C) and the resulting structures of each method were compared. A summary of samples manufactured and mechanically tested can be found in Table D.1. For conventional freeze cast samples (Figure 5.3A), a cylindrical PVC mold with an inner diameter of 17.4 mm was used so that freezing started from the base of the sample; ice crystals then grew vertically upwards and

were aligned longitudinally. For radially freeze cast samples (Figure 5.3B), a cylindrical copper mold of 17.4 mm inner diameter was used so that there were two origins of freezing: one at the base and another from the edges of the mold, resulting in both longitudinally and radially aligned porosity. For radial-concentric samples (Figure 5.3C), concentric rings were created in two steps. First, the sample was radially freeze cast using a copper mold and a 4.75 mm diameter copper pin placed in the center of the mold. Thus, freezing originated from three surfaces: the base, the surface of the outer copper mold, and the surface of the pin. Radially aligned ice crystals grew both inward from the mold and outward from the pin. These ice crystals then met halfway between each other to form an interface. In the second step, the pin was removed, slurry was poured into the resulting cavity of the freeze cast solid, and the sample was freeze cast again to form the center of the sample with radial alignment; thus, a second interface was formed between this center and the freeze casted solid from the first step. Prior to pouring the slurry into the cavity, the temperatures of the freeze cast solid and the slurry were equilibrated through thawing of the freeze cast solid and cooling of the slurry. The solid was thawed to a temperature between $-5-0^{\circ}\text{C}$, with temperature measured by contact of the top surface of the solid with a thermocouple, to lessen its effect as an unintended freezing surface. The slurry was cooled to a temperature between $0-5^{\circ}\text{C}$ by partially submerging the slurry container in liquid nitrogen, with temperature again measured using a thermocouple, so that it would not melt the solid as it was poured in. Neglecting to equilibrate the temperatures of the freeze cast solid and slurry resulted in multiple unevenly spaced rings radiating from the center (Figure D.1).

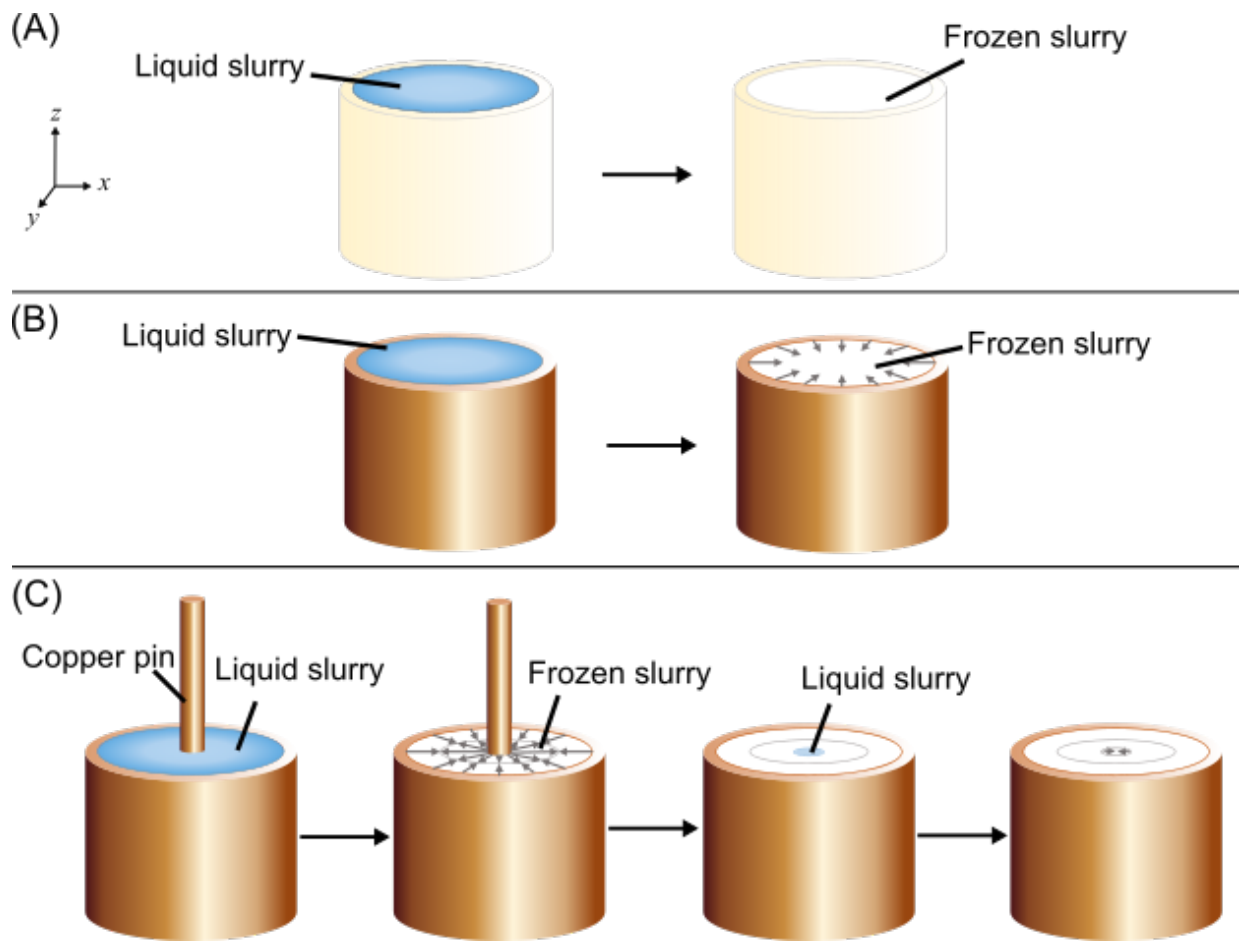


Figure 5.3. Overview of freeze casting methods (bottom freezing surface underneath molds not shown). **(A)** Conventional freeze casting, **(B)** radial freeze casting and **(C)** radial-concentric freeze casting. A copper pin is placed in the center of the copper mold. Then, the direction of freezing, shown by the gray arrows, is outward from the copper pin and inward from the copper mold. The pin is removed and the remaining void is filled with liquid slurry, and then cooling is applied again.

Samples were then freeze dried (Labconco, Kansas City, MO, USA) at -50°C and 3.5×10^{-6} Pa. Samples were sintered in an open-air furnace for three hours at 1500°C , with heating and cooling rates of $2^{\circ}\text{C}/\text{minute}$. Samples were 14 mm in diameter (shrinkage of sample diameters was a result of sintering). Approximately 1.5 cm of bottom portions of samples were removed, and samples were cut to ≈ 14 mm in length.

Additionally, a separate set of samples were infiltrated with epoxy (EpoxiCure 2 Epoxy System, Buehler, Lake Bluff, Illinois, USA). Samples were immersed completely in epoxy and

degassed for 30 minutes. Samples were then removed from the epoxy and allowed to cure overnight.

5.3.2 Microstructural characterization

Microstructures of radial and radial-concentric samples were observed using an environmental SEM (FEI/Philips XL-30, FEI, Hillsboro, OR, USA). To prepare samples for SEM, the finished ceramic sample (of 14 mm in height) was cut using a rotary saw so that approximately 4 mm from the top and bottom ends were removed. Then, cut surfaces were polished using 90 grit and 600 grit sandpaper. Samples were fixed to a sample stub using carbon tape and carbon paint and sputter coated with iridium (Emitech K575X, Quorum Technologies Ltd, East Sussex, UK) for 15 seconds at 85 mA. Samples were imaged under 10 kV accelerating voltage. Full axial cross sections of conventional, radial, and radial-concentric freeze cast samples were made by stitching together individual SEM images to create a composite image.

5.3.3 Mechanical testing

The cylindrical freeze cast samples were tested in axial compression and analyzed according to ASTM standard C39/C39M-15A [215]. Axial compressive strength was calculated based on the maximum nominal stress. Axial compressive modulus was calculated through the slope of the initial linear portion of plots of the nominal stress versus nominal strain. Uninfiltrated and infiltrated samples were loaded at a crosshead speed of 10^{-3} /s until failure. Uninfiltrated samples were tested using an Instron 3342 testing machine with a 500 N load cell (Instron, Norwood, MA, USA), while infiltrated samples were tested using an Instron 3367 testing machine (Instron, Norwood, MA, USA) with a 30 kN load cell.

Brazilian tests were performed according to ASTM standard D3967-08 [216] to find the splitting tensile strength of samples. Previous studies tested samples of porcupine fish spines to

tensile failure in bending [210]. Thus, it was desirable to obtain tensile properties of our freeze cast samples. However, the dimensions of the samples that can be produced through freeze casting make it difficult to test in three-point bending, since a suitable length to diameter ratio according to ASTM standards cannot be achieved. Brazilian tests had previously been developed to find the tensile strength of ceramic samples that are difficult to test using more common uniaxial tension test setups [217]. The relationship between the splitting tensile strength (σ_t) and failure load and sample dimensions is given by:

$$\sigma_t = \frac{2P}{\pi LD} \quad (1)$$

where P is the failure load, L is the height of the cylindrical sample, and D is the diameter [215].

Samples were loaded in the transverse direction at a crosshead speed of 10^{-3} /s. Both infiltrated and uninfiltrated samples were tested using an Instron 3367 testing machine (Instron, Norwood, MA, USA) with a 30 kN load cell.

For statistical analysis of mechanical test results, ANOVA with a general linear model was used. Sources of variance included: structure (conventional, radial, or radial-concentric) and infiltration (uninfiltrated or infiltrated with epoxy), and their interaction. A general linear model was used to determine whether the means of a particular mechanical property of two groups differed significantly. If $p < 0.05$, then a source of variance is said to have a significant impact on that particular mechanical property. Multi-factor, post hoc Tukey tests were used to determine whether samples with different structure and/or infiltration were statistically the same or different based on their mechanical test results.

5.4 Results and Discussion

Images of the axial cross sections of samples in Figure 5.4 show distinct microstructural differences between samples produced through the three freeze casting methods. Conventional

freeze cast samples have a microstructure with random alignment (Figure 5.4A), radial freeze cast samples have a microstructure that is radially aligned (Figure 5.4B), and radial-concentric freeze cast samples have a radially aligned microstructure with concentric rings (Figure 5.4C). The radial-concentric freeze cast scaffolds had three distinct layers. The outer and middle layer and the interface between them is a result of the first step in the radial-concentric method; we call this interface the “outer” interface. The core layer is the result of the second freeze casting step, and we call the interface between the core and middle layer the “inner” interface.

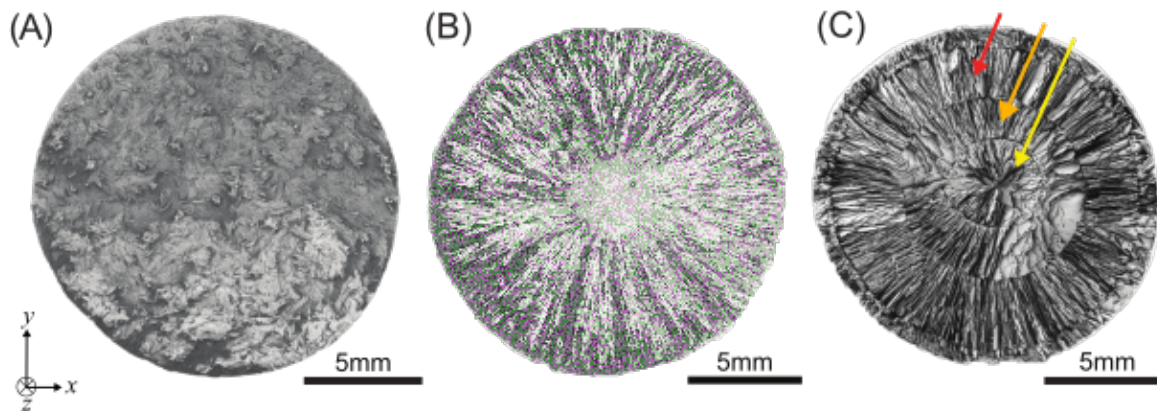


Figure 5.4. Freeze cast samples composed of 30 vol.% alumina. Full composite images of axial cross sections of each sample were created by stitching together multiple images, with each individual image taken at approximately $38\times$ magnification. Samples freeze cast through (A) conventional, (B) radial, and (C) radial-concentric methods are shown. In (C) the outer, middle, and core layers are pointed out by the red, orange, and yellow arrows, respectively.

5.4.1 Radial and radial-concentric freeze casts: axial cross sections

In Figure 5.5, close-up views of the microstructural features of radial and radial-concentric freeze cast samples are shown. Similar to other works in which water was used as the solvent [200, 207], the walls of these samples are lamellar. The average wall thicknesses of the lamellae were measured (Table 5.1). For radial freeze casts, the measurements were taken from near the outermost and innermost portions of the representative sample. For radial-concentric

freeze casts, similar measurements were taken from the outermost and innermost portions of the outer and core layers.

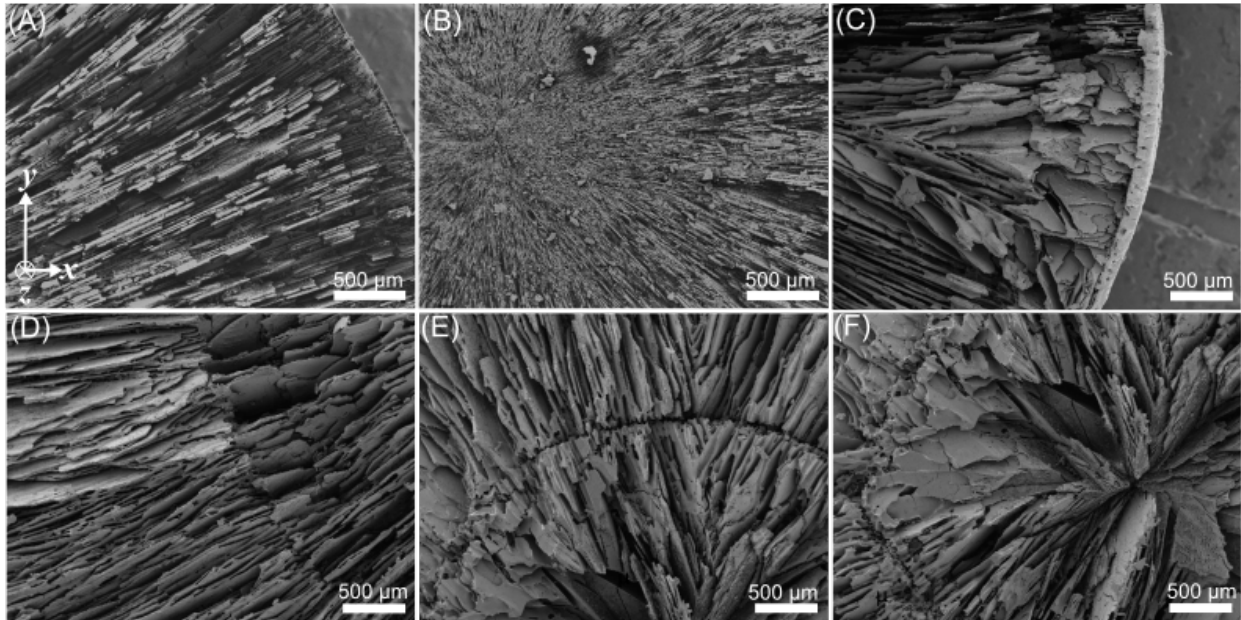


Figure 5.5. Scanning electron microscopy images of freeze cast samples composed of 30 vol.% alumina. Radial freeze cast (A) outermost region and (B) innermost region. Concentric freeze cast (C) outer layer, outer region; (D) outer layer, inner region; (E) core layer, outer region; (F) core layer, inner region.

Table 5.1. Wall thicknesses of lamellae, where N is the number of measurements taken and SD is the standard deviation. Measurements were taken using ImageJ software.

Freeze Cast Type	Zone	Region	N	Thickness \pm SD (μm)	Porosity (%)
Conventional	N/A	N/A	50	46 ± 15	$17.8\% \pm 0.6\%$,
Radial	N/A	Outer	50	14 ± 4	$21\% \pm 2\%$
Radial	N/A	Inner	50	8 ± 2	
Radial-concentric	Outer layer	Outer	53	19 ± 6	$30\% \pm 2\%$
Radial-concentric	Outer layer	Inner	51	17 ± 3	
Radial-concentric	Core layer	Outer	53	21 ± 6	
Radial-concentric	Core layer	Inner	50	12 ± 5	

In radial and radial-concentric freeze casts, there is a decrease in wall thicknesses when traveling from the outer surface of the sample to the center, which was also observed in other radial freeze cast samples [207]. At the very center of both radial and radial-concentric freeze cast samples, it can be seen that lamellae become significantly smaller and more tightly spaced together (Figure 5.5). This spacing may be due to either an increase in the freezing front velocity (lamellae spacing is inversely proportional to the freezing front velocity [200]) or the forces the ice crystals impose on each other as their growth converges towards the center. It is interesting to note that the center layer of radial-concentric samples not only have thinner wall sizes, but the walls seem to meld together into superstructures where striations of the individual lamellae are still visible.

The porosity of uninfiltated conventional, radial, and radial-concentric freeze cast samples were also measured. Measurements were made by using ImageJ software to analyze SEM images of representative samples. Fifteen SEM images per sample type were analyzed and porosities were found to be $17.8\% \pm 0.6\%$, $21\% \pm 2\%$, and $30\% \pm 2\%$ for conventional, radial and radial-concentric freeze casts, respectively. Although slurries with the same volume percentage of alumina particles were used in each method, the porosities of samples from each freeze casting method differ due to the fact that slurries were not confined to a constant volume during freezing.

5.4.2 Radial freeze cast: longitudinal cross section

A longitudinal cross-section of a representative radial freeze cast sample, after freeze-drying and sintering, is shown in Figure 5.6, showing the lamellae, which form the negative of the ice crystal primary dendrites.

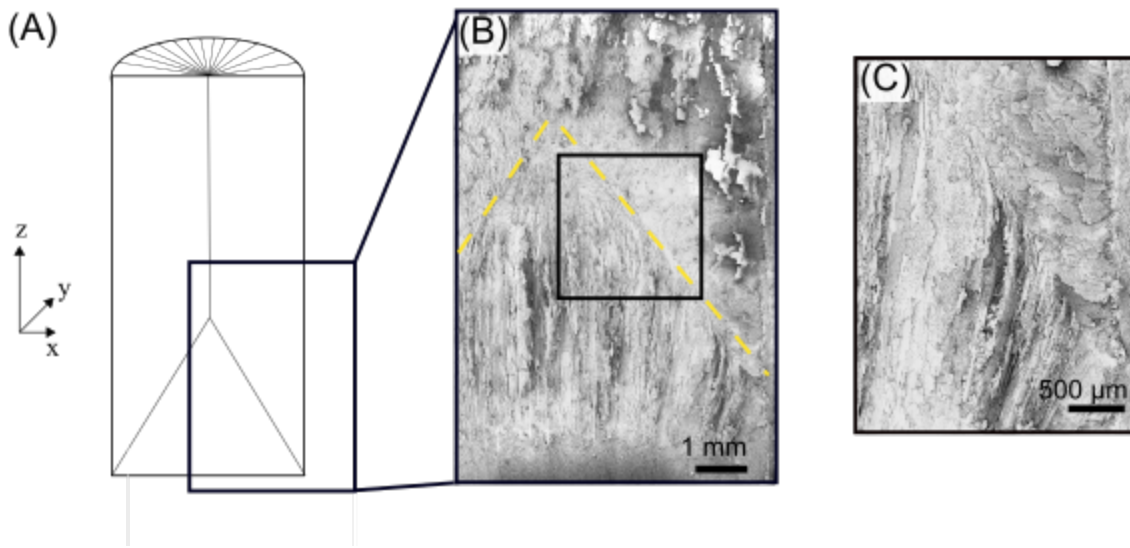


Figure 5.6. Longitudinal cross section of radial freeze cast sample. **(A)** Schematic diagram of longitudinally sectioned freeze cast sample. **(B)** Composite scanning electron microscopy image of longitudinal section in blue boxed area in (A) with yellow dotted line delineating the meeting of lamellae growing longitudinally from the bottom freezing surface and lamellae growing radially from the cylindrical copper mold. **(C)** Zoomed-in view of boxed area in (B).

Through X-ray in-situ radiography and tomography, Deville et al. [196] observed the morphology of longitudinal cross sections of a slurry during conventional freeze casting. Two phases of freeze casting were noted: the “initial instants” of solidification, where the orientation of ice crystal growth proceeds randomly without long-range order, and a transition into a “steady state” growth in which lamellar ice crystals grow parallel to the temperature gradients imposed in the slurry.

In the representative radial freeze cast sample shown in Figure 5.6, its equivalent initial instants of freezing encompass approximately the first centimeter of the sample, as measured from the bottom freezing surface. The length is similar to that previously reported [196], however, there are some differences between the longitudinal cross sections.

In [196], it was observed that in the initial instants, there was a mix of two kinds of ice dendrites: ones whose primary axis of growth are longitudinally in the direction parallel to the

thermal gradient and another whose growth axis is perpendicular to the thermal gradient (secondary dendrites), that arise from instabilities on the primary dendrites. The combination of the anisotropy of the ice crystals and the thermal gradient within the slurry is what causes the continued steady-state growth of these ice crystals to be oriented parallel to the temperature gradient. In contrast, initial crystal growth in the radial freeze cast (Figure 5.6B) is already mostly parallel to the thermal gradient imposed by the bottom-freezing surface. In addition, crystals also grow radially inward from the copper mold; exposed radially oriented lamellae are shown in the region above the yellow dashed line in Figure 5.6B).

Furthermore, the transition from the relatively turbulent initial instants to a steady-state is different from that observed through conventional freeze casting. This transition occurred gradually at approximately 1.5 cm through the longitudinal length of the sample [196]. For the radial freeze cast sample, the transition between the initial instants to steady-state growth is well-defined. As shown in Figure 5.6B, crystals growing radially from the copper cylindrical mold meet crystals growing longitudinally from the bottom freezing surface at an interface oriented at $\sim 45^\circ$ with respect to the bottom surface.

Closer inspection of this interface shows that crystals growing longitudinally become perturbed from their original direction of growth, curving away from crystals growing radially (Figure 5.6C). It is not clear if these curved edges are influenced more by the dual temperature gradients, created by the bottom freezing surface and the radial freezing surface, or by physical forces. These forces can arise due to the growth of the radially oriented crystals impeding the growth of longitudinally growing crystals.

5.4.3 Radial concentric freeze casts: outer interface

In Figure 5.7, representative close-up images of the outer and inner interfaces of the same radial-concentric freeze cast in Figure 5.4C are shown. Figure 5.7A is the same composite SEM image from Figure 5.4C but with different annotations. A representative close-up image of the interface of the outer interface of a radial-concentric freeze cast is shown in Figure 5.7B. This interface was formed in the first step of our radial-concentric freeze casting method, in which freezing fronts propagating from the inner copper pin and the outer copper mold met.

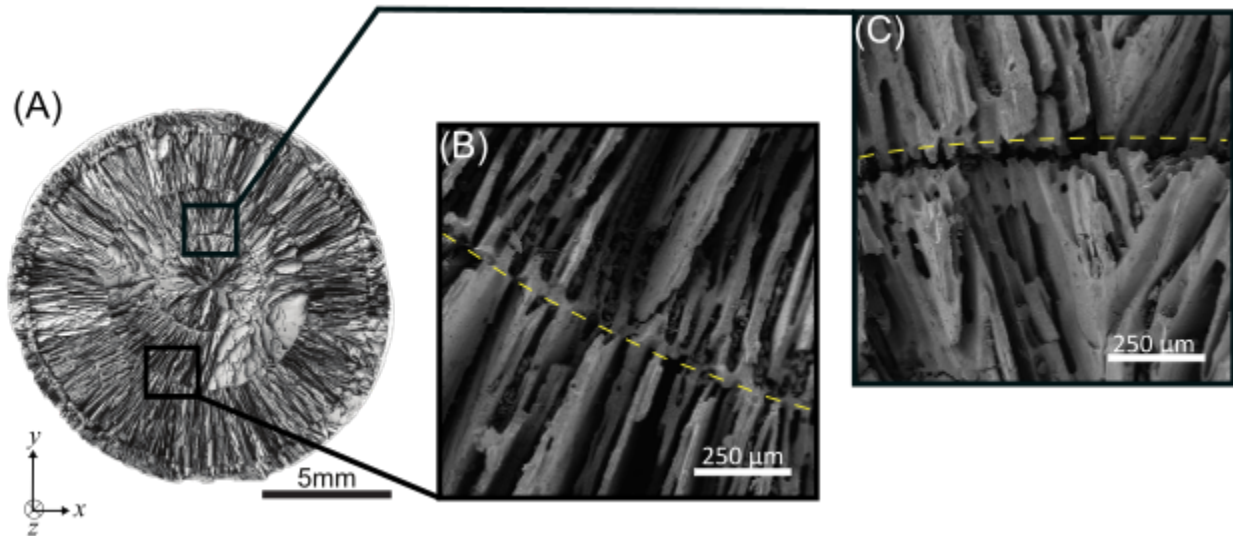


Figure 5.7. (A) Scanning electron microscopy images of inner and outer rings in a representative radial-concentric freeze cast sample. (B) Zoomed-in image of boxed region in (A) of inner ring, with yellow dashed line highlighting the interface. (C) Zoomed-in image of boxed region in (A) of outer ring, with yellow dashed line highlighting the interface.

The phenomenon used here, the meeting of two freezing fronts, should have been present in the double-sided (top and bottom solidification plates) cooling setup previously reported [202]. However, it is not clear if they observed an interface at the meeting of two freezing fronts. Similarly, the double-sided cooling method was explored to create more consistent lamellae spacing [218]. Yet, it is not clear from either the description of results or the images presented if the authors observed an interface. To date, it does not seem that anyone in the literature has

commented on this particular facet of freeze casting. Considering that the use of multiple freezing surfaces may be investigated as a way to scale up freeze casting, it would be helpful to understand the properties at such an interface.

An explanation for the morphology of this outer interface may be found in considering the interactions of the tips of the ice crystals as they reach each other. Similar to conventional freeze casting, ice crystal growth first begins at the freezing surfaces (Figure 5.8A). Then, the tips of ice crystals growing from two opposite freezing fronts ((Figure 5.8B) approach each other, and particles are pushed ahead until they become packed at that interface ((Figure 5.8C). The tips of ice crystals growing inward from opposite directions may either merge or be stopped due to the packed particles, resulting in the “suture-like” structure seen in Figure 5.7B. Further work should be done to explore the factors that influence the morphology of the interface at the meeting of two freezing fronts.

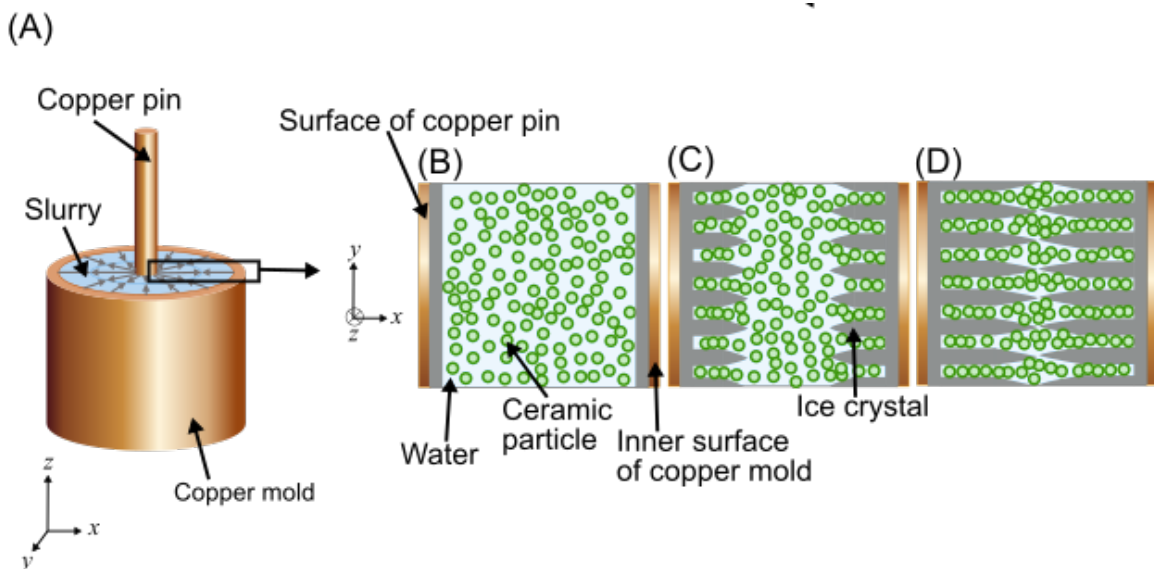


Figure 5.8. Schematic of packing of ceramic particles at the outer interface. **(A)** The setup of the radial-concentric freeze casting method in the first step of the process (showing a 3-dimensional view per the axes in the bottom left corner), with a schematic representation of the boxed region shown in a top-down view in (B)-(C). **(B)** Initial solidification of water at each freezing surface. **(C)** Growth of ice crystals at opposing freezing surfaces. **(D)** Meeting of ice crystals packing ceramic particles at the interface.

5.4.4 Radial concentric freeze casts: inner interface

The interface of the inner interface of the radial-concentric freeze cast is clearly defined in Figure 5.7B. The inner ring was formed by pouring more liquid slurry into the hollow center of an already freeze cast solid and then freezing a second time. This freezing step was performed after equilibrating the temperatures of both the additional liquid slurry and the freeze cast solid to prevent melting and re-freezing of the freeze cast solid. The effects of this temperature equilibration on the morphology of the inner interface can be understood by comparing the sample shown in Figure 5.7B (equilibrated) against the sample shown in Figure D.1 (not equilibrated) and against the samples produced through the two-step freeze casting method previously reported [205]. The latter two cases have blended interfaces due to the melting of the freeze cast solid as it comes into contact with the higher temperature liquid slurry and re-freezing upon freeze casting.

5.4.5 Mechanical test results

Figure 5.9 shows the mechanical testing results for uninfiltated samples in the left column and for infiltrated samples in the right column. Statistical similarity between results were analyzed using multi-factor Tukey tests; these results are shown by the brackets (labeled “n.s.” to signify sets of results which have no significant difference) in Figure 5.9. Generally, for each property (axial compressive strength, axial compressive modulus, and splitting tensile strength), uninfiltated samples are statistically similar regardless of structure. However, with infiltration, the mechanical properties of samples begin to differ.

A general linear model was used to analyze sources of variance between samples; p-values from this analysis are summarized in Table D.2. This analysis shows that infiltration, but

not structure, significantly influences axial compressive strength. Structure and infiltration both contribute to variances in axial compressive modulus, but the combined effect of structure and infiltration contribute greater variance than the sum of their individual contributions, meaning that the interaction between the factors has a significant impact on axial compressive modulus. Similarly, structure and infiltration interact to have a greater combined effect on splitting tensile strength. Therefore, while infiltration affects axial compressive strength, axial compressive modulus, and splitting tensile strength, structure only affects axial compressive modulus and splitting tensile strength.

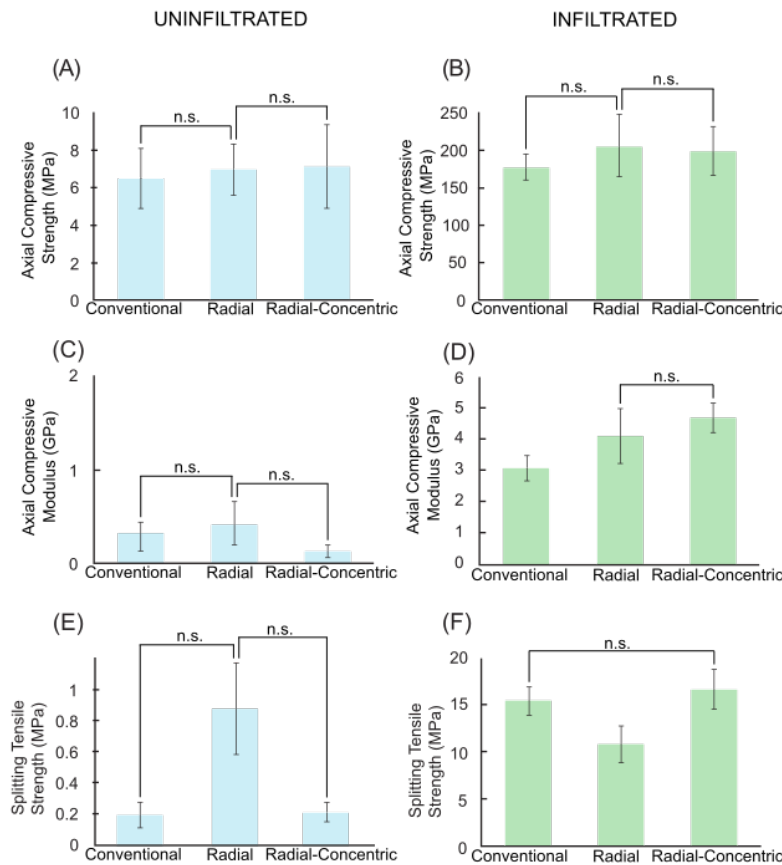


Figure 5.9. Results from mechanical testing, where brackets labeled “n.s.” indicate results found to have no significant difference under Tukey pairwise comparisons for both structure and infiltration. Axial compressive strength in (A) uninfiltred and (B) infiltred samples from axial compression tests. Axial compressive modulus of (C) uninfiltred and (D) infiltred samples measured from axial compression tests. Splitting tensile strength of (E) uninfiltred and (F) infiltred samples measured from Brazilian tests.

Axial compressive strength values for uninfiltreated conventional, radial, and concentric samples are 6.5 ± 1.6 MPa, 6.7 ± 1.3 MPa, and 7 ± 2 MPa, respectively, and values for infiltrated conventional, radial, and concentric samples are 180 ± 20 MPa, 200 ± 40 MPa, and 200 ± 30 MPa, respectively (Figure 5.9A). Infiltrated samples all have statistically similar axial compressive strengths. Therefore, structure does not affect the axial compressive strengths of the freeze casted samples while infiltration does. These results are likely due to all scaffold types having vertically aligned microstructures.

Axial compressive modulus values (shown in Figure 5.9B) for uninfiltreated conventional, radial, and concentric samples are 290 ± 140 MPa, 400 ± 200 MPa, and 110 ± 40 MPa, respectively. Axial compressive modulus values for infiltrated conventional, radial, and concentric samples are 3000 ± 400 MPa, 4000 ± 800 MPa, and 4600 ± 500 MPa, respectively. Infiltrated radial freeze casts have a modulus similar to that of infiltrated radial-concentric freeze casts, while infiltrated conventional freeze casts are less stiff. The differences between uninfiltreated and infiltrated samples highlight the importance of structure in multi-phase materials. Without infiltration, radial-concentric samples have the lowest axial compressive modulus amongst the three sample types, but after infiltration, they have the highest axial compressive modulus. Often, hierarchical arrangements of stiff and soft phases of materials are the sources of remarkable mechanical properties that cannot be predicted a simple “rule of mixtures” [1, 156]. These results show that the radial and concentric structure of the ceramic and collagen phases in the porcupine fish spine may be the source of similar improvements.

Finally, splitting tensile strengths for uninfiltreated conventional, radial, and concentric samples are 0.19 ± 0.08 MPa, 0.9 ± 0.3 MPa, and 0.21 ± 0.06 MPa, respectively (Figure 5.9c). Splitting tensile strengths for infiltrated conventional, radial, and concentric samples are $15.4 \pm$

1.5 MPa, 10.8 ± 1.9 MPa, and 17 ± 2 MPa, respectively. After infiltration, conventional and radial-concentric freeze cast samples have significantly higher splitting tensile strengths than radial freeze cast samples. These changes in the relative values of splitting tensile strengths in uninfiltrated and infiltrated samples might be attributed to the changes in what can be considered the weak phases in the microstructures of the samples. In all uninfiltrated samples, the porosity guides the crack formation. This is seen in many biological materials including the porcupine fish spine and bone [219]. Cracks will travel through porous regions, forming patterns mirroring the alignment of the microstructures formed by lamellae. Figure 5.10A-C show crack patterns formed in representative uninfiltrated samples after Brazilian tests, which corroborate the Brazilian test results described above. For a conventional freeze cast sample (Figure 5.10A), the crack forms jagged surfaces due to the random orientation of the microstructure, and a crack is deflected when it encounters a region with lamellae aligned in a direction different from its original direction of travel. Radial samples (Figure 5.10B) tended to have relatively straight cracks, which followed along the radially aligned pores of the microstructure. Since there is relatively little bridging in the radial samples, the crack progresses through the whole sample easily. Finally, cracks in radial-concentric freeze cast samples (Figure 5.10C) followed the radially aligned pores, traveling through the outer interface, before diverting into the apparently weak interface of the inner interface. There is a clear crack deflection at every interface between the different layers. This difference in crack propagation between the two rings in radial-concentric samples may be caused by their different microstructures. The outer interface is more enmeshed than the relatively well-defined inner interface. However, the crack propagation along the inner ring may also be due to the difference in the radius of curvature; the smaller radius of

curvature of the inner ring may make it more favorable for the crack to follow along that interface rather than break through the interface, as it did with the outer interface.

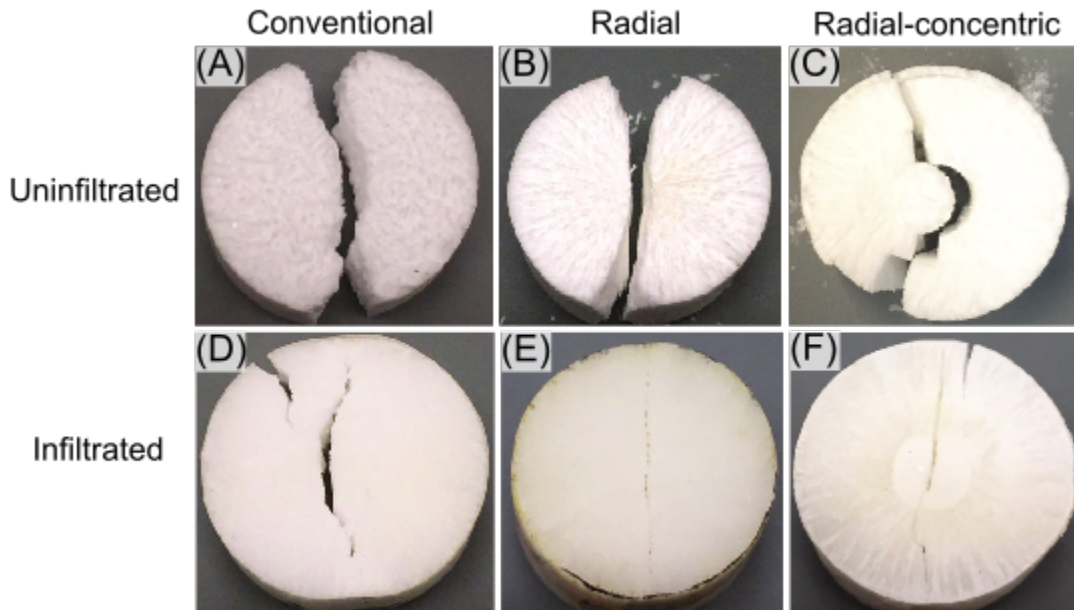


Figure 5.10. Crack patterns in representative samples after Brazilian testing. **(A)** Uninfiltrated conventional. **(B)** Uninfiltrated radial. **(C)** Uninfiltrated radial-concentric. **(D)** Infiltrated conventional. **(E)** Infiltrated radial. **(F)** Infiltrated radial-concentric.

In the infiltrated samples, the weak regions are instead the brittle lamellae encased within the epoxy phase. Figure 5.10D-F show crack patterns formed in representative infiltrated samples after having undergone Brazilian tests. For conventional freeze cast samples, the random orientation of the lamellae means that there is no specific path of weakness for the crack to travel; thus the sample splits down the center, where the stress is highest for the Brazilian test configuration [217]. In infiltrated radial freeze cast samples, the radial alignment of the relatively weak lamellae creates a line down the center of the sample. The samples split in half along this line at a force lower than that needed to split a conventional freeze cast sample. In a radial-concentric freeze cast sample (Figure 5.10F) a crack does not form along the inner interface as it did in an uninfiltrated sample (Figure 5.10C) since this inner interface is filled with the epoxy phase, which is tougher than the brittle ceramic phase. Consider that a crack, which is traveling

along one of the brittle lamellae, is surrounded on both sides by epoxy phases. Thus, once the crack reaches the inner interface, it is forced to travel through the inner interface.

Splitting tensile strengths of conventional and radial freeze cast samples from [207] were calculated based on the sample geometries and failure force values (failure force values were taken directly from data points given in the plots, interpolated between data points, or extrapolated from nearest data point). At 20% porosity, their conventional freeze and radial freeze cast samples the splitting tensile strengths are 6.4 MPa and 8.5MPa, respectively. The splitting tensile strength values for conventional and radial freeze casted samples in the present work are much lower than those calculated from the results given in [207]. The differences may be attributed to differences in particle size, freezing, sintering procedures and test sample geometry. Despite the differences between these results and previous results, both sets of results showed similar trends of conventional freeze cast samples having lower splitting tensile strengths than radial freeze cast samples.

5.5 Conclusions

A novel radial-concentric freeze casting method inspired by the radial and concentric structure of the porcupine fish spine was successfully developed. Radial-concentric freeze cast porous ceramics were compared with samples freeze cast through radial and conventional freeze cast methods. It was found that:

- Radial-concentric freeze casted samples from our two-step freeze casting process had three layers. Outer two layers resulted from the first step in the process, in which two freezing fronts met to form an interface. The inner core layer resulted from the second step in the process, where another interface could be seen between this core layer and the layer formed in the first step of the freeze cast method.

- Radial-concentric scaffolds had axial compressive strengths similar to those of conventional and radial freeze cast scaffolds.
- When infiltrated with epoxy, radial-concentric freeze casted ceramics had significantly improved axial compressive modulus over uninfiltrated radial-concentric freeze casts, especially when compared against the effects of infiltration in conventional or radial freeze casted ceramics.
- Amongst uninfiltrated samples, radial-concentric freeze casted ceramics had one of the lowest splitting tensile strengths. With infiltration, radial-concentric freeze casts improved significantly to having the highest splitting tensile strength.
- In comparison, uninfiltrated radial freeze casts initially had the highest splitting tensile strength. Upon infiltration, the splitting tensile strength of radial freeze casts only improved moderately.

These findings suggest that the radial-concentric samples can be considered to have optimal improvements in all three mechanical properties once infiltrated. Our results highlight the importance of structure in multi-phase materials. Mechanical properties between single phase and multi-phase materials with the same structure can differ significantly. These differences in mechanical behavior can be utilized for design of improved engineering materials.

Chapter 5, in part, is in preparation for submission for publication as “Radial-Concentric Freeze Casting Inspired by Porcupine Fish Spines,” 2018. The dissertation author was one of the primary investigators and authors on this paper. This work is co-authored by Joyce R. Mok and Joanna McKittrick.

6 Freeze Cast Composite of Hydroxyapatite and Demineralized Bone

6.1 Introduction

Osteoporosis affects more than 200 million people worldwide, leading to weakened bone that can result in fractures [220]. This sometimes necessitates bone grafts or implants for traumatic fractures. Current implants are often made from metal alloys, and while they are strong, they are much stiffer than the local bone that they are implanted into. This mismatch in stiffness results in stress shielding, where local bone mass or density decreases due to lower stress experienced by the bone [221]. This can cause implant loosening, resulting in interfacial failure of the implant. It can also make subsequent revision surgeries difficult. In contrast, ceramics are much more biocompatible and even osteoconductive in the instance of hydroxyapatite (HA) when compared to metals. However, ceramics are brittle and fail catastrophically under tensile or shear loading.

Many attempts have been made to mimic the structure of bone using ceramic materials as well as bone's actual constituents, type I collagen and hydroxyapatite. A review by Wahl, et al. [222], details a few methods for creating collagen-HA composite scaffolds. One method often used is the *in vitro* mineralization of collagen [223-225]. Vacuum infiltration of collagen into an HA scaffold is also done, by creating a porous HA scaffold through burning out polybutylmethacrylate beads and then infiltrating with collagen [226]. In addition, electro-spun collagen with hydroxyapatite particles embedded in the matrix have been made [227-229]. However, these electrospun scaffolds are often tested in tension rather than compression, which is the main loading condition of bone. Furthermore, these materials contain very little HA and are often compliant with elastic moduli ranging from 2.67-11.10 MPa [229]. Villa, et al. [230] created a collagen-HA freeze cast scaffold using a slurry of water-dissolved collagen and

precipitated nanocrystalline HA particles from a modified simulated body fluid solution. This method once again created a matrix of collagen with suspended HA particles. The composition of the scaffold was ~15 wt. % water, ~61 wt. % collagen, and ~24 wt. % HA, and mechanical properties of the scaffold were not evaluated.

Freeze casting, or ice templating, in particular has been used to mimic the structure of bone mineral. The technique synthesizes lamellar ceramic scaffolds with interconnected pores, simulating the structure of spongy bone. Freeze casting has been done with a variety of ceramics including hydroxyapatite [231], the ceramic found in bone. Ice templating has also been used with polymers [232] and more recently, collagen [118], the protein found in bone. Divakar, et al. [118] created a freeze casted collagen scaffold with aligned porosity. Freezing rate was varied to observe changes in structure and mechanical properties [233].

In this study, freeze casting of a ceramic scaffold is combined with freeze casting of collagen in a two-step process. As has been found in [156], a continuous stiff phase is necessary for high stiffness in a two-phase composite. This is done by creating an HA scaffold with a continuous ceramic phase. A collagen solution is infiltrated and freeze casted to create directional, interpenetrating porosity. The result is a collagen-HA composite that has potential to be used as a biomaterial for bone implants.

6.2 Materials and Methods

Combined HA and collagen samples are made through a two-part process shown in Figure 6.1. In the first part, HA particles are magnetized and magnetically freeze cast. Samples are then freeze dried and sintered. In the second part of the process, the sintered HA scaffolds are placed back into the freeze casting molds and infiltrated with the collagen/acetic acid solution. Specific methods for each section are described in subsequent subsections.

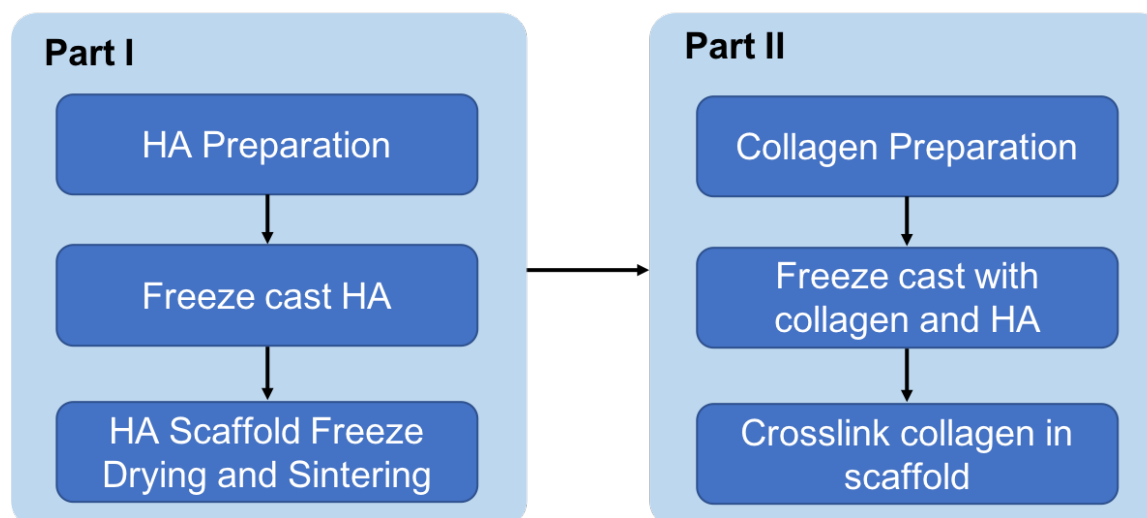


Figure 6.1. Process for making a combined hydroxyapatite (HA) and collagen freeze cast scaffold. The process is divided into two parts. Part I consists of HA preparation, freeze casting, and sintering. Part II involves preparing the collagen solution, combined freeze casting with HA and collagen, and crosslinking the collagen in the composite scaffold.

6.2.1 Magnetic Freeze Casting of Hydroxyapatite

HA particles of $\sim 2 \mu\text{m}$ diameter (Trans Tech, Adamstown, MD, USA) are first magnetized with iron oxide particles similar to the methods described in [7, 234]. To prepare the magnetized slurry, magnetized HA particles (10 and 20 vol%) were mixed with the following wt% quantities of binders and dispersants: 1 wt% polyvinyl alcohol (PVA 100,000 g/mol molecular weight (MW), Alfa Aesar, Ward Hill, MA, USA), 1 wt% polyethylene glycol (PEG, 10,000 g/mol MW, Alfa Aesar, Ward Hill, MA, USA), and 1 wt% Darvan 811 (R.T. Vanderbilt Company, Inc., Norwalk, CT, USA). The slurry was added to a container with alumina grinding media and ball milled for 24 hours.

After ball milling, the slurry was separated from the alumina grinding media and placed in a PVC mold. The PVC mold is placed between two $\sim 420 \text{ mT}$ bar magnets (N52 grade, K&J Magnetics, Inc. Pipersville, PA, USA) with a separation distance of 9.9 cm so that the magnetic field is $\sim 25 \text{ mT}$ according to the fitting curve in the Supplementary Material of [7]. The slurry was then freeze cast using a freezing rate of $-10^\circ\text{C}/\text{min}$ down to -170°C . The direction of the

magnetic field alignment will be referred to the y -axis while the direction of the ice growth that is perpendicular to the freezing surface is the z -axis. After freeze casting, samples were freeze dried (Labconco, Kansas City, MO, USA) for two days at -50°C and a vacuum pressure of 3.5×10^{-6} Pa. Samples were sintered in an open-air furnace for three hours at 1300°C , with heating and cooling rates of $2^{\circ}\text{C}/\text{minute}$.

6.2.2 Collagen Extraction

6-month porcine femur bone was first cut into slices of 2 mm thickness. Bone slices were then submerged in 0.5 M HCl for demineralization using the process described in Chapter 3. After transparency of samples were achieved, demineralized bone was moved to a solution of 0.05 M acetic acid to dissolve the bone collagen and placed on a magnetic stirrer for two days, during which the mixture was kept on ice. After the first day, demineralized bone was blended using an immersion blender to break larger demineralized bone pieces into smaller units. After the two days of dissolving, the acid-collagen solution was moved into 50 mL centrifuge conicals after removing most of the leftover solids. The solution was centrifuged for 3 minutes at 7,000 rpm in a centrifuge (IEC Clinical Centrifuge, International Equipment Company, Chattanooga, TN, USA). The supernatant in the conicals were transferred into a 11 cm diameter cylindrical containers and containers were filled to a height of 5 cm.

6.2.3 Combined Collagen and Hydroxyapatite Freeze Casting

The collagen freeze casting solution is first made by dissolving the extracted collagen from demineralized porcine bone into 0.05 M acetic acid, making a 2 wt% collagen solution. Collagen is dissolved over a period of two days while being kept on ice and on a stir plate with a magnetic stir bar. The collagen pieces are also periodically stirred manually and larger collagen

pieces are cut using small surgical scissors or a scalpel create a smooth solution. After two days of dissolving into acetic acid, the solution is ready for freeze casting.

First the sintered magnetized HA scaffolds are placed back into the PVC mold in which the HA was originally freeze cast and placed on a copper coin. The edge between the PVC mold and copper coin are sealed with petroleum jelly. Then the 2 wt.% collagen-acetic acid solution is added to the mold using a 16G \times 1- $\frac{1}{2}$ syringe (BD PrecisionGlide Needle, Becton, Dickenson and Company, Franklin Lakes, NJ, USA). After the HA scaffold is covered by the solution, the mold is placed under a vacuum to allow the collagen solution to infiltrate the scaffold. This is done 2-3 times to after adding more collagen solution to ensure ample volume to be infiltrated.

After sufficient collagen solution infiltration, samples were freeze cast using the same rate as used for magnetic HA scaffolds, and were again freeze dried for two days. The combined scaffolds were then submerged in a cross-linking solution (as described in Divakar, et al. [118]) of 33 mM 1-ethyl-3-(3-dimethylaminopropyl) carbodiimide (EDC) and 6 mM N-hydroxysuccinimide (NHS) in ethanol for 24 hours. Scaffolds were then rinsed in deionized water for 1, 12, and 1 hour increments.

6.2.4 Material Characterization

Scanning electron microscopy (SEM) was used to observe the microstructure of the scaffolds. Collagen and HA scaffolds were dehydrated using a series of ethanol solutions from 100% water to 100% ethanol at 25% ethanol steps. Samples were then critically point dried in an Autosamdri-815 (Tousimis, Rockville, MD, USA) and then sputter coated with iridium using the Emitech K575X (Quorum Technologies Ltd, East Sussex, UK). Samples were imaged using a ZEISS Sigma 500 (Carl Zeiss AG, Oberkochen, Germany) with voltage range between 1 and 5 kV.

Fourier transform infrared spectroscopy (FTIR) was used to look at the location of collagen within the scaffold. An ATR Spectrum Two (PerkinELmer, Waltham, MA, USA) was used in absorbance mode in air with ~25 N of applied force on the samples. Before testing, background spectra were collected. Baselines for each spectrum were corrected in Igor Pro using a cubic spline fit [119].

Finally, thermogravimetric analysis (TGA) was performed to look at the weight percentage composition of collagen and hydroxyapatite in the scaffolds. Samples were heated from room temperature to 800°C at 10°C/min in a TGA instrument (Pyris 1, PerkinElmer, Waltham, MA, USA). According to [41], free and bound water is evaporated at 250°C, collagen decomposition and combustion take place from 250°C to 750°C, and the remaining mass after 750°C is hydroxyapatite.

6.2.5 Mechanical Testing

Samples were first cut to a size of 5×5×5 mm³ using a sectioning saw at least 1 cm from each of the ends of the scaffold to remove edge effects from the freeze casting process. Samples were tested under dry and hydrated conditions with phosphate buffered saline (PBS) solution. Four types of samples were tested with at least three samples each: pure magnetized HA, hydrated magnetized HA, dry collagen-HA scaffold, and hydrated collagen-HA scaffold. Samples were compressed under quasistatic conditions at a strain rate of 0.1% strain/sec.

6.3 Results and Discussion

6.3.1 Scaffold Characterization

Combined collagen and magnetized hydroxyapatite scaffolds were successfully created using this new synthesis method. Magnetic alignment of HA scaffolds was first evaluated using

SEM (shown in Figure 6.2a). The average alignment across three samples was 57% with a standard deviation of 16%, which is in the range of previous magnetic alignment values for 20 wt. % HA scaffolds [234]. A transverse cross-section of the combined collagen-HA scaffold is shown in Figure 6.2b. It can be seen that the lamellae in the combined scaffold is slightly larger than that of the magnetic HA scaffold with no collagen, where the lamellae thickness in the combined scaffold is $4 \pm 1 \mu\text{m}$ and the thickness of magnetic HA scaffold is $3 \pm 1 \mu\text{m}$. However, more measurements across a larger number of samples is likely needed to make a better comparison. Of note, the freeze casted collagen appears to adhere to the HA phase of the scaffold and does not seem to form its own smaller porosity. However, to confirm this, scaffolds should be imaged while samples are hydrated as done in Divakar, et al. [118] for collagen-only scaffolds.

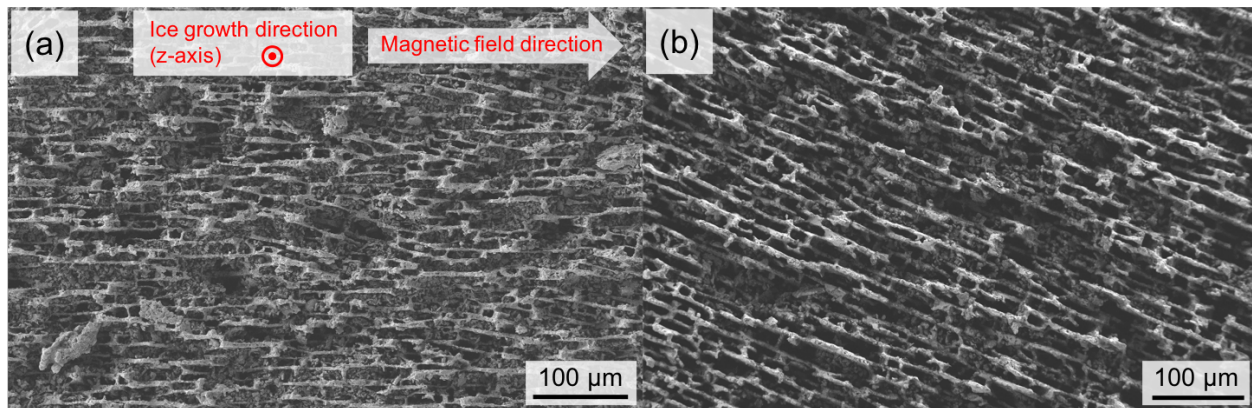


Figure 6.2. Scanning electron micrographs of the transverse cross-section of (a) magnetized HA and (b) combined collagen and magnetized HA scaffolds. Directions shown in (a) are applicable for both panels.

FTIR was used to look at chemical composition of the scaffold and the bonds that are present. Figure 6.3a shows FTIR spectra of demineralized bone and HCl-demineralized bone from Chapter 3 as well as the spectra for a magnetized HA scaffold. Bands associated with the mineral phase are dotted while bands for collagen are shown as dashed lines. Untreated bone has overlapping bands from both magnetized HA and demineralized bone, which is to be expected. Some differences in peaks, for example the presence of the OH^- band at 534 cm^{-1} and the less-

defined band at 1100 cm^{-1} , are also seen between untreated bone and pure HA, which is reasonable given that natural bone does not contain pure HA. It can be seen that most of the representative collagen bands are still present after demineralization and are more defined after mineral is removed from bone. This implies that most collagen structure is still preserved after the demineralization process.

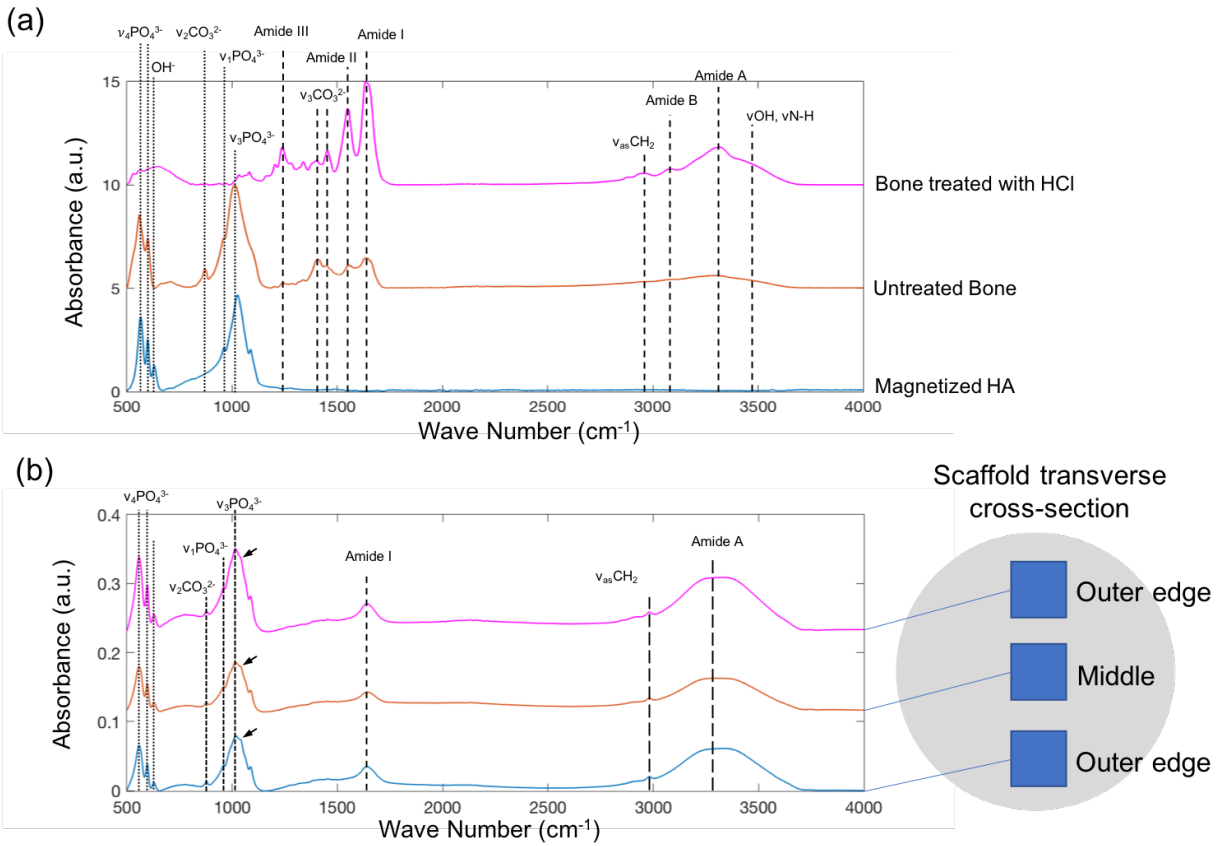


Figure 6.3. Fourier transform infrared spectra of **(a)** bone demineralized with HCl, untreated bone, and magnetized HA samples as well as **(b)** combined collagen and magnetized hydroxyapatite scaffolds in different regions of the scaffold transverse cross-section. Bands associated with hydroxyapatite are shown as dotted lines, and collagen-associated peaks are dashed. Arrows point at shoulder seen in combined scaffold spectra.

Figure 6.3b, shows the spectra of the combined collagen and HA scaffold. Three spectra are shown corresponding to two outer edges of the sample cross-section and the middle of the scaffold. This was done to assess whether collagen had successfully infiltrated the center of the

scaffold and it can be seen from Figure 6.3b that protein bands for amide I, amide A, and ν_{asCH_2} are present in all three spectra. Notably absent is the amide II band, which represents N-H bending and C-N stretching vibrations structure for collagen [138]. This band is sensitive to changes in conformation and collagen secondary structure [138], and has been shown to decrease in intensity due to EDC crosslinking. According to the cross-linking mechanism of EDC in collagen described by Yu, et al. [235], N-H₂ bonds in collagen are either eliminated or converted to N-H bonds, which may explain disappearance of the amide II band. This effect was also suggested in previous literature [236, 237]. Amide B is also significantly diminished and is related to N-H bonds as well. Finally, broadening of the amide A band is observed in the composite scaffold. Usha, et al. [238] observed this in EDC/NHS cross-linked collagen, and it was suggested that this phenomenon may be related to unusual strains or steric hindrances in the collagen after cross-linking.

Taking a closer look at representative HA bands, the $\nu_3\text{PO}_4^{3-}$ band has shifted and another peak has begun to emerge at 1018 cm^{-1} , which is pointed to by arrows in Figure 6.3b. This is likely the result of partial demineralization by acetic acid. The peaks at 1018 and 1040 cm^{-1} correspond to the $\nu_3\text{PO}_4$ from nonstoichiometric apatite and $\nu_3\text{PO}_4^{3-}$ band, respectively [132], showing that the HA has been partially dissolved by the acetic acid in the collagen solution. Future studies to produce combined collagen and HA scaffolds should substitute the collagen solvent for a compound that does not dissolve the HA scaffold.

Finally, TGA was performed to quantify the weight percentage of collagen that is present in the scaffolds. Results show that only ~0.26 wt.% collagen was present in the composite scaffold, 87.1 wt.% was mineral and ~12.6 wt. % was water from humidity. Better

homogenization of the collagen solution and longer infiltration times may be required to achieve a better ratio of collagen to HA.

6.3.2 Mechanical Testing in Dry and Hydrated Conditions

Two types of samples and two types of sample conditions were used during compression tests. Maximum stress results (Figure 6.4a) show that magnetized HA scaffolds were stronger compared to the collage-infiltrated scaffolds. This is likely due to the use of acetic acid as the solvent for the collagen solution. Although acetic acid is the most common method used to dissolve collagen to produce collagen gels [125, 239] and other scaffolds [240, 241], it is also an organic acid that dissolves hydroxyapatite [242]. It is likely that this caused the hydroxyapatite scaffold to be weakened and therefore, have a lower strength. The effect of dissolved hydroxyapatite by acetic acid is also visible in results for Young's modulus (Figure 6.4b) as the combined scaffold clearly not as stiff as the magnetized HA scaffolds. A way to address this issue in the future is to try dissolving the collagen in water instead, which should keep the hydroxyapatite stable. This has been done in Villa, et al. [230], and it is implied in Divakar, et al. [118] that if the collagen scaffold is not cross-linked prior to rehydration, the scaffold would collapse and dissolve.

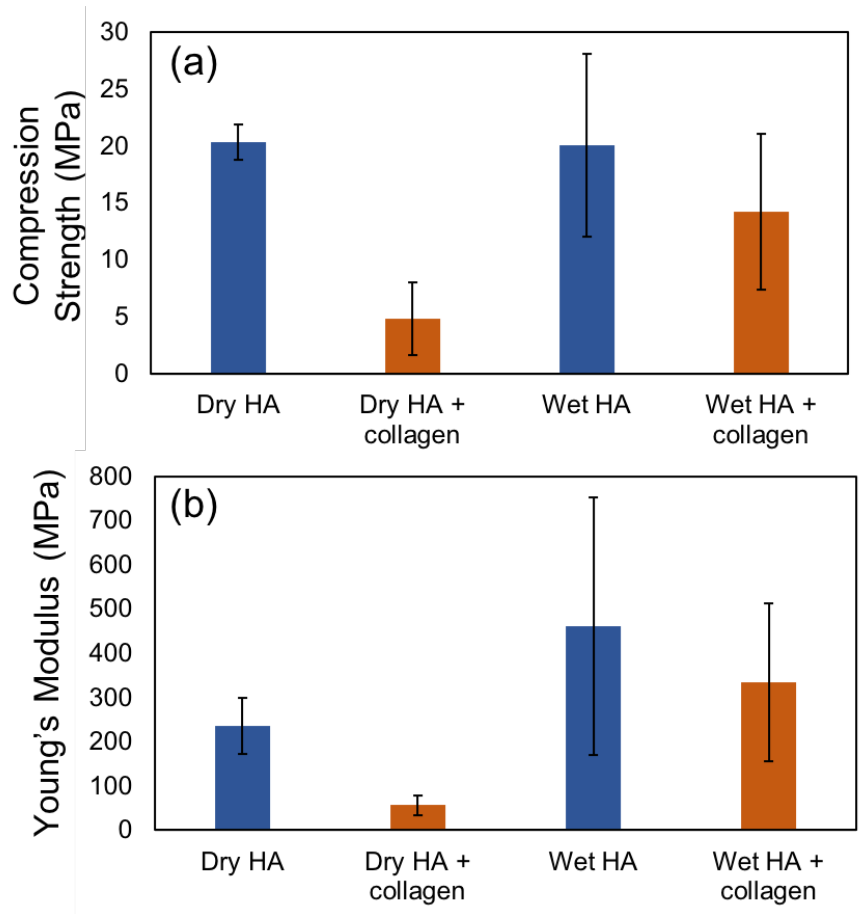


Figure 6.4. (a) Compression strength of scaffolds under dry or hydrated conditions and **(b)** Young's modulus of scaffolds in dry and hydrated conditions. Error bars show standard deviation and n=3.

Having looked at the differences between mechanical properties of the two types of scaffold, the effect of hydration using PBS will now be discussed. Magnetized HA scaffolds show no change in strength after hydration, but show larger variation in strength. Strength of the combined collagen-HA scaffold show significant improvement. For Young's modulus, variation also increases for magnetized HA scaffolds, but there seems to be no significant difference. Meanwhile, for the combined collagen-HA scaffold, hydrated scaffolds show a marked increase in stiffness. Swelling of the collagen phase may fill empty pores within the combined scaffold, thereby increasing the overall stiffness of the composite.

6.4 Conclusions

This paper describes the synthesis of a combined collagen and hydroxyapatite scaffold for the first time. This was done through a two-step process where magnetized HA particles were first magnetically freeze cast to create two axes of alignment in the y - and z -axes. Then a collagen solution extracted from demineralized bone is infiltrated into the hydroxyapatite scaffold and freeze cast again. Important findings include:

- Alignment of HA from the magnetic field is comparable to previous work and the infiltrated collagen phase appears to adhere to the HA scaffold rather than forming its own porosity within the HA scaffold.
- FTIR shows that collagen is present throughout the scaffold and that the use of acetic acid as the solvent for collagen results in partial dissolving of the base magnetic HA scaffold. Additionally, cross-linking by EDC and NHS results in significant changes in collagen secondary structure.
- Mechanical testing shows that acetic acid from the collagen solution significantly weakens the combined collagen-HA scaffolds when compared with pure magnetized HA scaffolds.
- Finally, hydration using phosphate buffered saline solution affects the mechanical properties of the combined scaffold, making the scaffold both stronger and stiffer while the magnetic HA scaffolds did not see much benefit from hydration.

Chapter 6, in part, is in preparation for submission for publication as “Freeze Cast Composite of Hydroxyapatite and Demineralized Bone,” 2018. The dissertation author is the primary investigator and author on this paper. This work is co-authored by Gowri Viswanathan, Justin Salim, and Katherine Tang, and Joanna McKittrick.

7 Recommendations for Future Work

7.1 Age study for mineral content of young porcine bone

Deproteinization of porcine bone has shown that bone is an interpenetrating composite at 6 months. However, it is generally agreed upon that bone starts out as a collagen matrix that mineralizes as bone develops [243, 244]. Therefore, it would be worth investigating when in development bone transitions from collagen matrix, to collagen with mineral particles, and finally to an interpenetrating composite with a continuous hydroxyapatite phase. Some preliminary experiments have been done in the group by demineralizing 3-week-old porcine bone, however even at this age, the bone is already continuous. Taking this into account, it would be worth investigating bones in fetal pigs to determine when the mineral phase in bone becomes continuous. This can be done by deproteinization of porcine fetuses at different stages of development. When the deproteinized bone no longer stays as one continuous solid and breaks down into small particles after deproteinization, this should indicate the age at which the bone has yet to form a continuous mineral network. After determining the age before which bone has a continuous mineral phase, it would then be worth comparing the mechanical behavior and properties of bone before and after a continuous mineral phase has developed. Based on the findings in this dissertation, it is likely we would see large differences in mechanical behavior.

7.2 Measurement of nanoscale deformation using *in situ* small angle x-ray scattering and wide angle x-ray diffraction

Having determined the best methods for deproteinization and demineralization of bone with as little influence on the mineral or collagen phases after each treatment type as discussed in Chapters 2 and 3, the new area to explore would be the nanoscale deformations of each individual phase. A technique that can be used is small angle x-ray scattering (SAXS) and wide

angle x-ray diffraction (WAXD) to observe deformation of collagen and hydroxyapatite, respectively. SAXS can be used to look at the change in characteristic d-spacing in a collagen fibril and WAXD looks at the change in interplanar spacing in hydroxyapatite crystals and usually looks at the c-axis length since the c-axis is aligned in the direction of compression in most bone [245].

Studies have been done to look at nanoscale deformation in tension and in compression of bone as a composite and one of the most impressive aspects of this technique is the ability to measure both phases at once while also measuring macroscale stress. However, it would be just as interesting and important to measure nanoscale deformation each of the phases separately to help understand the role of nanostructure of each phase in the overall composite. By removing each phase while maintaining the nano- and microstructure of the phase left behind, deformations at the nanoscale of either the mineral or collagen phase can be observed. This can provide more insight into the function of each phase individually, and could help inform future modeling of bone mechanics.

7.3 Cell growth study using scaffolds synthesized with the combine collagen and hydroxyapatite freeze casting

Chapter 6 details a new method for synthesizing a bone-inspired scaffold by freeze casting both hydroxyapatite and collagen into a porous biomaterial. The next step after observing the material properties of the composite is to test the biocompatibility of the scaffold and whether the composite has added benefits for bone growth. While it is unlikely for the material to be detrimental to cell growth since HA is naturally produced in the body and the collagen crosslinking technique used has been shown to be biocompatible [118, 241], MTT cytotoxicity test should be done to make sure cell death is not an issue. A multi-week comparison study

should also be done to see how cells respond to pure HA scaffolds as opposed to scaffolds with both collagen and HA.

Previous studies have shown that osteocytes can sense stresses within bone and grow in response to applied loads within the bone []. This is why astronauts need to do exercises to simulate normal bone loads while in zero-gravity conditions. Therefore, an additional test that would be valuable is to seed the scaffolds with osteocytes and load the bioinspired composite in cyclical compressive loading within the elastic regime of the material. The study should then determine the effect of the composite on bone cell growth during which cyclical loading takes place. This could help prove that the new composite material would be a viable bone substitute, reducing the need for autografts.

7.4 Effects of bioinspired hierarchy and anisotropy in additively manufactured composites

With respect to bioinspired materials, additive manufacturing has emerged as an easy way to prototype and test bioinspired designs. Most papers have focused on a testing the importance of a single level of hierarchy. The next step would be to investigate incorporating multiple levels of hierarchy and see how lower levels effect overall properties of a composite. For example, results from Chapter 4 are arrangements of some proposed nanostructures for the collagen and hydroxyapatite phases in bone. Incorporating these as a lower level structure and adding higher levels of bone hierarchy can help elucidate the effect of the nanostructure on overall mechanical behavior including strength, toughness, fracture toughness, and impact resistance.

Another aspect that can be explored is the introduction of anisotropy into the unit cells. Instead of using cubic cells, elongated rectangular prisms can be used to explore the effects of

anisotropy on mechanical properties in different directions. This has been done for polymer foams[246], and would help us to build better models and address some of the limitations in current predictions of composite strength and modulus using modeling.

8 Conclusion

In this dissertation, the phases of bone were first isolated using deproteinization or demineralization to show that bone was an interpenetrating composite. The best method for deproteinization that preserves the mineral phase of bone was explored in Chapter 2. A 0.35 M NaOCl solution was found to remove the most protein from bone while leaving the mineral phase intact. Thermogravimetric analysis results showed that the H₂O₂ solution removed minimal protein, and that both NaOH and KOH solutions were found to dissolve bone mineral during treatment while removing small quantities of protein only. NaOCl treatment also had the most similar mineral microstructure to that seen in untreated bone as well. Conversely, NaOH and KOH treatments showed large platelets, which are likely the result of dissolved and reprecipitated hydroxyapatite. X-ray diffraction (XRD) was used for the first time to compare deproteinization treatments and showed almost no changes to the mineral composition and structure after treatment. XRD of whole bone also showed directional dependence from oriented crystals and revealed previously unobserved peaks from other forms of apatite. Finally, Raman spectroscopy revealed that small quantities of protein were still present in NaOCl-treated specimens after 14 days of treatment and that the addition of a delipidation step had almost no effect on residual protein content. Results from this study not only reveal the best deproteinization treatment, but also show that deprotenized bone is self-standing and that bone is likely an interpenetrating composite.

On the front of demineralization, of the four treatments tested: EDTA, CH₂O₂, HCl, and an EDTA/HCl mixture, CH₂O₂ was found to have the best demineralization capability while preserving collagen integrity. Collagen integrity was found to be similar across all treatments

with the exception of the EDTA/HCl mixture, which had poorer quality collagen. CH_2O_2 showed better collagen quality from Raman spectroscopy analysis, however, TGA showed that the whole volume of bone was not completely demineralized. FTIR revealed that collagen secondary structure was altered among all treatments, and SEM showed aligned collagen fibrils in samples after treatment. The deciding factor in the “best” demineralization treatment was therefore the length of the treatment require to completely demineralize bone, making HCl the best method.

After the phase isolation studies done in this dissertation showed that bone was an interpenetrating composite, the influence of architecture of a material on mechanical properties was investigated. Three types of composites were 3D printed and their mechanical behavior compared: discontinuous phase composites (DPC), matrix-inclusion composites (MIC), and interpenetrating phase composites (IPC). Results showed that both increasing the number of unit cells with constant specimen size and decreasing the size of unit cells generally decreased both strength and elastic modulus. Finite element modeling showed similar behavior to $1 \times 1 \times 1$ unit cells with 12.7 mm side lengths, but had higher modulus and strength predictions than observed in experiments. As observed from previous studies, strain is predominantly in the soft phase and localization in strain was observed to lead to overall material instability. Finally, smaller sized unit cells showed softening and weakened mechanical properties, which are the opposite of most traditional material trends.

In the last experimental chapters of this dissertation, bioinspired materials were synthesized. The first was a novel radial-concentric freeze cast scaffold with three layers was inspired by the porcupine fish spine, which also has an interpenetrating structure and has the same composition of bone. Radial-concentric freeze cast porous ceramics were compared with samples freeze cast through radial and conventional freeze cast methods. The porcupine fish

spine inspired scaffolds had axial compressive strengths similar to those of conventional and radial freeze cast scaffolds, and when infiltrated with epoxy, radial-concentric freeze casted ceramics had significantly improved axial compressive modulus over uninfiltrated radial-concentric freeze casts. With infiltration, radial-concentric freeze casts improved significantly to having the highest splitting tensile strength. Therefore, the radial-concentric samples can be considered to have optimal mechanical properties once infiltrated. Results help show that structure plays a significant role in multi-phase materials and can be used for improved design of engineering materials.

The second bioinspired material is a bone inspired scaffold made from magnetized hydroxyapatite (HA) and collagen made for the synthesized for the first time through freeze casting. Results showed that collagen was sufficiently infiltrated into the HA scaffold. While the acetic acid used for the collagen solution was found to degrade the HA scaffold, hydration of the scaffolds was found to increase both stiffness and strength of the composite HA-collagen scaffold. This new scaffold has potential for use as a bone replacement scaffold and sheds light on hydration effects within biological materials.

The findings of this dissertation not only show that the nanostructure of bone is an interpenetrating composite, it also helps to prove the importance of an interpenetrating structure and continuous stiff phase for maintaining stiffness and strength in composites. The composites designed and synthesized based off of these principles show that the architecture of a material is essential for desirable mechanical properties. In addition, these new composites show that the inclusion of a reinforcing phase improves mechanical properties significantly. These conclusions build on what is known about composite properties, and can help aid the design of new, lightweight materials for engineering applications. Bioinspiration has proved to be a useful way

to explore new composite designs and further studies must be conducted to fully connect mechanical properties to material architecture.

APPENDIX

Appendix A. Supplementary Material for Deproteinization of Cortical Bone

pH Measurement and Ionic Strength Calculations of Treatment Solutions

Treatment solution pH was measured using narrow range pH paper and data are shown in Table 2.1. Ionic strength was calculated using Equation A.1 for NaOH and KOH solutions, where I is the ionic strength, c_i is the molar concentration of the ion, and z_i is the charge for each ion i present in the solution. H₂O₂ and NaOCl treatment ionic strengths were excluded due to both having multiple dissociation or decomposition reactions that are not simple to deconvolute.

$$I = \frac{1}{2} \sum_{i=1}^n c_i z_i^2 \quad \text{Equation A.1}$$

Rietveld Refinement

Rietveld refinement was performed using TOPAS with hexagonal symmetry (space group: P6₃/m). Refinements were obtained by refining the unit-cell axes ($a=b$ and c), zero point, and background coefficients. Thermal factors were kept constant and microstrain was set to zero, since previous studies have found the effect to be minimal [81]. Results from refinement are shown in Table A.1.

Table A.1. Lattice parameters a and c calculated through Rietveld refinement as well as c/a ratio. Goodness of fit for each refinement is as also shown. Estimated standard deviations are shown in parentheses for the last two significant figures.

Sample/treatment	a (nm)	c (nm)	c/a	Goodness of fit (χ^2)
Untreated	9.440 (30)	6.905 (16)	0.731	1.02
NaOCl	9.434 (10)	6.9067 (64)	0.732	1.15
H ₂ O ₂	9.482 (23)	6.9191 (84)	0.730	1.02
NaOH	9.395 (14)	6.8951 (88)	0.734	1.00
KOH	9.420 (13)	6.8970 (80)	0.732	1.05
Synthetic hydroxyapatite	9.419	6.883	0.731	-

Determining Crystallite Size with the Scherrer Equation

Analysis of hydroxyapatite crystallite size was performed in DIFFRAC.EVA software, which uses the Scherrer equation. It is known that crystals in bone can be either plate-like or needle-like in morphology, therefore crystallite sizes along the c axis (τ_c) and a,b axes ($\tau_{a,b}$) were calculated using the full-width at half-maximum (FWHM) of the (002) and (310) peaks, respectively. A Scherrer constant (K) value of 0.9 was used based on work by Johnsson, et al. [81]. Since the (300) peak could not be clearly distinguished from neighboring peaks, the (310) peak was used to approximate $\tau_{a,b}$. The approximated value using the (310) peak may underestimate the actual crystallite size of in the a -axis direction since the interplanar spacing is smaller than that of the (300) plane. Results for crystallite size are summarized in Table A.2.

Table A.2. Crystallite sizes along the c and a,b axes for different treatments.

Sample/treatment	Crystallite Size (nm)	
	τ_c	$\tau_{a,b}$
Untreated	33.67	16.38
H ₂ O ₂	18.95	10.45
NaOCl	26.06	8.61
NaOH	20.03	8.26
KOH	19.77	9.49

Appendix B. Collagen Scaffold Production using Demineralized Bone and Freeze Casting

Six-month-old porcine femur bone was cut into quadrants. The quadrants were then cut into slices of 2 mm thickness using a diamond blade sectioning saw. The bone was demineralized according to the protocol for HCl mentioned in the sample preparation section. After demineralization, the collagen from demineralized bone was extracted using a process similar to that described in Rajan, et al. [125]. Demineralized bone was placed in pure acetone for 10 min, and then transferred to 70% isopropanol solution for an additional 10 min. The treated bone was then placed in a beaker of 0.05 M acetic acid solution for two days on ice. The acetic acid should be added so that the bone samples are covered and with about 1 cm above the demineralized bone pieces and a magnetic stir bar was added to the beaker. The beaker was then placed in a Styrofoam container with ice and placed on a magnetic stirrer for 24 hrs. Ice was switched out ever 9-12 hours. After the first day of mixing, the solution with demineralized bone was blended using an immersion blender to break up the pieces of demineralized bone. The solution was then returned the stir plate for another 24 hours on ice.

After 48 hours total of stirring, the liquid portion of the mixture was transferred to 50 mL conical centrifuge tubes. Tubes were centrifuged for 2 min at 7,000 RPM to remove larger pieces of collagen that weren't properly dissolved. The supernatant in the centrifuge tubes were then transferred to an 11 mm diameter plastic container and filled to a liquid height of 5 mm from the base of the container and placed in a freezer for at least 6 hours. After the collagen/acetic acid solution is frozen, the ice is punctured and placed into a lyophilizer (Labconco, Kansas City, MO, USA) for at least 48 hours to produce a collagen sponge. The ice is punctured so that any trapped air under the frozen solution cannot expand in vacuum of the lyophilizer.

To freeze cast collagen, the collagen sponge is weighed and dissolved in 0.05 M acetic acid solution to make a 2 wt% collagen solution similar to what was done by Divakar, et al. [118]. The collagen solution was degassed and placed in a polyvinyl chloride (PVC) mold to be freeze cast at a cooling rate of $-10^{\circ}\text{C}/\text{min}$. After freezing, the scaffold was lyophilized for 48 hours and then placed in a crosslinking solution of 33 mM 1-Ethyl-3-(3-dimethylaminopropyl)-carbodiimide

(EDC), 6 mM N-hydroxysuccinimide (NHS), and ethanol for 24 hours. The scaffold was rinsed five times after crosslinking with deionized water for five minutes each rinse. To dry the collagen scaffold, the same sample preparation as described for Raman spectroscopy samples was used.

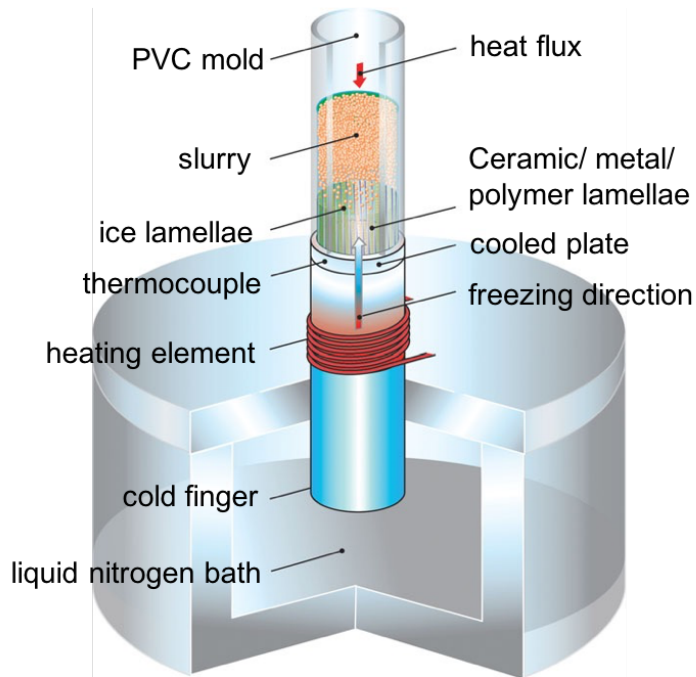


Figure B.1. Freeze casting experimental setup adapted from Wegst, et al. [9].

**Supplementary Material for Additively Manufactured Two Phase Composites with
Continuous or Discontinuous Phases**

Table C.1. Yield strain, yield stress, and elastic modulus values from FEM and experiments. Values for experiments are given as average (s.d) and n=6 for each sample type.

Network type	Condition	Sample type	Yield Strain (%)	Yield Stress (MPa)	Elastic Modulus (MPa)	
DPC	FEM MBC	1×1×1	-	-	7.79	
	FEM MBC	2×2×2	-	-	7.98	
	FEM PBC	-	-	-	8.02	
	Experiment		1×1×1	3.3 (0.4)	0.78 (0.05)	27.9 (1.7)
			2×2×2	7.9 (0.3)	1.87 (0.12)	25.67 (0.9)
			4×4×4	15.6 (0.4)	4.51 (0.18)	28.7 (0.8)
			8×8×8	32.9 (0.8)	11.4 (0.4)	34.4 (0.8)
MIC soft frame	FEM MBC	1×1×1	-	-	29.60	
	FEM MBC	2×2×2	-	-	27.80	
	FEM PBC	-	-	-	27.80	
	Experiment		1×1×1	17.3 (0.4)	33.3 (0.6)	26 (2)
			2×2×2	13.5 (0.2)	7.6 (1.1)	24.5 (0.9)
			4×4×4	10.6 (0.6)	3.2 (0.3)	23.1 (1.5)
			8×8×8	13.4 (0.5)	2.3 (0.1)	20.8 (0.8)
MIC stiff frame	FEM MBC	1×1×1	5.5	25.88	507.7	
	FEM MBC	2×2×2	6	27.5	509.8	
	FEM PBC	-	6.7	29.87	514.3	
	Experiment		1×1×1	5.54 (0.12)	13.7 (0.4)	346 (15)
			2×2×2	5.35 (0.12)	13.2 (0.7)	338 (12)
			4×4×4	5.45 (0.10)	13.7 (0.2)	363 (11)
			8×8×8	5.9 (0.2)	11.2 (0.2)	296 (8)
IPC soft frame	FEM MBC	1×1×1	5.1	20.5	403.8	
	FEM MBC	2×2×2	5	19.8	403.8	
	FEM PBC	-	5.5	20	403	
	Experiment		1×1×1	4.9 (0.3)	17.2 (1.0)	472 (26)
			2×2×2	4.31 (0.15)	14.5 (0.4)	439 (8)
			4×4×4	8.20 (0.16)	16.0 (0.3)	369 (9)
			8×8×8	6.4 (0.3)	13.7 (0.4)	309 (8)
IPC stiff frame	FEM MBC	1×1×1	5.5	18.42	379	
	FEM MBC	2×2×2	6	20	398.1	
	FEM PBC	-	5.5	18.94	370.2	
	Experiment		1×1×1	5.09 (0.12)	12.4 (0.3)	341 (7)
			2×2×2	5.36 (0.14)	12.04 (0.14)	323 (8)
			4×4×4	5.5 (0.1)	12.1 (0.2)	312 (4)
			8×8×8	6.7 (0.4)	11.0 (0.3)	260 (7)

Average stress-strain curves for single unit cells of the different composite types discussed in this paper are shown in Figure C.1.

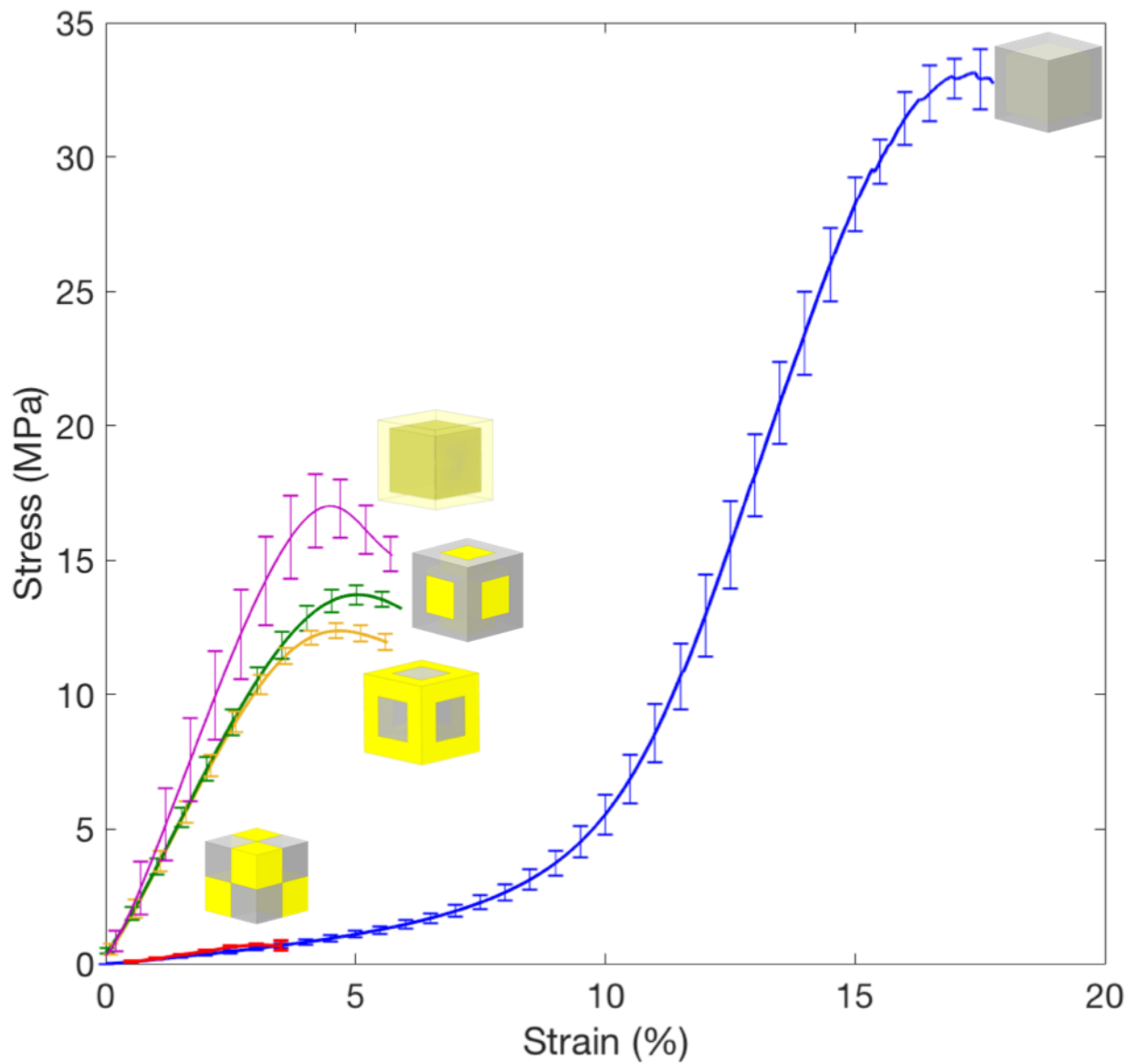


Figure C.1. Average stress-strain curves of composite unit cells.

Appendix C. Supplementary Material for Radial-Concentric Freeze Casting

Statistical Analysis Based on Structure and Infiltration

Table D.1. Summary of mechanical test results, where N is the number of samples and SD is the standard deviation.

	Axial Compressive Strength Sample type	N	Mean ± SD (MPa)
Infiltrated	Radial	7	210 ± 40
	Radial-concentric	6	200 ± 30
	Conventional	5	177 ± 17
Uninfiltrated	Radial-concentric	5	7 ± 2
	Radial	6	7.0 ± 1.3
	Conventional	8	6.5 ± 1.6
	Axial Compressive Modulus Sample type		
Infiltrated	Radial-concentric	6	4600 ± 500
	Radial	7	4100 ± 800
	Conventional	5	3000 ± 400
Uninfiltrated	Concentric	6	400 ± 200
	Radial	8	290 ± 150
	Conventional	5	100 ± 40
	Splitting Tensile Strength Sample type		
Infiltrated	Radial-concentric	6	17 ± 2
	Conventional	5	15.4 ± 1.5
	Radial	7	10.8 ± 1.9
Uninfiltrated	Radial	6	0.9 ± 0.3
	Radial-concentric	5	0.212 ± 0.06
	Conventional	8	0.19 ± 0.08

Variances were analyzed using a linear model and summarized in Table D.2.

Table D.2. Analysis of variance, p-values (where $p < 0.05$ indicates that the mechanical property is influenced by the source).

Source	Stiffness	Strength	Tensile Splitting Strength	Maximum Strain
Structure	0.001	0.277	0.000	0.004
Infiltration	0.000	0.000	0.000	0.054
Structure \times Infiltration	0.000	0.320	0.0000	0.000

Unintended Melting in Radial-concentric Freeze Casting

Figure D.1 below shows a radial-concentric sample in which temperatures between the frozen solid and the liquid slurry were not equilibrated in the second step of the radial-concentric freeze casting method.

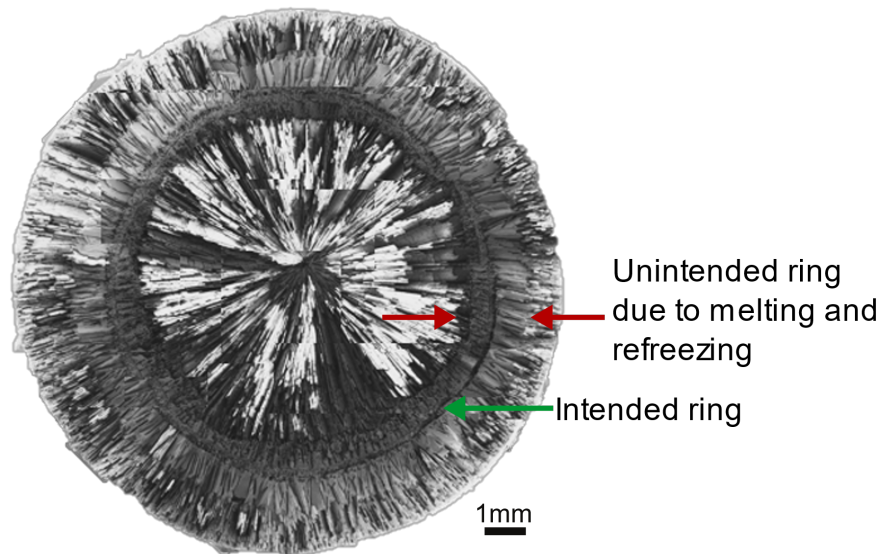


Figure D.1. Scanning electron micrograph of radial-concentric sample manufactured without equilibrating temperatures of the frozen solid and liquid slurry. Unintended rings from melting and refreezing are indicated by red arrows.

Appendix D. Magnetizing Hydroxyapatite and Freeze Casting Protocol

HA particles of ~ 2 μm diameter (Trans Tech, Adamstown, MD, USA) are first magnetized with iron oxide particles similar to the methods described in [7, 234]. In a 200 mL bottle, 1.97 g of HA particles are added to 75 mL of distilled water. The bottle is placed in a sonicator and swirled while 100 μL of anionic ferrofluid (EMG-605, Ferrotec, Bedford, NH, USA) is added to the HA particles in water. Continue swirling the container for ~ 10 s, after which the particles in the water will become a light brown color as the magnetite particles attach to the HA particles. Magnetized HA was then rinsed with distilled water as described in and dried for at least 6 hours at 100°C in a drying oven.

To prepare the magnetized slurry, magnetized HA particles (10 and 20 vol%) were mixed with the following wt% quantities of binders and dispersants: 1 wt% polyvinyl alcohol (PVA 100,000 g/mol molecular weight (MW), Alfa Aesar, Ward Hill, MA, USA), 1 wt% polyethylene glycol (PEG, 10,000 g/mol MW, Alfa Aesar, Ward Hill, MA, USA), and 1 wt% Darvan 811 (R.T. Vanderbilt Company, Inc., Norwalk, CT, USA). The slurry was added to a container with alumina grinding media and ball milled for 24 hours.

After ball milling, the slurry was separated from the alumina grinding media and placed in a PVC mold. The PVC mold is placed between two ~ 420 mT bar magnets (N52 grade, K&J Magnetics, Inc. Pipersville, PA, USA) with a separation distance of 9.9 cm so that the magnetic field is ~ 25 mT according to the fitting curve in the Supplementary Material of [7]. The slurry was then freeze cast using a freezing rate of $-10^\circ\text{C}/\text{min}$ down to -170°C . After freeze casting, samples were freeze dried (Labconco, Kansas City, MO, USA) for two days at -50°C and a vacuum pressure of 3.5×10^{-6} Pa. Samples were sintered in an open-air furnace for three hours at 1300°C , with heating and cooling rates of $2^\circ\text{C}/\text{minute}$.

REFERENCES

1. Fratzl, P. and Weinkamer, R., "Nature's hierarchical materials," *Progress in Materials Science*, **52**(8): p. 1263-1334 (2007).
2. Naleway, S.E., Porter, M.M., McKittrick, J., and Meyers, M.A., "Structural design elements in biological materials: Application to bioinspiration," *Advanced Materials*, **27**(37): p. 5455-5476 (2015).
3. Yaraghi, N.A., Guarín-Zapata, N., Grunenfelder, L.K., Hintsala, E., Bhowmick, S., Hiller, J.M., Betts, M., Principe, E.L., Jung, J.-Y., Sheppard, L., Wuhrer, R., McKittrick, J., Zavattieri, P.D., and Kisailus, D., "A sinusoidally architected helicoidal biocomposite," *Advanced Materials*, **28**(32): p. 6835-6844 (2016).
4. Launey, M.E., Buehler, M.J., and Ritchie, R.O., "On the mechanistic origins of toughness in bone," *Annual Review of Materials Research*, **40**: p. 25-53 (2010).
5. Fish, F.E., Weber, P.W., Murray, M.M., and Howle, L.E., "The tubercles on humpback whales' flippers: application of bio-inspired technology," *Integrative and Comparative Biology*, **51**(1): p. 203-213 (2011).
6. Deville, S., Saiz, E., and Tomsia, A.P., "Freeze casting of hydroxyapatite scaffolds for bone tissue engineering," *Biomaterials*, **27**(32): p. 5480-5489 (2006).
7. Frank, M.B., Naleway, S.E., Haroush, T., Liu, C.-H., Siu, S.H., Ng, J., Torres, I., Ismail, A., Karandikar, K., and Porter, M.M., "Stiff, porous scaffolds from magnetized alumina particles aligned by magnetic freeze casting," *Materials Science and Engineering: C*, **77**: p. 484-492 (2017).
8. Naleway, S.E., Christopher, F.Y., Hsiong, R.L., Sengupta, A., Iovine, P.M., Hildebrand, J.A., Meyers, M.A., and McKittrick, J., "Bioinspired intrinsic control of freeze cast composites: Harnessing hydrophobic hydration and clathrate hydrates," *Acta Materialia*, **114**: p. 67-79 (2016).
9. Wegst, U.G., Schechter, M., Donius, A.E., and Hunger, P.M., "Biomaterials by freeze casting," *Philosophical Transactions. Series A, Mathematical, Physical, and Engineering Sciences*, **368**(1917): p. 2099-2121 (2010).
10. Munch, E., Launey, M.E., Alsem, D.H., Saiz, E., Tomsia, A.P., and Ritchie, R.O., "Tough, bio-inspired hybrid materials," *Science*, **322**(5907): p. 1516 (2008).
11. Bai, H., Walsh, F., Gludovatz, B., Delattre, B., Huang, C., Chen, Y., Tomsia, A.P., and Ritchie, R.O., "Bioinspired hydroxyapatite/poly(methyl methacrylate) composite with a

- nacre-mimetic architecture by a bidirectional freezing method," *Advanced Materials*, **28**(1): p. 50-56 (2016).
12. Porter, M.M., Meraz, L., Calderon, A., Choi, H., Chouhan, A., Wang, L., Meyers, M.A., and McKittrick, J., "Torsional properties of helix-reinforced composites fabricated by magnetic freeze casting," *Composite Structures*, **119**: p. 174-184 (2015).
 13. Launey, M.E., Munch, E., Alsem, D.H., Saiz, E., Tomsia, A.P., and Ritchie, R.O., "A novel biomimetic approach to the design of high-performance ceramic-metal composites," *Journal of The Royal Society Interface*, **7**(46): p. 741 (2010).
 14. Porter, M.M., McKittrick, J., and Meyers, M.A., "Biomimetic materials by freeze casting," *JOM*, **65**(6): p. 720-727 (2013).
 15. Valashani, S.M.M. and Barthelat, F., "A laser-engraved glass duplicating the structure, mechanics and performance of natural nacre," *Bioinspiration & Biomimetics*, **10**(2)(2015).
 16. Yin, Z., Dastjerdi, A., and Barthelat, F., "Tough and deformable glasses with bioinspired cross-ply architectures," *Acta Biomaterialia*, **75**: p. 439-450 (2018).
 17. Malik, I.A. and Barthelat, F., "Toughening of thin ceramic plates using bioinspired surface patterns," *International Journal of Solids and Structures*, **97-98**: p. 389-399 (2016).
 18. Velasco-Hogan, A., Xu, J., and Meyers, M.A., "Additive manufacturing as a method to design and optimize bioinspired structures," *Advanced Materials*, **0**(0): p. 1800940.
 19. Sullivan, T., *Avian Feathers: An Examination of Lightweight Resilience and Bioinspired Designs*. 2017, UC San Diego.
 20. Porter, M.M., Adriaens, D., Hatton, R.L., Meyers, M.A., and McKittrick, J., "Why the seahorse tail is square," *Science*, **349**(6243)(2015).
 21. Porter, M.M., *Bioinspired Design: Magnetic Freeze Casting*. 2014, UC San Diego.
 22. Weiner, S. and Wagner, H.D., "The material bone: Structure mechanical function relations," *Annual Review of Materials Science*, **28**: p. 271-298 (1998).
 23. Ritchie, R.O., "The conflicts between strength and toughness," *Nature Materials*, **10**(11): p. 817-822 (2011).

24. Olszta, M.J., Cheng, X.G., Jee, S.S., Kumar, R., Kim, Y.Y., Kaufman, M.J., Douglas, E.P., and Gower, L.B., "Bone structure and formation: A new perspective," *Materials Science & Engineering R-Reports*, **58**(3-5): p. 77-116 (2007).
25. Goldberg, M. and Boskey, A.L., "Lipids and biomineralizations," *Progress in Histochemistry and Cytochemistry*, **31**(2): p. III1-X187 (1996).
26. Boskey, A.L., *Bone mineralization*, in *Bone Mechanics Handbook*, S.C. Cowin, Editor. 2001, CRC Press: Boca Raton, FL. p. 5.1-5.33.
27. Baselt, D.R., Revel, J.P., and Baldeschwieler, J.D., "Subfibrillar structure of type-I collagen observed by atomic-force microscopy," *Biophysical Journal*, **65**(6): p. 2644-2655 (1993).
28. Fratzl, P., *Collagen: Structure and Mechanics*. 2008, New York, NY: Springer. 506 pages.
29. Wegst, U.G., Bai, H., Saiz, E., Tomsia, A.P., and Ritchie, R.O., "Bioinspired structural materials," *Nature Materials*, **14**(1): p. 23-36 (2015).
30. Landis, W.J., Song, M.J., Leith, A., Mcewen, L., and Mcewen, B.F., "Mineral and organic matrix interaction in normally calcifying tendon visualized in 3 dimensions by high-voltage electron-microscopic tomography and graphic image-reconstruction," *Journal of Structural Biology*, **110**(1): p. 39-54 (1993).
31. Currey, J.D., *Bones: Structure and Mechanics*. 2002, Princeton: Princeton University Press.
32. Barkaoui, A., Bettamer, A., and Hambli, R., "Failure of mineralized collagen microfibrils using finite element simulation coupled to mechanical quasi-brittle damage," *Procedia Engineering*, **10**: p. 3185-3190 (2011).
33. Barkaoui, A., Bettamer, A., and Hambli, R., "Mechanical behavior of single mineralized collagen fibril using finite element simulation coupled to quasi-brittle damage law," *6th European Congress on Computational Methods in Applied Sciences and Engineering*: p. 1357-1365 (2012).
34. Barkaoui, A. and Hambli, R., "Nanomechanical properties of mineralised collagen microfibrils based on finite elements method: biomechanical role of cross-links," *Computer Methods in Biomechanics and Biomedical Engineering*, **17**(14): p. 1590-1601 (2014).

35. Barkaoui, A., Hambli, R., and Tavares, J.M.R.S., "Effect of material and structural factors on fracture behaviour of mineralised collagen microfibril using finite element simulation," *Computer Methods in Biomechanics and Biomedical Engineering*, **18**(11): p. 1181-1190 (2015).
36. Schwarcz, H.P., "The ultrastructure of bone as revealed in electron microscopy of ion-milled sections," *Seminars in Cell & Developmental Biology*, **46**: p. 44-50 (2015).
37. Benezra Rosen, V., Hobbs, L., and Spector, M., "The ultrastructure of anorganic bovine bone and selected synthetic hydroxyapatites used as bone graft substitute materials," *Biomaterials*, **23**(3): p. 921-928 (2002).
38. Chen, P.-Y., Toroian, D., Price, P.A., and McKittrick, J., "Minerals form a continuum phase in mature cancellous bone," *Calcified Tissue International*, **88**(5): p. 351-361 (2011).
39. Chen, P.Y. and McKittrick, J., "Compressive mechanical properties of demineralized and deproteinized cancellous bone," *Journal of the Mechanical Behavior of Biomedical Materials*, **4**(7): p. 961-973 (2011).
40. Novitskaya, E., Chen, P.Y., Lee, S., Castro-Cesena, A., Hirata, G., Lubarda, V.A., and McKittrick, J., "Anisotropy in the compressive mechanical properties of bovine cortical bone and the mineral and protein constituents," *Acta Biomaterialia*, **7**(8): p. 3170-3177 (2011).
41. Bigi, A., Ripamonti, A., Cojazzi, G., Pizzuto, G., Roveri, N., and Koch, M.H.J., "Structural analysis of turkey tendon collagen upon removal of the inorganic phase," *International Journal of Biological Macromolecules*, **13**(2): p. 110-114 (1991).
42. Venkatesan, J., Qian, Z.J., Ryu, B., Thomas, N.V., and Kim, S.K., "A comparative study of thermal calcination and an alkaline hydrolysis method in the isolation of hydroxyapatite from *Thunnus obesus* bone," *Biomedical Materials*, **6**(3): p. 035003 (2011).
43. Barakat, N.A.M., Khalil, K.A., Sheikh, F.A., Omran, A.M., Gaihre, B., Khil, S.M., and Kim, H.Y., "Physiochemical characterizations of hydroxyapatite extracted from bovine bones by three different methods: Extraction of biologically desirable HAp," *Materials Science & Engineering C-Biomimetic and Supramolecular Systems*, **28**(8): p. 1381-1387 (2008).
44. Barakat, N.A.M., Khil, M.S., Omran, A.M., Sheikh, F.A., and Kim, H.Y., "Extraction of pure natural hydroxyapatite from the bovine bones bio waste by three different methods," *Journal of Materials Processing Technology*, **209**(7): p. 3408-3415 (2009).

45. Ooi, C.Y., Hamdi, M., and Ramesh, S., "Properties of hydroxyapatite produced by annealing of bovine bone," *Ceramics International*, **33**(7): p. 1171-1177 (2007).
46. Toque, J.A., Herliansyah, M.K., Hamdi, M., Ide-Ektessabi, A., and Wildan, M.W., *The effect of sample preparation and calcination temperature on the production of hydroxyapatite from bovine bone powders*, in *3rd Kuala Lumpur International Conference on Biomedical Engineering 2006: Biomed 2006, 11 – 14 December 2006 Kuala Lumpur, Malaysia*, F. Ibrahim, et al., Editors. 2007, Springer Berlin Heidelberg: Berlin, Heidelberg. p. 152-155.
47. Termine, J.D., Eanes, E.D., Greenfield, D.J., Nylen, M.U., and Harper, R.A., "Hydrazine-deproteinated bone mineral," *Calcified Tissue Research*, **12**(1): p. 73-90 (1973).
48. Bertazzo, S. and Bertran, C.A., "Effect of hydrazine deproteination on bone mineral phase: A critical view," *Journal of Inorganic Biochemistry*, **102**(1): p. 137-145 (2008).
49. Kim, H.M., Rey, C., and Glimcher, M.J., "Isolation of calcium - phosphate crystals of bone by non - aqueous methods at low temperature," *Journal of Bone and Mineral Research*, **10**(10): p. 1589-1601 (1995).
50. Tomazic, B.B., Brown, W.E., and Eanes, E.D., "A critical evaluation of the purification of biominerals by hypochlorite treatment," *Journal of Biomedical Materials Research Part A*, **27**(2): p. 217-225 (1993).
51. Wynnyckyj, C., Omelon, S., Willett, T., Kyle, K., Goldberg, H., and Grynepas, M., "Mechanism of bone collagen degradation due to KOH treatment," *Biochimica et Biophysica Acta (BBA)-General Subjects*, **1810**(2): p. 192-201 (2011).
52. Karlsmark, T., Danielsen, L., Thomsen, H., Aalund, O., Nielsen, K., Nielsen, O., and Genefke, I., "The effect of sodium hydroxide and hydrochloric acid on pig dermis. A light microscopic study," *Forensic Science International*, **39**(3): p. 227-233 (1988).
53. Uklejewski, R., Winiecki, M., Musielak, G., and Tokowicz, R., "Effectiveness of various deproteinization processes of bovine cancellous bone evaluated via mechano-biostructural properties of produced osteoconductive biomaterials," *Biotechnology and Bioprocess Engineering*, **20**(2): p. 259-266 (2015).
54. Weiner, S. and Price, P.A., "Disaggregation of bone into crystals," *Calcified Tissue International*, **39**(6): p. 365-375 (1986).
55. Termine, J.D., Belcourt, A.B., Conn, K.M., and Kleinman, H.K., "Mineral and collagen-binding proteins of fetal calf bone," *Journal of Biological Chemistry*, **256**(20): p. 403-408 (1981).

56. Termine, J.D., Conn, K.M., Kleinman, H.K., Martin, G.R., and Whitson, S.W., "Osteonectin, a mineral and collagen binding-protein of fetal calf bone," *Calcified Tissue International*, **33**(3): p. 302-302 (1981).
57. Glimcher, M.J., "Mechanism of calcification: role of collagen fibrils and collagen phosphoprotein complexes in vitro and in vivo," *Anatomical Record*, **224**(2): p. 139-153 (1989).
58. Morris, M.D. and Mandair, G.S., "Raman assessment of bone quality," *Clinical Orthopaedics and Related Research®*, **469**(8): p. 2160-2169 (2011).
59. Mandair, G.S. and Morris, M.D., "Contributions of Raman spectroscopy to the understanding of bone strength," *BoneKEy Reports*, **4**(2015).
60. Akkus, O., Adar, F., and Schaffler, M.B., "Age-related changes in physicochemical properties of mineral crystals are related to impaired mechanical function of cortical bone," *Bone*, **34**(3): p. 443-453 (2004).
61. Martiniakova, M., Grosskopf, B., Omelka, R., Vondrakova, M., and Bauerova, M., "Differences among species in compact bone tissue microstructure of mammalian skeleton: use of a discriminant function analysis for species identification," *Journal of Forensic Sciences*, **51**(6): p. 1235-1239 (2006).
62. Urist, M.R., Behnam, K., Kerendi, F., Raskin, K., Nuygen, T.D., Shamie, A.N., and Malinin, T.I., "Lipids closely associated with bone morphogenetic protein (BMP) .. and induced heterotopic bone formation. With preliminary observations of deficiencies in lipid and osteoinduction in lathyrism in rats," *Connective Tissue Research*, **36**(1): p. 9-20 (1997).
63. Fages, J., Marty, A., Delga, C., Condoret, J.S., Combes, D., and Frayssinet, P., "Use of supercritical CO₂ for bone delipidation," *Biomaterials*, **15**(9): p. 650-656 (1994).
64. Feng, L.A. and Jasiuk, I., "Multi-scale characterization of swine femoral cortical bone," *Journal of Biomechanics*, **44**(2): p. 313-320 (2011).
65. Locke, M., "Structure of long bones in mammals," *Journal of Morphology*, **262**(2): p. 546-565 (2004).
66. Almany Magal, R., Reznikov, N., Shahar, R., and Weiner, S., "Three-dimensional structure of minipig fibrolamellar bone: Adaptation to axial loading," *Journal of Structural Biology*, **186**(2): p. 253-264 (2014).

67. Chittenden, M., Najafi, A.R., Li, J., and Jasiuk, I., "Nanoindentation and ash content study of age dependent changes in porcine cortical bone," *Journal of Mechanics in Medicine and Biology*, **15**(5)(2015).
68. Martiniaková, M., Grosskopf, B., Omelka, R., Dammers, K., Vondráková, M., and Bauerová, M., "Histological study of compact bone tissue in some mammals: a method for species determination," *International Journal of Osteoarchaeology*, **17**(1): p. 82-90 (2007).
69. Mehdawi, I.M. and Young, A., *Antibacterial composite restorative materials for dental applications*, in *Biomaterials and Medical Device-associated Infections*. 2015, Woodhead Publishing: Oxford. p. 199-221.
70. Bagambisa, F., Joos, U., and Schilli, W., "A scanning electron microscope study of the ultrastructural organization of bone mineral," *Cells and Materials*, **3**(1): p. 10 (1993).
71. Chen, P.Y., Novitskaya, E., Lopez, M.I., Sun, C.Y., and McKittrick, J., "Toward a better understanding of mineral microstructure in bony tissues," *Bioinspired, Biomimetic and Nanobiomaterials*, **3**(2): p. 71-84 (2014).
72. Fratzl, P., Schreiber, S., and Klaushofer, K., "Bone mineralization as studied by small-angle X-ray scattering," *Connective Tissue Research*, **35**(1-4): p. 9-16 (1996).
73. Hamed, E., Novitskaya, E., Li, J., Chen, P.Y., Jasiuk, I., and McKittrick, J., "Elastic moduli of untreated, demineralized and deproteinized cortical bone: Validation of a theoretical model of bone as an interpenetrating composite material," *Acta Biomaterialia*, **8**(3): p. 1080-1092 (2012).
74. Di Renzo, M., Ellis, T.H., Sacher, E., and Stangel, I., "A photoacoustic FTIRS study of the chemical modifications of human dentin surfaces: II. Deproteination," *Biomaterials*, **22**(8): p. 793-797 (2001).
75. Tas, A.C., "X-ray diffraction data for flux-grown calcium hydroxyapatite whiskers," *Powder Diffraction*, **16**(2): p. 102-106 (2012).
76. Jackson, S.A., Cartwright, A.G., and Lewis, D., "The morphology of bone mineral crystals," *Calcified Tissue Research*, **25**(1): p. 217-222 (1978).
77. Meneghini, C., Dalconi, M.C., Nuzzo, S., Mobilio, S., and Wenk, R.H., "Rietveld refinement on X-ray diffraction patterns of bioapatite in human fetal bones," *Biophysical Journal*, **84**(3): p. 2021-2029 (2003).

78. Rey, C., Shimizu, M., Collins, B., and Glimcher, M.J., "Resolution-enhanced Fourier transform infrared spectroscopy study of the environment of phosphate ions in the early deposits of a solid phase of calcium-phosphate in bone and enamel, and their evolution with age. I: investigations in the $\nu_4\text{PO}_4$ domain," *Calcified Tissue International*, **46**(6): p. 384-394 (1990).
79. Francis, M.D. and Webb, N.C., "Hydroxyapatite formation from a hydrated calcium monohydrogen phosphate precursor," *Calcified Tissue International*, **6**(1): p. 335-342 (1970).
80. Lin, F.-H., Lin, C.-C., Lu, C.-M., Liu, H.-C., Sun, J.-S., and Wang, C.-Y., "Mechanical properties and histological evaluation of sintered $\beta\text{-Ca}_2\text{P}_2\text{O}_7$ with $\text{Na}_4\text{P}_2\text{O}_7 \cdot 10\text{H}_2\text{O}$ addition," *Biomaterials*, **16**(10): p. 793-802 (1995).
81. Johnsson, M.S.-A. and Nancollas, G.H., "The role of brushite and octacalcium phosphate in apatite formation," *Critical Reviews in Oral Biology & Medicine*, **3**(1): p. 61-82 (1992).
82. Crane, N.J., Popescu, V., Morris, M.D., Steenhuis, P., and Ignelzi, M.A., "Raman spectroscopic evidence for octacalcium phosphate and other transient mineral species deposited during intramembranous mineralization," *Bone*, **39**(3): p. 434-442 (2006).
83. Czamara, K., Majzner, K., Pacia, M.Z., Kochan, K., Kaczor, A., and Baranska, M., "Raman spectroscopy of lipids: a review," *Journal of Raman Spectroscopy*, **46**(1): p. 4-20 (2015).
84. Rho, J.Y., Kuhn-Spearing, L., and Zioupos, P., "Mechanical properties and the hierarchical structure of bone," *Medical Engineering & Physics*, **20**(2): p. 92-102 (1998).
85. Weiner, S. and Traub, W., "Bone structure from angstroms to microns," *The FASEB Journal*, **6**(3): p. 879-885 (1992).
86. Reznikov, N., Shahar, R., and Weiner, S., "Three-dimensional structure of human lamellar bone: the presence of two different materials and new insights into the hierarchical organization," *Bone*, **59**: p. 93-104 (2014).
87. Ambrose, S.H. and Krigbaum, J., "Bone chemistry and bioarchaeology," *Journal of Anthropological Archaeology*, **22**(3): p. 193-199 (2003).
88. Schwarcz, H.P. and Schoeninger, M.J., "Stable isotope analyses in human nutritional ecology," *American Journal of Physical Anthropology*, **34**(S13): p. 283-321 (1991).
89. Michelson, J.D. and Curl, L.A., "Use of demineralized bone matrix in hindfoot arthrodesis," *Clinical Orthopaedics and Related Research*, **325**: p. 203-208 (1996).

90. Neigel, J.M. and Ruzicka, P.O., "Use of demineralized bone implants in orbital and craniofacial reconstruction and a review of the literature," *Ophthalmic Plastic & Reconstructive Surgery*, **12**(2): p. 108-120 (1996).
91. Dahners, L.E. and Jacobs, R.R., "Long bone defects treated with demineralized bone," *Southern Medical Journal*, **78**(8): p. 933-934 (1985).
92. Groeneveld, E., Van Den Bergh, J., Holzmann, P., Ten Bruggenkate, C., Tuinzing, D., and Burger, E., "Mineralization processes in demineralized bone matrix grafts in human maxillary sinus floor elevations," *Journal of Biomedical Materials Research Part A*, **48**(4): p. 393-402 (1999).
93. Gepstein, R., Weiss, R.E., and Hallel, T., "Bridging large defects in bone by demineralized bone matrix in the form of a powder. A radiographic, histological, and radioisotope-uptake study in rats," *Journal of Bone and Joint Surgery*, **69**(7): p. 984-992 (1987).
94. Martin, G.J.J., Boden, S.D., Titus, L., and Scarborough, N.L., "New formulations of demineralized bone matrix as a more effective graft alternative in experimental posterolateral lumbar spine arthrodesis," *Spine*, **24**(7): p. 637-645 (1999).
95. Huggins, C., Wiseman, S., and Reddi, A., "Transformation of fibroblasts by allogeneic and xenogeneic transplants of demineralized tooth and bone," *Journal of Experimental Medicine*, **132**(6): p. 1250-1258 (1970).
96. Ajie, H.O., Hauschka, P.V., Kaplan, I.R., and Sobel, H., "Comparison of bone collagen and osteocalcin for determination of radiocarbon ages and paleodietary reconstruction," *Earth and Planetary Science Letters*, **107**(2): p. 380-388 (1991).
97. Frank, J.D., Balena, R., Masarachia, P., Seedor, J.G., and Cartwright, M.E., "The effects of three different demineralization agents on osteopontin localization in adult rat bone using immunohistochemistry," *Histochemistry and Cell Biology*, **99**(4): p. 295-301 (1993).
98. Amaral, N.G.D., Rezende, M.L.R.d., Hirata, F., Rodrigues, M.G.S., Sant'Ana, A.C.P., Greggi, S.L.A., and Passanezi, E., "Comparison among four commonly used demineralizing agents for root conditioning: A scanning electron microscopy," *Journal of Applied Oral Science*, **19**(5): p. 469-475 (2011).
99. Ruggeri, A., Prati, C., Mazzoni, A., Nucci, C., Di Lenarda, R., Mazzotti, G., and Breschi, L., "Effects of citric acid and EDTA conditioning on exposed root dentin: An immunohistochemical analysis of collagen and proteoglycans," *Archives of Oral Biology*, **52**(1): p. 1-8 (2007).

100. Castania, V.A., Silveira, J.W.d.S.d., Issy, A.C., Pitol, D.L., Castania, M.L., Neto, A.D., Del Bel, E.A., and Defino, H.L.A., "Advantages of a combined method of decalcification compared to EDTA," *Microscopy Research and Technique*, **78**(2): p. 111-118 (2015).
101. Wang, X., Shen, X., Li, X., and Mauli Agrawal, C., "Age-related changes in the collagen network and toughness of bone," *Bone*, **31**(1): p. 1-7 (2002).
102. Katz, J.L., Spencer, P., Nomura, T., Wagh, A., and Wang, Y., "Micromechanical properties of demineralized dentin collagen with and without adhesive infiltration," *Journal of Biomedical Materials Research Part A*, **66**(1): p. 120-128 (2003).
103. Chen, J., Burger, C., Krishnan, C.V., Chu, B., Hsiao, B.S., and Glimcher, M.J., "In vitro mineralization of collagen in demineralized fish bone," *Macromolecular Chemistry and Physics*, **206**(1): p. 43-51 (2005).
104. Summitt, M.C. and Reisinger, K.D., "Characterization of the mechanical properties of demineralized bone," *Journal of Biomedical Materials Research Part A*, **67A**(3): p. 742-750 (2003).
105. Pestle, W.J., "Chemical, elemental, and isotopic effects of acid concentration and treatment duration on ancient bone collagen: an exploratory study," *Journal of Archaeological Science*, **37**(12): p. 3124-3128 (2010).
106. Vashishth, D., Gibson, G.J., Khoury, J.I., Schaffler, M.B., Kimura, J., and Fyhrie, D.P., "Influence of nonenzymatic glycation on biomechanical properties of cortical bone," *Bone*, **28**(2): p. 195-201 (2001).
107. Ramakrishnaiah, R., Rehman, G.u., Basavarajappa, S., Al Khuraif, A.A., Durgesh, B.H., Khan, A.S., and Rehman, I.u., "Applications of Raman spectroscopy in dentistry: Analysis of tooth structure," *Applied Spectroscopy Reviews*, **50**(4): p. 332-350 (2014).
108. Timchenko, E.V., Zherdeva, L.A., Timchenko, P.E., Volova, L.T., and Ponomareva, U.V., "Detailed analysis of the structural changes of bone matrix during the demineralization process using Raman spectroscopy," *Physics Procedia*, **73**: p. 221-227 (2015).
109. Figueiredo, M., Gamelas, J., and Martins, A., *Characterization of bone and bone-based graft materials using FTIR spectroscopy*, in *Infrared Spectroscopy-Life and Biomedical Sciences*. 2012, InTech.
110. Wartewig, S., *IR and Raman Spectroscopy: Fundamental Processing*. 2006: Wiley.

111. Sano, H., Ciucchi, B., Matthews, W.G., and Pashley, D.H., "Tensile properties of mineralized and demineralized human and bovine dentin," *Journal of Dental Research*, **73**(6): p. 1205-1211 (1994).
112. Lewandrowski, K.U., Tomford, W.W., Michaud, N.A., Schomacker, K.T., and Deutsch, T.F., "An electron microscopic study on the process of acid demineralization of cortical bone," *Calcified Tissue International*, **61**(4): p. 294-297 (1997).
113. Figueiredo, M., Cunha, S., Martins, G., Freitas, J., Judas, F., and Figueiredo, H., "Influence of hydrochloric acid concentration on the demineralization of cortical bone," *Chemical Engineering Research and Design*, **89**(1): p. 116-124 (2011).
114. Rai, D. and Singh, R., "Thermodynamic study of bone biocomposites," *Trends in Biomaterials & Artificial Organs*, **19**(1)(2005).
115. Deville, S., "Freeze-casting of porous ceramics: A review of current achievements and issues," *Advanced Engineering Materials*, **10**(3): p. 155-169 (2008).
116. Porter, M.M., Yeh, M., Strawson, J., Goehring, T., Lujan, S., Siripasopsotorn, P., Meyers, M.A., and McKittrick, J., "Magnetic freeze casting inspired by nature," *Materials Science and Engineering A-Structural Materials Properties Microstructure and Processing*, **556**: p. 741-750 (2012).
117. Bai, H., Polini, A., Delattre, B., and Tomsia, A.P., "Thermoresponsive composite hydrogels with aligned macroporous structure by ice-templated assembly," *Chemistry of Materials*, **25**(22): p. 4551-4556 (2013).
118. Divakar, P., Caruso, I., Moodie, K.L., Theiler, R.N., Hoopes, P.J., and Wegst, U.G., "Design, manufacture, and in vivo testing of a tissue scaffold for permanent female sterilization by tubal occlusion," *MRS Advances*: p. 1-6 (2018).
119. Short, K.W., Carpenter, S., Freyer, J.P., and Mourant, J.R., "Raman spectroscopy detects biochemical changes due to proliferation in mammalian cell cultures," *Biophysical Journal*, **88**(6): p. 4274-4288 (2005).
120. Kohn, D.H., Sahar, N.D., Wallace, J.M., Golcuk, K., and Morris, M.D., "Exercise alters mineral and matrix composition in the absence of adding new bone," *Cells Tissues Organs*, **189**(1-4): p. 33-37 (2009).
121. Pezzotti, G., Rondinella, A., Marin, E., Zhu, W., Aldini, N.N., Ulian, G., and Valdre, G., "Raman spectroscopic investigation on the molecular structure of apatite and collagen in osteoporotic cortical bone," *Journal of the Mechanical Behavior of Biomedical Materials*, **65**: p. 264-273 (2017).

122. Awonusi, A., Morris, M.D., and Tecklenburg, M.M., "Carbonate assignment and calibration in the Raman spectrum of apatite," *Calcified Tissue International*, **81**(1): p. 46-52 (2007).
123. Carden, A., Rajachar, R.M., Morris, M.D., and Kohn, D.H., "Ultrastructural changes accompanying the mechanical deformation of bone tissue: a Raman imaging study," *Calcified Tissue International*, **72**(2): p. 166-175 (2003).
124. Goodyear, S.R., Gibson, I.R., Skakle, J.M., Wells, R.P., and Aspden, R.M., "A comparison of cortical and trabecular bone from C57 Black 6 mice using Raman spectroscopy," *Bone*, **44**(5): p. 899-907 (2009).
125. Rajan, N., Habermehl, J., Coté, M.-F., Doillon, C.J., and Mantovani, D., "Preparation of ready-to-use, storable and reconstituted type I collagen from rat tail tendon for tissue engineering applications," *Nature Protocols*, **1**: p. 2753 (2007).
126. Thomas, C.B., Jenkins, L., Kellam, J.F., and Burg, K.J., *Endpoint verification of bone demineralization for tissue engineering applications*, in *Tissue Engineered Medical Products (TEMPs)*. 2004, ASTM International.
127. Callis, G. and Sterchi, D., "Decalcification of bone: Literature review and practical study of various decalcifying agents, methods, and their effects on bone histology," *Journal of Histotechnology*, **21**(1): p. 49-58 (1998).
128. Bellali, F., Kharroubi, M., Hmimid, F., Loutfi, M., and Bourhim, N., "Conditions optimization for demineralization of sardine scales with hydrolic acid using factorial experimental design," *Journal of Materials and Environmental Science*, **8**(1): p. 14-21 (2017).
129. Anastassopoulou, J., Kolovou, P., Papagelopoulos, P., and Theophanides, T., *The role of β -antagonists on the structure of human bone-A spectroscopic study*, in *Infrared Spectroscopy-Life and Biomedical Sciences*. 2012, InTech.
130. Lee, Y.-C., Chiang, C.-C., Huang, P.-Y., Chung, C.-Y., Huang, T.D., Wang, C.-C., Chen, C.-I., Chang, R.-S., Liao, C.-H., and Reisz, R.R., "Evidence of preserved collagen in an Early Jurassic sauropodomorph dinosaur revealed by synchrotron FTIR microspectroscopy," *Nature Communications*, **8**: p. 14220 (2017).
131. Fowler, B., "Infrared studies of apatites. I. Vibrational assignments for calcium, strontium, and barium hydroxyapatites utilizing isotopic substitution," *Inorganic Chemistry*, **13**(1): p. 194-207 (1974).

132. Gadaleta, S.J., Paschalis, E.P., Betts, F., Mendelsohn, R., and Boskey, A.L., "Fourier transform infrared spectroscopy of the solution-mediated conversion of amorphous calcium phosphate to hydroxyapatite: New correlations between X-ray diffraction and infrared data," *Calcified Tissue International*, **58**(1): p. 9-16 (1996).
133. Vedantham, G., Sparks, H.G., Sane, S.U., Tzannis, S., and Przybycien, T.M., "A holistic approach for protein secondary structure estimation from infrared spectra in H₂O solutions," *Analytical Biochemistry*, **285**(1): p. 33-49 (2000).
134. Schliephake, H. and Scharnweber, D., "Chemical and biological functionalization of titanium for dental implants," *Journal of Materials Chemistry*, **18**(21): p. 2404-2414 (2008).
135. Jackson, M., Watson, P.H., Halliday, W.C., and Mantsch, H.H., "Beware of connective tissue proteins: assignment and implications of collagen absorptions in infrared spectra of human tissues," *Biochimica et Biophysica Acta (BBA)-Molecular Basis of Disease*, **1270**(1): p. 1-6 (1995).
136. Rieppo, L., Saarakkala, S., Närhi, T., Helminen, H., Jurvelin, J., and Rieppo, J., "Application of second derivative spectroscopy for increasing molecular specificity of Fourier transform infrared spectroscopic imaging of articular cartilage," *Osteoarthritis and Cartilage*, **20**(5): p. 451-459 (2012).
137. Krimm, S. and Bandekar, J., "Vibrational spectroscopy and conformation of peptides, polypeptides, and proteins," *Advances in Protein Chemistry*, **38**: p. 181-364 (1986).
138. Garidel, P. and Schott, H., "Fourier-transform midinfrared spectroscopy for analysis and screening of liquid protein formulations," *BioProcess International*, **4**(6): p. 48-55 (2006).
139. Kabsch, W. and Sander, C., "Dictionary of protein secondary structure: pattern recognition of hydrogen - bonded and geometrical features," *Biopolymers*, **22**(12): p. 2577-2637 (1983).
140. Kolovou, P. and Anastassopoulou, J., *Synchrotron FT-IR spectroscopy of human bones. The effect of aging*, in *Brilliant Light in Life and Material Sciences*. 2007, Springer. p. 267-272.
141. Mamarelis, I., Pissaridi, K., Dritsa, V., Kotileas, P., Tsiligiris, V., Tzilalis, V., and Anastassopoulou, J., "Oxidative stress and atherogenesis. An FT-IR spectroscopic study," *In Vivo*, **24**(6): p. 883-888 (2010).
142. Frank, M.B., Naleway, S.E., Wirth, T.S., Jung, J.-Y., Cheung, C.L., Loera, F.B., Medina, S., Sato, K.N., Taylor, J.R., and McKittrick, J., "A protocol for bioinspired design: A

- ground sampler based on sea urchin jaws," *JoVE (Journal of Visualized Experiments)*(110): p. e53554-e53554 (2016).
143. Dimas, L.S., Bratzel, G.H., Eylon, I., and Buehler, M.J., "Tough composites inspired by mineralized natural materials: computation, 3D printing, and testing," *Advanced Functional Materials*, **23**(36): p. 4629-4638 (2013).
 144. Libonati, F., Gu, G.X., Qin, Z., Vergani, L., and Buehler, M.J., "Bone - inspired materials by design: toughness amplification observed using 3D printing and testing," *Advanced Engineering Materials*, **18**(8): p. 1354-1363 (2016).
 145. Gu, G.X., Takaffoli, M., Hsieh, A.J., and Buehler, M.J., "Biomimetic additive manufactured polymer composites for improved impact resistance," *Extreme Mechanics Letters*, **9**: p. 317-323 (2016).
 146. Zhang, P., Heyne, M.A., and To, A.C., "Biomimetic staggered composites with highly enhanced energy dissipation: Modeling, 3D printing, and testing," *Journal of the Mechanics and Physics of Solids*, **83**: p. 285-300 (2015).
 147. Gu, G.X., Takaffoli, M., and Buehler, M.J., "Hierarchically enhanced impact resistance of bioinspired composites," *Advanced Materials*, **29**(28)(2017).
 148. Lin, E., Li, Y., Ortiz, C., and Boyce, M.C., "3D printed, bio-inspired prototypes and analytical models for structured suture interfaces with geometrically-tuned deformation and failure behavior," *Journal of the Mechanics and Physics of Solids*, **73**: p. 166-182 (2014).
 149. Lin, E., Li, Y., Weaver, J.C., Ortiz, C., and Boyce, M.C., "Tunability and enhancement of mechanical behavior with additively manufactured bio-inspired hierarchical suture interfaces," *Journal of Materials Research*, **29**(17): p. 1867-1875 (2014).
 150. Jasiuk, I., Abueidda, D.W., Kozuch, C., Pang, S.Y., Su, F.Y., and McKittrick, J., "An overview on additive manufacturing of polymers," *JOM*, **70**(3): p. 275-283 (2018).
 151. Cho, H., Weaver, J.C., Poselt, E., in't Veld, P.J., Boyce, M.C., and Rutledge, G.C., "Engineering the mechanics of heterogeneous soft crystals," *Advanced Functional Materials*, **26**(38): p. 6938-6949 (2016).
 152. Gu, G.X., Libonati, F., Wettermark, S.D., and Buehler, M.J., "Printing nature: Unraveling the role of nacre's mineral bridges," *Journal of the Mechanical Behavior of Biomedical Materials*, **76**: p. 135-144 (2017).

153. Yap, Y.L., Wang, C., Sing, S.L., Dikshit, V., Yeong, W.Y., and Wei, J., "Material jetting additive manufacturing: An experimental study using designed metrological benchmarks," *Precision Engineering*, **50**(Supplement C): p. 275-285 (2017).
154. Slesarenko, V. and Rudykh, S., "Towards mechanical characterization of soft digital materials for multimaterial 3D-printing," *International Journal of Engineering Science*, **123**: p. 62-72 (2018).
155. Bass, L., Meisel, N.A., and Williams, C.B., "Exploring variability of orientation and aging effects in material properties of multi-material jetting parts," *Rapid Prototyping Journal*, **22**(5): p. 826-834 (2016).
156. Sabet, F.A., Su, F.Y., McKittrick, J., and Jasiuk, I., "Mechanical properties of model two - phase composites with continuous compared to discontinuous phases," *Advanced Engineering Materials*(2018).
157. Blaber, J., Adair, B., and Antoniou, A., "Ncorr: open-source 2D digital image correlation MATLAB software," *Experimental Mechanics*, **55**(6): p. 1105-1122 (2015).
158. Yeoh, O.H., "Some forms of the strain energy function for rubber," *Rubber Chemistry and Technology*, **66**(5): p. 754-771 (1993).
159. Mueller, J., Shea, K., and Daraio, C., "Mechanical properties of parts fabricated with inkjet 3D printing through efficient experimental design," *Materials & Design*, **86**: p. 902-912 (2015).
160. Huet, C., "Application of variational concepts to size effects in elastic heterogeneous bodies," *Journal of the Mechanics and Physics of Solids*, **42**: p. 1995-2011 (1990).
161. Onck, P.R., Andrews, E.W., and Gibson, L.J., "Size effects in ductile cellular solids. Part I: modeling," *International Journal of Mechanical Sciences*, **43**(3): p. 681-699 (2001).
162. Andrews, E.W., Gioux, G., Onck, P., and Gibson, L.J., "Size effects in ductile cellular solids. Part II: experimental results," *International Journal of Mechanical Sciences*, **43**(3): p. 701-713 (2001).
163. Alkhader, M. and Vural, M., "Mechanical response of cellular solids: Role of cellular topology and microstructural irregularity," *International Journal of Engineering Science*, **46**(10): p. 1035-1051 (2008).
164. Cho, J., Joshi, M.S., and Sun, C.T., "Effect of inclusion size on mechanical properties of polymeric composites with micro and nano particles," *Composites Science and Technology*, **66**(13): p. 1941-1952 (2006).

165. Fu, S.-Y., Feng, X.-Q., Lauke, B., and Mai, Y.-W., "Effects of particle size, particle/matrix interface adhesion and particle loading on mechanical properties of particulate-polymer composites," *Composites Part B: Engineering*, **39**(6): p. 933-961 (2008).
166. Gross, D. and Seelig, T., *Micromechanics and homogenization*, in *Fracture Mechanics*. 2018, Springer. p. 243-319.
167. Eggwertz, S. and Lind, N.C., *Probabilistic Methods in the Mechanics of Solids and Structures: Symposium Stockholm, Sweden, 1984*. 2012, Berlin, Germany: Springer Science & Business Media.
168. Brezny, R. and Green, D.J., "The effect of cell size on the mechanical behavior of cellular materials," *Acta Metallurgica et Materialia*, **38**(12): p. 2517-2526 (1990).
169. Towse, A., Potter, K., Wisnom, M.R., and Adams, R.D., "Specimen size effects in the tensile failure strain of an epoxy adhesive," *Journal of Materials Science*, **33**(17): p. 4307-4314 (1998).
170. Puskas, J.E., Dos Santos, L.M., Fischer, F., Götz, C., El Fray, M., Altstädt, V., and Tomkins, M., "Fatigue testing of implantable specimens: Effect of sample size and branching on the dynamic fatigue properties of polyisobutylene-based biomaterials," *Polymer*, **50**(2): p. 591-597 (2009).
171. Lakes, R., "Experimental microelasticity of two porous solids," *International Journal of Solids and Structures*, **22**(1): p. 55-63 (1986).
172. Anderson, W.B. and Lakes, R.S., "Size effects due to Cosserat elasticity and surface damage in closed-cell polymethacrylimide foam," *Journal of Materials Science*, **29**(24): p. 6413-6419 (1994).
173. Maxwell, W., Gurnick, R., and Francisco, A., "Preliminary investigation of the 'freeze-casting' method for forming refractory powders," *National Advisory Committee for Aeronautics*(1954).
174. Chino, Y. and Dunand, D.C., "Directionally freeze-cast titanium foam with aligned, elongated pores," *Acta Materialia*, **56**(1): p. 105-113 (2008).
175. Yook, S.-W., Yoon, B.-H., Kim, H.-E., Koh, Y.-H., and Kim, Y.-S., "Porous titanium (Ti) scaffolds by freezing TiH₂/camphene slurries," *Materials Letters*, **62**(30): p. 4506-4508 (2008).

176. Li, J.C. and Dunand, D.C., "Mechanical properties of directionally freeze-cast titanium foams," *Acta Materialia*, **59**(1): p. 146-158 (2011).
177. Ramos, A.I. and Dunand, D.C., "Preparation and characterization of directionally freeze-cast copper foams," *Metals*, **2**(3): p. 265-273 (2012).
178. Dash, R., Li, Y., and Ragauskas, A.J., "Cellulose nanowhisker foams by freeze casting," *Carbohydrate Polymers*, **88**(2): p. 789-792 (2012).
179. Zhou, Y., Fu, S., Pu, Y., Pan, S., and Ragauskas, A.J., "Preparation of aligned porous chitin nanowhisker foams by directional freeze-casting technique," *Carbohydrate Polymers*, **112**: p. 277-283 (2014).
180. Zhou, Y., Fu, S., Pu, Y., Pan, S., Levit, M.V., and Ragauskas, A.J., "Freeze-casting of cellulose nanowhisker foams prepared from a water-dimethylsulfoxide (DMSO) binary mixture at low DMSO concentrations," *RSC Advances*, **3**(42): p. 19272-19277 (2013).
181. Donius, A.E., Liu, A., Berglund, L.A., and Wegst, U.G., "Superior mechanical performance of highly porous, anisotropic nanocellulose-montmorillonite aerogels prepared by freeze casting," *Journal of the Mechanical Behavior of Biomedical Materials*, **37**: p. 88-99 (2014).
182. Qiu, L., Liu, J.Z., Chang, S.L., Wu, Y., and Li, D., "Biomimetic superelastic graphene-based cellular monoliths," *Nature Communications*, **3**: p. 1241 (2012).
183. Antink, M.M.H., Ropke, L., Bartels, J., Soltmann, C., Kunzmann, A., Rezwan, K., and Kroll, S., "Porous ceramics with tailored pore size and morphology as substrates for coral larval settlement," *Ceramics International*, **44**(14): p. 16561-16571 (2018).
184. Deville, S., "Freeze-casting of porous biomaterials: structure, properties and opportunities," *Materials*, **3**(3): p. 1913-1927 (2010).
185. Yoon, B.H., Koh, Y.H., Park, C.S., and Kim, H.E., "Generation of large pore channels for bone tissue engineering using camphene - based freeze casting," *Journal of the American Ceramic Society*, **90**(6): p. 1744-1752 (2007).
186. Zhang, Y., Zuo, K., and Zeng, Y.-P., "Effects of gelatin addition on the microstructure of freeze-cast porous hydroxyapatite ceramics," *Ceramics International*, **35**(6): p. 2151-2154 (2009).
187. Fu, Q., Rahaman, M.N., Bal, B.S., and Brown, R.F., "Proliferation and function of MC₃T₃-E₁ cells on freeze-cast hydroxyapatite scaffolds with oriented pore architectures," *Journal of Materials Science: Materials in Medicine*, **20**(5): p. 1159-1165 (2009).

188. Suetsugu, Y., Hotta, Y., Iwasashi, M., Sakane, M., Kikuchi, M., Ikoma, T., Higaki, T., Ochiai, N., and Tanaka, M., "Structural and tissue reaction properties of novel hydroxyapatite ceramics with unidirectional pores," *Key Engineering Materials*, **330**: p. 1003-1006 (2007).
189. Yoon, B.-H., Choi, W.-Y., Kim, H.-E., Kim, J.-H., and Koh, Y.-H., "Aligned porous alumina ceramics with high compressive strengths for bone tissue engineering," *Scripta Materialia*, **58**(7): p. 537-540 (2008).
190. Hong, C., Zhang, X., Han, J., Du, J., and Han, W., "Ultra-high-porosity zirconia ceramics fabricated by novel room-temperature freeze-casting," *Scripta Materialia*, **60**(7): p. 563-566 (2009).
191. Bouville, F., Maire, E., Meille, S., Van de Moortele, B., Stevenson, A.J., and Deville, S., "Strong, tough and stiff bioinspired ceramics from brittle constituents," *Nature Materials*, **13**(5): p. 508-514 (2014).
192. Uhlmann, D.R., Chalmers, B., and Jackson, K.A., "Interaction between particles and a solid-liquid interface," *Journal of Applied Physics*, **35**(10): p. 7 (1964).
193. Araki, K. and Halloran, J.W., "Porous ceramic bodies with interconnected pore channels by a novel freeze casting technique," *Journal of the American Ceramic Society*, **88**(5): p. 1108-1114 (2005).
194. Peppin, S.S., Worster, M.G., and Wettlaufer, J. *Morphological instability in freezing colloidal suspensions*. in *Proceedings of the Royal Society of London A: Mathematical, Physical and Engineering Sciences*. 2007. The Royal Society.
195. Peppin, S.S.L., Wettlaufer, J.S., and Worster, M.G., "Experimental verification of morphological instability in freezing aqueous colloidal suspensions," *Physical Review Letters*, **100**(23)(2008).
196. Deville, S., Maire, E., Lasalle, A., Bogner, A., Gauthier, C., Leloup, J., and Guizard, C., "In situ X - ray radiography and tomography observations of the solidification of aqueous alumina particles suspensions. Part II: Steady state," *Journal of the American Ceramic Society*, **92**(11): p. 2497-2503 (2009).
197. Mukai, S.R., Nishihara, H., and Tamon, H., "Formation of monolithic silica gel microhoneycombs (SMHs) using pseudosteady state growth of microstructural ice crystals," *Chemical Communications*(7): p. 874-875 (2004).
198. Koh, Y.H., Lee, E.J., Yoon, B.H., Song, J.H., Kim, H.E., and Kim, H.W., "Effect of polystyrene addition on freeze casting of ceramic/camphene slurry for ultra - high

- porosity ceramics with aligned pore channels," *Journal of the American Ceramic Society*, **89**(12): p. 3646-3653 (2006).
199. Shanti, N.O., Araki, K., and Halloran, J.W., "Particle redistribution during dendritic solidification of particle suspensions," *Journal of the American Ceramic Society*, **89**(8): p. 2444-2447 (2006).
 200. Deville, S., Saiz, E., and Tomsia, A.P., "Ice-templated porous alumina structures," *Acta Materialia*, **55**(6): p. 1965-1974 (2007).
 201. Fukasawa, T., Ando, M., Ohji, T., and Kanzaki, S., "Synthesis of porous ceramics with complex pore structure by freeze - dry processing," *Journal of the American Ceramic Society*, **84**(1): p. 230-232 (2001).
 202. Deville, S., Saiz, E., Nalla, R.K., and Tomsia, A.P., "Freezing as a path to build complex composites," *Science*, **311**(5760): p. 515-518 (2006).
 203. Nakata, M., Tanihata, K., Yamaguchi, S., and Sukanuma, K., "Fabrication of porous alumina sintered bodies by a gelate-freezing method," *Journal of the Ceramic Society of Japan*, **113**(1323): p. 712-715 (2005).
 204. Zhang, H., Hussain, I., Brust, M., Butler, M.F., Rannard, S.P., and Cooper, A.I., "Aligned two-and three-dimensional structures by directional freezing of polymers and nanoparticles," *Nature Materials*, **4**(10): p. 787 (2005).
 205. Tang, Y., Zhao, K., Hu, L., and Wu, Z., "Two-step freeze casting fabrication of hydroxyapatite porous scaffolds with bionic bone graded structure," *Ceramics International*, **39**(8): p. 9703-9707 (2013).
 206. Moon, J.W., Hwang, H.J., Awano, M., and Maeda, K., "Preparation of NiO-YSZ tubular support with radially aligned pore channels," *Materials Letters*, **57**(8): p. 1428-1434 (2003).
 207. Tang, Y.F., Miao, Q., Qiu, S., Zhao, K., and Hu, L., "Novel freeze-casting fabrication of aligned lamellar porous alumina with a centrosymmetric structure," *Journal of the European Ceramic Society*, **34**(15): p. 4077-4082 (2014).
 208. Leis, J.M., "Nomenclature and distribution of the species of the porcupinefish family Diodontidae (Pisces, Teleostei)," *Memoirs of Victoria Museum*, **63**(1): p. 77-90 (2006).
 209. Brainerd, E.L., "Pufferfish inflation: functional morphology of postcranial structures in *Diodon holocanthus* (Tetraodontiformes)," *Journal of Morphology*, **220**(3): p. 243-261 (1994).

210. Su, F.Y., Bushong, E.A., Deerinck, T.J., Seo, K., Herrera, S., Graeve, O.A., Kisailus, D., Lubarda, V.A., and McKittrick, J., "Spines of the porcupine fish: Structure, composition, and mechanical properties," *Journal of the Mechanical Behavior of Biomedical Materials*(2017).
211. Zhu, D.J., Ortega, C.F., Motamedi, R., Szewciw, L., Vernerey, F., and Barthelat, F., "Structure and mechanical performance of a "modern" fish scale," *Advanced Engineering Materials*, **14**(4): p. B185-B194 (2012).
212. Yu, Z.B. and Krstic, V.D., "Fabrication and characterization of laminated SiC ceramics with self-sealed ring structure," *Journal of Materials Science*, **38**(23): p. 4735-4738 (2003).
213. Marshall, D.B., Ratto, J.J., and Lange, F.F., "Enhanced fracture toughness in layered microcomposites of Ce - ZrO₂ and Al₂O₃," *Journal of the American Ceramic Society*, **74**(12): p. 2979-2987 (1991).
214. Williams, J.T., Carpenter, K.E., Van Tassell, J.L., Hoetjes, P., Toller, W., Etnoyer, P., and Smith, M., "Biodiversity assessment of the fishes of Saba Bank atoll, Netherlands Antilles," *PLOS ONE*, **5**(5): p. e10676 (2010).
215. ASTM International, *ASTM C39/C39M-18, Standard Test Method for Compressive Strength of Cylindrical Concrete Specimens*. 1921 (2015), ASTM International: West Conshohocken, PA.
216. ASTM International, *ASTM D3967-16, Standard Test Method for Splitting Tensile Strength of Intact Rock Core Specimens*. 1981 (2016), ASTM International: West Conshohocken, PA.
217. Li, D.Y. and Wong, L.N.Y., "The Brazilian disc test for rock mechanics applications: review and new insights," *Rock Mechanics and Rock Engineering*, **46**(2): p. 269-287 (2013).
218. Waschkie, T., Oberacker, R., and Hoffmann, M.J., "Control of lamellae spacing during freeze casting of ceramics using double-side cooling as a novel processing route," *Journal of the American Ceramic Society*, **92**(1): p. S79-S84 (2009).
219. Nalla, R.K., Kinney, J.H., and Ritchie, R.O., "Mechanistic fracture criteria for the failure of human cortical bone," *Nature Materials*, **2**(3): p. 164-168 (2003).
220. Pesce, V., Speciale, D., Sammarco, G., Patella, S., Spinarelli, A., and Patella, V., "Surgical approach to bone healing in osteoporosis," *Clinical Cases in Mineral and Bone Metabolism*, **6**(2): p. 131 (2009).

221. Brydone, A.S., Meek, D., and Maclaine, S., "Bone grafting, orthopaedic biomaterials, and the clinical need for bone engineering," *Proceedings of the Institution of Mechanical Engineers Part H-Journal of Engineering in Medicine*, **224**(H12): p. 1329-1343 (2010).
222. Wahl, D. and Czernuszka, J., "Collagen-hydroxyapatite composites for hard tissue repair," *European Cells & Materials*, **11**: p. 43-56 (2006).
223. Lawson, A.C. and Czernuszka, J., "Collagen-calcium phosphate composites," *Proceedings of the Institution of Mechanical Engineers, Part H: Journal of Engineering in Medicine*, **212**(6): p. 413-425 (1998).
224. Kikuchi, M., Ikoma, T., Itoh, S., Matsumoto, H.N., Koyama, Y., Takakuda, K., Shinomiya, K., and Tanaka, J., "Biomimetic synthesis of bone-like nanocomposites using the self-organization mechanism of hydroxyapatite and collagen," *Composites Science and Technology*, **64**(6): p. 819-825 (2004).
225. Bradt, J.-H., Mertig, M., Teresiak, A., and Pompe, W., "Biomimetic mineralization of collagen by combined fibril assembly and calcium phosphate formation," *Chemistry of Materials*, **11**(10): p. 2694-2701 (1999).
226. Pompe, W., Worch, H., Epple, M., Friess, W., Gelinsky, M., Greil, P., Hempel, U., Scharnweber, D., and Schulte, K., "Functionally graded materials for biomedical applications," *Materials Science and Engineering A-Structural Materials Properties Microstructure and Processing*, **362**(1-2): p. 40-60 (2003).
227. Venugopal, J., Low, S., Choon, A.T., Sampath Kumar, T.S., and Ramakrishna, S., "Mineralization of osteoblasts with electrospun collagen/hydroxyapatite nanofibers," *Journal of Materials Science: Materials in Medicine*, **19**(5): p. 2039-2046 (2008).
228. Teng, S.-H., Lee, E.-J., Wang, P., and Kim, H.-E., "Collagen/hydroxyapatite composite nanofibers by electrospinning," *Materials Letters*, **62**(17): p. 3055-3058 (2008).
229. Asran, A.S., Henning, S., and Michler, G.H., "Polyvinyl alcohol–collagen–hydroxyapatite biocomposite nanofibrous scaffold: Mimicking the key features of natural bone at the nanoscale level," *Polymer*, **51**(4): p. 868-876 (2010).
230. Villa, M.M., Wang, L., Huang, J., Rowe, D.W., and Wei, M., "Bone tissue engineering with a collagen–hydroxyapatite scaffold and culture expanded bone marrow stromal cells," *Journal of Biomedical Materials Research Part B: Applied Biomaterials*(2014).
231. Lee, S., Porter, M., Wasko, S., Lau, G., Chen, P.-Y., Novitskaya, E.E., Tomsia, A.P., Almutairi, A., Meyers, M.A., and McKittrick, J. *Potential bone replacement materials prepared by two methods*. in *MRS Proceedings*. 2012. Cambridge Univ Press.

232. Zhang, H. and Cooper, A.I., "Aligned porous structures by directional freezing," *Advanced Materials*, **19**(11): p. 1529-1533 (2007).
233. Divakar, P., Yin, K., and Wegst, U.G., "Anisotropic freeze-cast collagen scaffolds for tissue regeneration: How processing conditions affect structure and properties in the dry and fully hydrated states," *Journal of the Mechanical Behavior of Biomedical Materials*(2018).
234. Frank, M.B., *Applications Bioinspired by Sea Urchins and Spongy Bone*. 2017, UC San Diego.
235. Yu, X.Y., Tang, C., Xiong, S.B., Yuan, Q.J., Gu, Z.P., Li, Z., and Hu, Y., "Modification of collagen for biomedical applications: A review of physical and chemical methods," *Current Organic Chemistry*, **20**(17): p. 1797-1812 (2016).
236. Amri, M., Firdaus, M., Fauzi, M., Chowdhury, S.R., Fadilah, N., Wan Hamirul, W., Reusmaazran, M., Aminuddin, B., and Ruszymah, B., "Cytotoxic evaluation of biomechanically improved crosslinked ovine collagen on human dermal fibroblasts," *Bio-medical Materials and Engineering*, **24**(4): p. 1715-1724 (2014).
237. Doyle, B.B., Bendit, E.G., and Blout, E.R., "Infrared spectroscopy of collagen and collagen-like polypeptides," *Biopolymers*, **14**(5): p. 937-957 (1975).
238. Usha, R., Sreeram, K.J., and Rajaram, A., "Stabilization of collagen with EDC/NHS in the presence of L-lysine: A comprehensive study," *Colloids and Surfaces B: Biointerfaces*, **90**: p. 83-90 (2012).
239. Sheu, M.-T., Huang, J.-C., Yeh, G.-C., and Ho, H.-O., "Characterization of collagen gel solutions and collagen matrices for cell culture," *Biomaterials*, **22**(13): p. 1713-1719 (2001).
240. Davidenko, N., Schuster, C.F., Bax, D.V., Raynal, N., Farndale, R.W., Best, S.M., and Cameron, R.E., "Control of crosslinking for tailoring collagen-based scaffolds stability and mechanics," *Acta Biomaterialia*, **25**: p. 131-142 (2015).
241. Wang, X.H., Li, D.P., Wang, W.J., Feng, Q.L., Cui, F.Z., Xu, Y.X., Song, X.H., and van der Werf, M., "Crosslinked collagen/chitosan matrix for artificial livers," *Biomaterials*, **24**(19): p. 3213-3220 (2003).
242. Margolis, H.C. and Moreno, E.C., "Kinetics of hydroxyapatite dissolution in acetic, lactic, and phosphoric acid solutions," *Calcified Tissue International*, **50**(2): p. 137-143 (1992).

243. Rasoulia, R., Najafi, A.R., Chittenden, M., and Jasiuk, I., "Reference point indentation study of age-related changes in porcine femoral cortical bone," *Journal of Biomechanics*, **46**(10): p. 1689-1696 (2013).
244. Buckwalter, J., Glimcher, M., Cooper, R., and Recker, R., "Bone biology," *Journal of Bone and Joint Surgery*, **77**(8): p. 1256-1275 (1995).
245. Gupta, H.S., Seto, J., Wagermaier, W., Zaslansky, P., Boesecke, P., and Fratzl, P., "Cooperative deformation of mineral and collagen in bone at the nanoscale," *Proceedings of the National Academy of Sciences of the United States of America*, **103**(47): p. 17741-17746 (2006).
246. Ridha, M. and Shim, V.P.W., "Microstructure and tensile mechanical properties of anisotropic rigid polyurethane foam," *Experimental Mechanics*, **48**(6): p. 763 (2008).